



CHALMERS

Steering control for haptic feedback and active safety functions

TUSHAR CHUGH

DEPARTMENT OF MECHANICS AND MARITIME SCIENCES

CHALMERS UNIVERSITY OF TECHNOLOGY

Gothenburg, Sweden 2021

www.chalmers.se

THESIS FOR THE DEGREE OF DOCTOR OF PHILOSOPHY
IN MACHINE AND VEHICLE SYSTEMS

Steering control for haptic feedback and active safety functions

TUSHAR CHUGH

Department of Mechanics and Maritime Sciences
CHALMERS UNIVERSITY OF TECHNOLOGY
Gothenburg, Sweden 2021

Steering control for haptic feedback and active safety functions

TUSHAR CHUGH

ISBN 978-91-7905-521-9

© TUSHAR CHUGH, 2021

Doktorsavhandlingar vid Chalmers tekniska högskola

Ny serie nr. 4988

ISSN 0346-718X

Department of Mechanics and Maritime Sciences

Chalmers University of Technology

SE-412 96 Gothenburg

Sweden

Telephone: +46 (0)31-772 1000

Chalmers Reproservice

Gothenburg, Sweden 2021

Steering control for haptic feedback and active safety functions

TUSHAR CHUGH

Department of Mechanics and Maritime Sciences

Chalmers University of Technology

Abstract

Steering feedback is an important element that defines driver–vehicle interaction. It strongly affects driving performance and primarily depends on the steering actuator’s control strategy. Typically, the control method is open loop, that is, it has no reference tracking. Its drawbacks are hardware dependent steering feedback response and attenuated driver–environment transparency. Accordingly, this research investigates a closed-loop control method for electric power assisted steering and steer-by-wire systems. The advantages, compared to open loop control, are: (a) better hardware impedance compensation; (b) system independent response; (c) explicit transparency control; and (d) direct interface with active safety functions.

The proposed closed-loop architectures include a reference model, a feedback controller, and a disturbance observer. The feedback controller forms the inner loop and ensures the following: reference tracking, hardware impedance compensation, and robustness against coupling uncertainties. Two different causalities are studied: torque and position control. The two are objectively compared in this thesis from the perspective of (uncoupled and coupled) stability, tracking performance, robustness, and transparency.

The reference model forms the outer loop and defines a torque or position reference variable, depending on the causality. Different haptic feedback functions are implemented to control the following parameters: inertia, damping, Coulomb friction, and transparency. Transparency control in this application is particularly novel, which is sequentially achieved. For non-transparent steering feedback, an environment model is developed such that the reference variable is a function of virtual dynamics. Consequently, the driver–steering interaction is independent from the actual environment. Whereas, for the driver–environment transparency, environment interaction is estimated using a disturbance observer; then, the estimated signal is fed back to the reference model. Furthermore, an optimization based transparency algorithm is proposed. This renders the closed-loop system transparent in case of environmental uncertainty, even if the initial condition is non-transparent.

The steering related active safety functions can be directly realized using the closed-loop steering feedback controller. This implies, but is not limited to, an angle overlay from vehicle motion control functions and a torque overlay from haptic support functions.

Experimental results and theoretical findings presented in the thesis are corroborated, including the real-time implementation of torque and position control strategies. In general, it can be concluded that position control lacks performance and robustness due to high and/or varying system inertia. Although the problem is somewhat mitigated by a robust \mathcal{H}_∞ position controller, the high frequency haptic performance remains compromised. Whereas, the required objectives are simultaneously achieved using a torque controller.

Keywords: haptic feedback, steering system, torque control, position control, passivity, coupled stability, uncoupled stability, state estimation, transparency, active safety

Acknowledgments

First and foremost, I would like to thank my supervisor, Dr. Fredrik Bruzelius, for his exceptional guidance throughout the work presented in this thesis. I would also like to appreciate the sincere efforts of my examiner, Professor Bengt Jacobson, and Dr. Matthijs Klomp for the suggestions and project management. I am further thankful to Dr. Barys Shyrokau at Delft University of Technology for the collaboration and feedback. I also express my appreciation to the funding agencies: the ITEAM project in the European Union’s Horizon 2020 research and innovation program as well as the SWOPPS project under Electronics, Software and Communication (EMK) as part of the Swedish Strategic Vehicle Research and Innovation (FFI) program.

I am grateful to my colleagues at Volvo Car Corporation, particularly David Dahlgren, Pontus Carlsson, Joakim Norrby, Carl-Johan Häll, Johan Eklöv, Marcus Ljungberg, Anton Albinsson, Weitao Chen, and Georgios Minos for the discussions, support, and assistance with proving ground experiments.

I would also like to thank past and present colleagues of the VEAS division at Chalmers University of Technology for a friendly working environment. My sincerest gratitude goes to Sonja and Simone for ensuring that PhD students maintain a proper work–life balance. I am incredibly thankful and forever indebted to my friends for the different sports activities, after-works, fun discussions, and conversations during coffee breaks.

Lastly, thank you mom, dad, and Ruchir for your support, especially in dealing with my frustration at times during this journey.

Tushar Chugh
October, 2021

List of Publications

This thesis consists of an extended summary and the following appended papers.

Paper A: T. Chugh, F. Bruzelius, M. Klomp, and S. Ran. Comparison of steering feel control strategies in electric power assisted steering. In: Proceedings of the 14th International Symposium on Advanced Vehicle Control (AVEC), Beijing, China, 2018. URL: <https://research.chalmers.se/en/publication/504620>

Paper B: T. Chugh, F. Bruzelius, M. Klomp, and B. Shyrokau. Design of haptic feedback control for steer-by-wire. In: Proceedings of the 21st IEEE International Conference on Intelligent Transportation Systems (ITSC), Maui, USA, pp. 1737–1744, 2018. doi:10.1109/ITSC.2018.8569795

Paper C: T. Chugh, F. Bruzelius, M. Klomp, and B. Shyrokau. An approach to develop haptic feedback control reference for steering systems using open-loop driving manoeuvres, *Vehicle System Dynamics*, vol. 58, no. 12, pp. 1953–1976, 2019. doi:10.1080/00423114.2019.1662923

Paper D: T. Chugh, F. Bruzelius, M. Klomp, and B. Jacobson. Steering feedback transparency using rack force observer. Submitted for possible journal publication.

Paper E: T. Chugh, F. Bruzelius, B. Kulcsár, and M. Klomp. Robust \mathcal{H}_∞ position control for vehicle steering. To be submitted for possible journal publication.

The author of the thesis was responsible for the control architecture, design, modeling, simulation, experiments, and analysis. The co-authors contributed with the discussions. The papers were written by T. Chugh with many valuable inputs from Dr. Bruzelius.

Other relevant publications by the author, but not included in the thesis:

1. T. Chugh, W. Chen, et al. Design and control of model based steering feel reference in an electric power assisted steering system. In: Proceedings of the 25th International Symposium on Dynamics of Vehicles on Roads and Tracks (IAVSD), Rockhampton, Australia, pp. 43–49, 2017. URL: <https://research.chalmers.se/en/publication/511873>
2. L. Schenk, T. Chugh, et al. Musculoskeletal driver model for the steering feedback controller, *MDPI Dynamics and Control of Automated Vehicles*, vol. 3, no. 1, pp. 111–126, 2021. doi:10.3390/vehicles3010007
3. W. Chen, T. Chugh, et al. Design and control of the steering torque feedback in a vehicle driving simulator. In: Proceedings of the 25th International Symposium on Dynamics of Vehicles on Roads and Tracks (IAVSD), Rockhampton, Australia, 2017.

The patent application by the author:

T. Chugh, F. Bruzelius, and D. Dahlgren. “Method and apparatus for operating a haptic system”, Volvo Car Corporation, European Patent 20163724.6 (filing date: March 17, 2020) and U.S. Patent 17/203,106 (filing date: March 16, 2021).

Abbreviations

Abbreviation	Description
ADAS	Advanced Driver Assistance System
ADS	Automated Driving System
CAN	Controller Area Network
CG	Center of Gravity
DAS	Driving Automation System
DFR	Direct Force Reflection
DOF	Degrees of Freedom
EKF	Extended Kalman Filter
EPAS	Electric Power Assisted Steering
FFb	Force-Feedback
FRF	Frequency Response Function
HIL	Hardware-in-the-Loop
HMI	Human–Machine Interface
IMU	Inertial Measurement Unit
KF	Kalman Filter
LMI	Linear Matrix Inequality
LQ	Linear Quadratic
LTI	Linear Time-Invariant
MPC	Model Predictive Control
OCP	Optimal Control Problem
PEB	Position Error Based
QP	Quadratic Programming
RWA	Road Wheel Actuator
SbW	Steer-by-Wire
SISO	Single Input Single Output
UKF	Unscented Kalman Filter

Contents

1	Introduction	1
1.1	Background	2
1.1.1	A human–robot interaction perspective	2
1.1.2	The importance of steering feedback	5
1.1.3	The vehicle motion control aspect	7
1.2	Research questions	8
1.3	Limitations	9
1.4	Scientific contribution	10
1.5	Thesis outline	10
2	System dynamics	13
2.1	Steering system	13
2.1.1	Electric power assisted steering	13
2.1.2	Steer-by-wire	15
2.2	Models for environment interaction	18
2.3	A model for driver interaction	21
3	Steering feedback control	23
3.1	Interaction dynamics	23
3.2	State of the art: Open loop	25
3.2.1	Electric power assisted steering control	26
3.2.2	Steer-by-wire force-feedback control	30
3.3	Closed-loop strategy	31
3.4	Torque control	34
3.4.1	Stability analysis	35
3.4.2	Tracking performance and robustness	39
3.5	Position control	41
3.5.1	Stability analysis	41
3.5.2	Typical shortcomings	45
3.5.3	A more robust solution: \mathcal{H}_∞ control	47
3.6	Summary	49
4	Steering feedback reference	51
4.1	Model structure	51
4.1.1	Torque reference	52
4.1.2	Position reference	56
4.2	Non-transparency using virtual environment	57
4.2.1	Rack force model	57
4.2.2	Evaluation of non-transparent setting	62
4.3	Disturbance estimation	67
4.3.1	Vehicle motion based observer	67

4.3.2	Steering system based observer	70
4.3.3	Evaluation of observers	71
4.4	Transparency using estimated disturbance	72
4.5	Transparency control	75
4.5.1	Motion based concept	75
4.5.2	MPC algorithm	77
4.5.3	Examples of optimization based transparency	80
4.6	Summary	83
5	Interfacing active safety functions	85
5.1	Open loop control: Motor torque overlay	85
5.2	Closed-loop control	86
5.2.1	Angular position overlay	87
5.2.2	Driver torque overlay	89
6	Summary and future work	91
6.1	Discussion	91
6.2	Conclusion	94
6.3	Future work	95
	Appendix A Experimental setups	99
	Appendix B Model and controller parameters	103
	References	107
	Appended Papers	

1 Introduction

Electrification and driving autonomy are widely researched topics in the vehicle industry. Their combination offers many benefits, such as energy efficiency, safety, performance, and advanced technologies (e.g., platooning and cooperative interaction). An energy efficient system aims to perform certain tasks using as little energy as possible, thus reducing CO₂ emissions and lowering overall cost. As for driving automation, in general, various safety aspects, for example traffic safety, road safety, and system safety are covered. Vehicle safety can be improved through electrified propulsion [1], such as using differential braking [2,3] or improving hardware [4] for emergency braking, etc. Furthermore, applications involving two or more semi-autonomous/fully autonomous vehicles or agents communicating, coordinating, and subsequently controlling their trajectory are considered under cooperative interaction [5]. Lastly, performance is defined according to how well a given mechatronic system (because of its designed software functions) delivers the required user experience. This thesis focuses on the performance of one such mechatronic system and proposes two control alternatives that it can employ.

The mechatronic system being investigated here is vehicle steering. It provides a human-machine interface (HMI) for the driver that defines the haptic feedback. Simultaneously, the steering system interacts with the environment. The environment interaction is not only important for the haptic feedback but also for the driving automation system (DAS), regardless of the automation level [6]. This is because an undertaken *dynamic driving task* has to be performed by an advanced driver assistance system (ADAS) or an automated driving system (ADS) such that vehicle motion is controlled in both longitudinal and lateral directions; the steering system is responsible for the latter.

The term *haptic* literally means touch sensation. In a mechatronic system, it defines the interaction between human, machine, and environment. Throughout this thesis, kinesthetic (haptic) feedback, which is responsible for muscular forces as a function of the angular position of body joints, is considered. The importance of haptic feedback for human operated task completion is a well known phenomenon [7,8], particularly in remote surgery [9]. There are various haptic feedback applications. In telerobotics and telemanipulated devices, robots are remotely controlled and generate desired haptic sensations during exploration for the operator [10–14]. In minimally invasive surgery, robots employ telepresence and telemanipulation to create force feedback for the surgeon [15–18]. Flight and driving simulators generate haptic feedback for the pilot and driver using a virtual environment, respectively [19–21], and exoskeleton devices assist human limbs during body movements [22–24]. Some of the foregoing examples are shown in Fig. 1.1. Note that the driver-steering interaction falls under the same category.

The driver-vehicle interaction is subjectively perceived by humans as steering feel. It is a combination of information feedback from multiple sources/cues: haptic, visual, audio, and motion. In this thesis, the haptic part of steering feel is referred to as *steering feedback*, and its subsequent manipulation through a given actuator is further termed as *steering feedback control*.



Figure 1.1: Examples of the haptic feedback application with a suitable HMI: an exoskeleton, a driving simulator, a telemanipulated surgical robot with a master console, an F-35 flight simulator, and a teleoperated robot for exploration. Photo credits: Lockheed Martin Corporation, German Aerospace Center (DLR), European Space Agency (ESA), and Volvo Car Corporation.

1.1 Background

A typical state-of-the-art passenger vehicle steering system consists of an actuator to assist the driver in overcoming resistant road forces. Over the years, the actuator has transitioned from a hydraulic pump to a servo (electric) motor due to the environmental benefits afforded by the latter [25–28]. In addition to steering feedback control, electrical actuation also offers an opportunity for ADAS functions [29]. A conventional steering system with a steering rack-mounted servo motor is known as electric power assisted steering (EPAS), see Fig. 1.2(a). In EPAS, one actuator controls both steering feedback and vehicle motion objectives. Concurrently, the same system hardware is responsible for human and environment interactions. Moreover, a torque sensor provides a measured indication of the applied driver torque input, known as torsion bar torque.

A more advanced steering configuration is a steer-by-wire (SbW) system, similar to telerobotics and telemanipulated devices, as shown in Fig. 1.2(b). Here, two actuators are involved, i.e., a force-feedback (FFb) for the driver interaction and a road wheel actuator (RWA) for the environment interaction, which are responsible for steering feedback control and vehicle motion control tasks, respectively. They are necessary due to the mechanical disconnection between the human and the environment.

First, a brief overview of robotic devices from which parallels are drawn between the two interactions (driver–steering and human–robot) is presented. Second, the importance of steering feedback is explained, and a short summary of different steering feedback control methods is presented in Section 1.1.2. In Section 1.1.3, the lateral vehicle motion control is discussed with respect to driving automation.

1.1.1 A human–robot interaction perspective

The concept of manipulating haptic feedback is typically known as interaction control [30–32]. An EPAS system is analogous to exoskeletons and robotic devices for rehabilitation because of similarities in the model configuration and input–output channels. Therefore, a considerable inspiration is drawn from robotics. These devices assist a human to follow a virtual reference [24] and subsequently interact with the environment to complete a given task, e.g., object grasping [33], and providing support to upper/lower limb movement [34]. Similarly in EPAS, the driver is supported by the actuator to counteract the tire–road interaction.

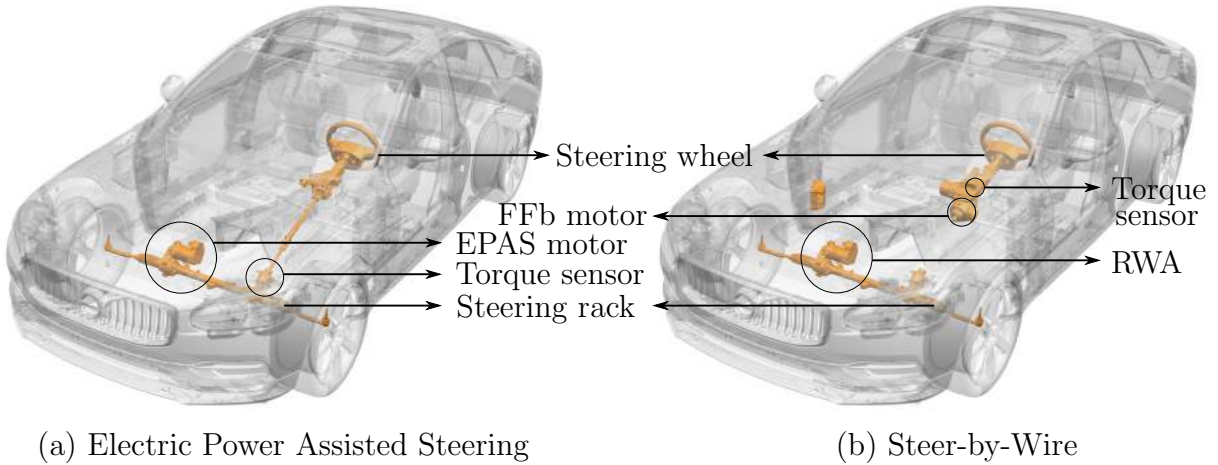


Figure 1.2: Typical passenger vehicle steering configurations: (a) electric power assisted steering and (b) steer-by-wire system with force feedback (FFb) motor and road wheel actuator (RWA).

In the literature, different control solutions are reported for a rehabilitation robot based on the (lower level control) error minimization principle, in which an error is defined as the difference between reference and measured variables. A straightforward approach is the use of direct torque/force feedback with a null torque/force reference, thus decreasing the system impedance for minimal distortion [35, 36]. This state-of-the-art method is also known as zero torque/impedance control or direct impedance manipulation [31]. However, for clarity, it is defined as open loop control because of the null reference and error minimization is virtually absent. If the reference variable is not null, then the control method is closed-loop.

For closed-loop torque or impedance control, the reference torque/force variable (i.e. the higher level control) is computed online and updated [31, 37–43]. A thorough comparison among different torque controllers is reported in [44]. The comparison claims that a proportional-learning-damping control, which is shown to be similar to the classical PID (proportional-integral-derivative) control, yields the best performance for such configurations.

Another closed-loop alternative involves an opposing error minimization principle to control the motion trajectory in terms of angular position and velocity feedback. This approach is called position/velocity or admittance control; a few examples are reported in [22, 23, 43, 45–50]. In the foregoing, reference is also defined in terms of the motion trajectory variables. For instance, [23, 45, 46] implemented virtual stiffness and damping using an admittance PD (proportional-derivative) controller. A comprehensive review of different control strategies can be further studied in [51].

A typical aspect is that, regardless of the closed-loop method, attaining satisfactory reference tracking by lower level control requires high (controller) gains to compensate for hardware impedance. Nevertheless, this is evidently limited to a certain extent due to reasons affecting stability [30, 35]. However, [22, 47] reported an additional performance improvement using an explicit inertia compensation function along with an LQ (linear quadratic) position controller and robust control solutions, such as that proposed in [48]. Eventually, this can ensure faster limb movement due to the lower effective system inertia.

Different approaches for computing the reference variable depending on the application

requirements are available. A conventional technique is to use the measured angular position and/or velocity signal with a virtual impedance function for a fixed torque reference. In position control, the measured torque signal and a virtual admittance function for a fixed position reference are used. As a result, the foregoing causes non-transparency toward changes in system dynamics, environment interaction uncertainties, etc. A system with low transparency considerably distorts the actual interaction dynamics; hence, it relies on virtual haptic sensations [52].

The next logical step should be to include additional information, models, and measurements to generate an adaptive reference variable, thus realizing a certain degree of robotic transparency [36, 39, 53, 54]. Although the maximum achievable transparency is limited by robot inertia, it can be efficiently improved using a suitable reference variable. The examples in [39, 53] improved transparency by modifying the higher level (torque) control request using a coupled oscillator to anticipate the input signal harmonics and a dynamic model-based compensator, respectively. In [54, 55], the use of a real-time disturbance observer to achieve the same purpose was reported. A similar methodology can be adopted for developing the closed-loop steering feedback controller.

Due to similarities in model dynamics and the same haptic input–output channels, an SbW system is regarded an example of a telemanipulated device. The main difference between the two is that in the former, the driver’s perception is not entirely disconnected from the environment. This is because the information flow from other feedback channels (motion, visual, and audio) are still natural and exactly the same as those in EPAS. Despite that, the haptic feedback findings published in relevant literature can be applied.

Telerobotics and teleoperated devices operate on the principle of telepresence or telemanipulation [12], where the human operator is remotely coupled to a distant environment using a suitable HMI [13, 17, 56–58]. For such configurations, the hardware includes a *leader* and a *follower*. The former constitutes of human interaction port and environment interaction port on the latter. These systems are inherently non-transparent and remains the same even in the case of unilateral teleoperation. This implies that motion and/or force signals are sent from the leader to the follower but not contrariwise [59]. If motion and/or force signals are also directly sent back from the follower to the leader, thus forming an interconnection for transparency, then it is defined as bilateral teleoperation. An important remark: transparency improves human perception and task performance, particularly when the environment interaction is uncertain and/or safety critical, such as in teleoperation robots used in minimally invasive surgery [15–17, 60].

Bilateral teleoperation is a well-known field that has been extensively studied over the years to ensure stability and transparency for different control architectures and applications. A control architecture is defined by closed-loop solutions for leader and follower actuators. Typical architectures are torque/force–position, position–position and torque/force–torque/force. Stability is an important aspect for such systems mainly due to a time delay in the communication channel and other reasons, such as non-linear dynamics and human or environment coupling as reported in [61]. This is usually achieved by ensuring a *passive* interaction port. According to [31, 62], a system is considered passive if the output energy at its interaction port, for any time instant, does not exceed the total energy injected into the same port over the complete time. Therefore, a passivity-based

control could be employed to guarantee stability; however, due to conservatism, it could result in transparency loss (or less robust performance) [12, 63, 64]. A general framework of stability and transparency optimized teleoperation using all four information channels (i.e., torque and velocity exchanges between the leader and follower) for linear systems was first introduced in [12]. Apart from the four-channel architecture, a simplified solution can be a two-channel architecture with different causalities: (a) position error based (PEB) and (b) direct force reflection (DFR) [65]. For the PEB control, the position and/or velocity signals of the leader and follower are exchanged for transparency. In contrast, the force/torque signal from the follower's environment interaction (instead of position signal) is transmitted back to the leader in the DFR method. In this thesis, a DFR for SbW control is investigated, assuming that stability is ensured because of the following reasons: (a) a higher degree of transparency performance compared with that of PEB is attainable due to direct force feedback [12]; (b) a common reference variable solution based on DFR can be implemented for both types of system dynamics, i.e., rehabilitation robots (or EPAS) and telerobotics (or SbW).

There are many published articles on telemanipulation in robotics that could be utilized for a desired SbW control architecture. For example, [65] implemented a force sensor to the follower for improved transparency in the two-channel (PEB and DFR) and four-channel control architectures. Here, the effect of time delay is ignored in implementing simplified linear stability analysis because of the lower sampling time and faster signal communication (i.e., approximately 1 ms for steering system signals). However, extensive research on this topic has been performed in [64, 66–69], thus confirming that stability is ensured by preserving passivity. Given a certain sampling time and viscous damping parameter, they optimized the performance of a 1-DOF (degree of freedom) leader device for virtual haptic feedback. A detailed review of bilateral teleoperation in the four-channel architecture with the aforementioned communication delay effect is reported in [70]. Other applications, such as multiple follower robots with enforced passivity for coupled stability are found in [71]. In [72, 73], applications for a non-linear teleoperation control in the two-channel PEB and four-channel architectures, respectively, have also been reported.

From the perspective of human–robot interaction, the driver's steering feedback is extremely relatable. In this research, two closed-loop steering feedback control methods are developed and compared. Thus, theoretical contributions are generic and valid for similar system dynamics.

1.1.2 The importance of steering feedback

In EPAS and SbW systems, road wheels are mechanically connected to the steering rack (Fig. 1.2); and the rack is further actuated by its corresponding motor. Thereby, the vehicle response is dependent on the steering rack actuation. Consequently, the human perception of steering feedback primarily results from the driver–vehicle interaction which essentially depends on the steering system and its control strategy. Various steering feedback control methods have been investigated and introduced into product or prototype development over the years [74–79]. Hence, the following questions arise. What exactly is the problem? What new solutions are necessary?

From the steering feedback aspect, the state-of-the-art EPAS control (i.e., open loop or direct impedance manipulation) has two main drawbacks: poor driver–environment transparency or road feedback and hardware dependent response. The former implies an attenuated (high frequency) response to the steering wheel from the tire–road interaction dynamics on the environment port. This occurs due to higher effective servo motor impedance [29] and its limited compensation. For the latter, the open loop control formulation depends on system dynamics and so as the resulting haptic response. Therefore, different closed-loop solutions are investigated to improve the driver–environment transparency and define a hardware independent (or an absolute) haptic response. The implementation involves a steering feedback reference model that outputs a suitable reference variable. Consequently, assuming that stability is ensured due to different system dynamics, the same reference model can be used in SbW because the reference solution is hardware independent.

Some examples of EPAS open loop control that suffer from the aforementioned loss of transparency are found in [74–76, 80–83]. Accordingly, closed-loop methods for overcoming this problem are sought. Many researchers have already proposed techniques in EPAS including torque control [78, 84–87] and position control [88–90]. However, most of these studies lack thorough stability and transparency analysis. Although [78, 86] attempted to restore transparency using measured vehicle motion states, such as lateral acceleration and yaw rate, this approach could be less effective as described in this thesis. Similarly, [88, 89] proposed an EPAS position controller with road feedback; however, the concept lacked proper experimental validation, particularly in terms of frequency response. In [90], a better position control solution was proposed. It had an empirical road feedback filtering solution instead of a model-based approach and a limited discussion on stability.

Typical SbW control architectures (with DFR and PEB) are discussed in [91] and [92], respectively. For SbW-FFb, a straightforward control solution is open loop [93–96]. Accordingly, the required FFb motor torque is computed and requested for a desired steering feedback without any lower level FFb control. In contrast, [97–99] proposed an FFb torque controller, and [77, 79, 100] put forward an FFb position controller. The objective is to thoroughly compare these methods in terms of stability, robustness, and transparency and then evaluate the steering feedback performance using the same reference as that in EPAS. As stated, until the road feedback force or rack position signal is explicitly included in the FFb controller, the SbW system remains non-transparent. A simple approach to achieve limited transparency is to empirically use the measured vehicle motion states as that reported in [93, 101] or a bilateral control scheme with rack position feedback as that in [102]. Whereas, this thesis proposes a force observer-based transparency approach suitable for closed-loop configurations in EPAS and SbW-FFb. For controlling the RWA (or follower) in SbW, a typical (rack) position control law similar to the EPAS position controller is implemented for sufficient tracking performance. The RWA control design is not emphasized in this thesis, however reported in other articles, such as cascaded yaw rate and rack position controller [103, 104] and a robust controller against the tire–road uncertainties [105, 106].

This leads to the question on why steering feedback is important. The answer is similar to the conclusions reported in [7, 14] claiming that a higher haptic feedback quality improves task performance and human control actions. If the steering feedback lacks transparency, then the resulting driving performance is inferior in the case of uncertain tire–road interaction.

Consequently, supplementary steering feedback guidance and interventions from an ADAS (or active safety) function should be provided to support the driver [107]. This is also illustrated in [100], where the driver receives haptic support while driving near the vehicle's handling limits or performing extreme dynamic maneuvers (e.g., drifting on a slippery road surface). Therefore, better transparency can significantly improve the lateral vehicle motion performance and reduce the driver's mental and physical effort, as claimed in [100]. Another example is reported in [108] where the driver's haptic response is modified by including vehicle motion information through lateral acceleration feedback to prevent rollover.

In the next example, consider a racing scenario in which a higher vehicle speed is required at the corners for a shorter lap time. Maximizing tire performance (i.e., operating near the tire-road friction limit) results in a motion trajectory close to the optimal racing line for a faster lap. This requires a higher steering activity from the driver in search of the maximum lateral tire-road grip, as experimentally demonstrated in [109]. This indicates the degree of actual tire-road interaction dynamics transparent to the driver in the applied steering torque at a given steering angle. A more transparent steering torque could improve the human perception of path following, thereby assisting the driver to operate at a particular lateral tire force-slip angle point, as shown by the mathematical driver model in [110]. The better the environmental transparency, the faster the steering correction. Consequently, a shorter lap time could be achieved by increasing the driver's compensatory steering control activity (or corrections) [111], particularly near the limits of vehicle handling where the tire-road interaction could be uncertain. Note that typical driver models with path-following control [112–114] are based on the vehicle state feedback and the steering torque feedback is not explicitly included. Modifications to such driver models may include minimization problem, i.e., optimizing the tire performance for a minimum lap time, similar to that reported in [115, 116]. This is because, in reality, a driver can perform steering corrections based on the applied steering torque, which must implicitly reflect the front axle lateral tire force or equivalent aligning moment. Subsequently, by reacting to the haptic sensation that is as real as possible, the driver's response is accelerated, although vehicle motion is naturally delayed due to a cause-and-effect relationship. Hence, this study investigates a model-based steering feedback reference that can explicitly and sufficiently control environmental transparency.

1.1.3 The vehicle motion control aspect

For controlling lateral vehicle motion, different ADAS and ADS functions request an external angular position and/or velocity to steer the vehicle. Regardless of the steering feedback control method, the external request from these functions should be capable of performing the steering actuation. To execute such interventions, a straightforward solution is the use of a position controller. However, the question on how this action can be implemented using the same closed-loop controller for the steering feedback manipulation, particularly with the torque control approach, remains unanswered.

Some examples of these ADAS functions are active front steering, lane departure warning/prevention, lane keeping assistance/aid, and pilot assist [3, 100, 117, 118]. The shared steering control functions in which the driver and vehicle motion are supported by

an additional steering angle/torque overlay request can also be included [119]. For instance, stabilizing a vehicle operating near the handling limits or drifting equilibria using a driver steering support interface is presented in [100, 120]. Their implementation involves an LQ controller that calculates an optimal steering angular position (apart from the rear wheels' torque request) for the steady state stabilization problem during drifting and provides guidance to the driver by changing the steering angle. Other examples on computing an optimal steering angle for trajectory control and using it as the reference variable (especially near the limits of tire-road friction or an uncertain environment) to coordinate with and without the driver are found in [121–126]. Basically, most of them resolve a similar problem of autonomous drifting with different complexities. Moreover, they rely on the same principle of computing an optimal steering angle reference and realizing it through a typical lower level position controller. Of course, the foregoing approach makes sense for a highly or fully ADS. However, with a driver in the loop, the required lateral vehicle motion could be achieved and/or improved either by the driver (based on transparent steering feedback) or supported by shared steering control techniques, such as those proposed in [127–130]. For the latter, an interface is required to overlay a suitable external request variable in the steering feedback controller.

1.2 Research questions

A fundamental investigation on closed-loop steering feedback control is performed in this thesis. The main highlights are control design and a comparison of different methods, theoretical and experimental through real-time digital implementation. Three problems are identified from Sections 1.1.2 and 1.1.3. Consequently, the following research questions are formulated:

1. Which closed-loop solution (between torque and position control) offers better steering feedback performance and robustness in EPAS and SbW-FFb?

The first research question deals with the architecture problem of realizing closed-loop control in EPAS and SbW systems. Two opposing model-based causalities are studied: torque and position control in EPAS and torque–position and position–position control in SbW. The aim is to sufficiently achieve and manipulate transparency with the closed-loop approach, which is a shortcoming of open loop control. Thereby, the main aspects to the given problem are: how should non-transparent causality be defined? What stability conditions are important? How robust is a given solution against uncertainties at the coupling port? How good is the reference tracking performance? How can transparency be achieved with guaranteed stability? The answer to all these questions can conclude about the best possible closed-loop solution for steering feedback control.

2. How should the steering feedback response be mathematically represented in the reference model independent of system dynamics?

The second research question pertains to the reference model structure for torque and position control. Given a certain closed-loop setting, the same reference model should

be valid for both EPAS and SbW-FFb, because the intention is to use the same input signals and define the required output reference variable. Moreover, given a certain (lower level controller's) reference tracking, the reference parameters should satisfy the stability constraints derived in the first research question. Due to causality inversion and the pursuit of a model-based approach, the reference models for torque and position control must be complementary. A reasonable steering feedback reference model should consider the following aspects: impedance or admittance dynamics, formulation of a virtual environment model for non-transparency, estimation of the actual environment interaction for transparency, and subsequent computation of optimal transparency in case of tire-road interaction uncertainty.

3. How can a steering related active safety function be realized using the closed-loop steering feedback controller?

The third research question refers to the problem of executing an intervening task by a given active safety function, particularly the lateral vehicle motion control functions, such as pilot assist and lane keeping assistance. This problem has two parts: why may the existing solution (from open loop control) might not be an ideal approach? How can the external request variable from these functions be superimposed in a closed-loop steering feedback control setting? The answer to the last question is sought to provide an interface for realizing the shared steering control requests through the same controller used for steering feedback manipulation.

1.3 Limitations

As stated earlier, this thesis mainly deals with the performance of steering feedback control and disregards other aspects, such as system and functional safety, in particular, with respect to ISO-26262 [131]. However, the implementation of a controller for real-world experiments requires certain safety measures, which are undertaken in this work. Some of the practical and theoretical limitations considered are as follows.

- (a) **Sensors and signal communication:** The higher resolution, lower sampling, and faster update time of measured signals ensure lower communication delay and increase the possibility of faster controller tuning.
- (b) **Digital implementation:** To execute a real-time controller, bilinear transformation from the s -domain to the z -domain is performed. For the state estimation problem, the first-order exponential method is selected for linear equations, and the second-order Taylor-Lie series method to non-linear equations.
- (c) **Anti-windup:** The presented lower level controllers are limited to the linear control design with an integrator for disturbance attenuation and low steady state tracking error. Hence, a typical anti-windup solution is implemented to counteract actuator saturation and avoid integral state overflow.
- (d) **Feedback linearization:** The lower level control laws sufficiently assume a linear time-invariant (LTI) system dynamics because the model parameters (inertia/mass

and damping) are time-invariant. Moreover, the actual Coulomb friction force/torque is reasonably estimated using an observer and it is subsequently compensated.

- (e) **Stability analysis:** To derive the stability condition through the passivity of an interaction port, an underlining assumption for the coupling element dynamics is necessary. For simplicity, this thesis assumes that the driver and environment model are passive.
- (f) **Subjective evaluation:** Although the driver–vehicle interaction is subjectively perceived, the subjective evaluation of steering feedback is kept out of context. This is due to significant variations in the human perception toward a haptic controlled system in varying environments, thus requiring different analyses.

1.4 Scientific contribution

The major contributions of this research work are as follows:

- (a) A comparison between torque and position control for EPAS and SbW-FFb in terms of stability, tracking performance, robustness, and transparency.
- (b) A multi-variable position control solution based on the \mathcal{H}_∞ optimization principle is developed for EPAS and SbW-FFb to attain robustness against coupling inertia.
- (c) A methodology for developing a non-transparent steering feedback reference model using state-of-the-art vehicle steering system and conventional vehicle dynamic maneuvers is formulated.
- (d) Vehicle motion based and steering system based rack force observers are compared; the best available estimate for steering feedback transparency is subsequently used.
- (e) The computation of optimal transparency as a function of vehicle motion states in case of tire–road interaction uncertainty is proposed.
- (f) A new signal interface to realize steering related active safety functions through the closed-loop steering feedback controller is presented.

1.5 Thesis outline

The outline of this thesis is as follows. Chapter 2 briefly describes the system dynamics and models of steering, environment, and driver that are required for the controller development in EPAS and SbW. The first research question is addressed in Chapter 3 beginning with a short introduction to the driver–steering–vehicle interaction dynamics and then describing the shortcomings of open loop control. This chapter also presents the haptic control design aspects: stability, performance, robustness, and transparency. Chapter 4 proposes an answer to the second research question that comprehensively describes the steering feedback reference models for torque and position control. Moreover, this chapter presents the

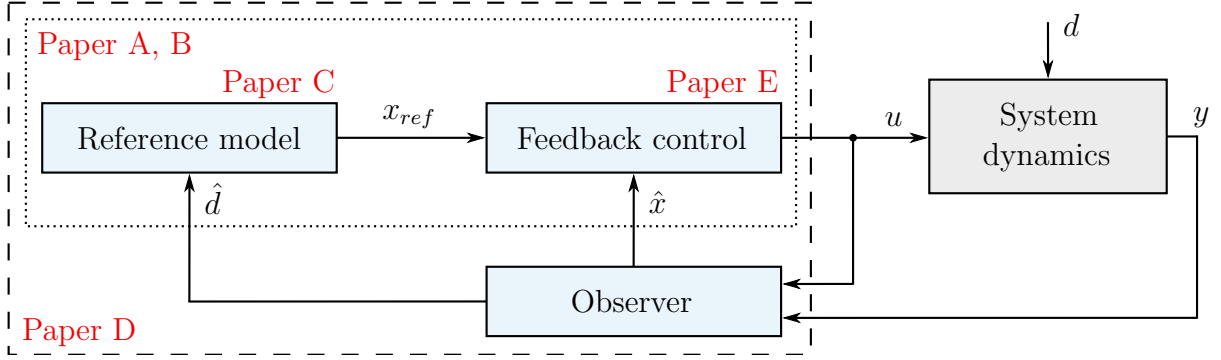


Figure 1.3: A typical state feedback control layout [132] with control input u , disturbance d , measured output y , estimated disturbance \hat{d} , estimated state \hat{x} , and reference state x_{ref} . The contribution of each appended paper is highlighted.

experimental results and validation of suggested control architectures. The solution to the third research question involving the overlay of the external request variable from an ADAS/ADS function is proposed and covered in Chapter 5. The final discussion, concluding remarks, and some suggestions for future research are explained in Chapter 6. Papers of the author pertaining to the aforementioned scientific contributions are appended to the end of this thesis. A typical state feedback controller highlighting the contribution of each paper is illustrated in Fig. 1.3. A brief description of each paper is as follows.

Paper A

In EPAS, the system inherits a high mechanical impedance on the steering rack due to the servo motor inertia and corresponding transmission ratio between the rack and motor. Two single-variable closed-loop methods, i.e., torque and position control, are investigated to resolve the problem of high system inertia. For a fair comparison, a sufficient linear feedback control law is formulated, assuming a given LTI reference model to form a non-transparent interconnection. The controller parameters are chosen to ensure uncoupled and coupled stability regardless of the port dynamics and for a defined phase margin. A concluding remark for this paper: the position control method illustrates an inferior reference tracking performance for hardware systems with high inertia.

Paper B

A closed-loop comparison similar to that presented in Paper A is conducted for SbW-FFb (i.e., leader device only). The analysis is performed with sufficiently defined control laws and a given reference model, thus ensuring uncoupled and (the driver port) coupled stability of the interconnected system. A concluding remark for this paper: the reference tracking performance in position control decreases with increasing coupling inertia at the driver port.

Paper C

A methodology for creating a steering feedback reference model using state-of-the-art steady state and transient vehicle dynamic maneuvers is proposed in this paper. The reference

model parameters (i.e., inertia, viscous damping, Coulomb friction, and rack force frequency response function) are estimated for a non-transparent setting within the linear vehicle/tire operating range. Subsequently, a validation is performed in closed-loop EPAS and SbW-FFb for both torque and position controllers.

Paper D

Due to non-transparency in closed-loop EPAS and SbW, the steering feedback response is disconnected from the actual environment interaction dynamics. Therefore, to achieve the driver–environment transparency, the first step is to estimate the steering rack force at the environment port. For this, a comparison among different estimation schemes is performed. In the second step, the best available estimated rack force signal is fed back to the reference model, based on the DFR approach while ensuring stability. Experimental results indicate that transparency is achieved during the steering activity; this is particularly useful when driving at the limits of handling.

Paper E

A typical LTI position controller in Papers A and B suffers from performance loss due to increasing coupling port inertia (i.e., driver arm inertia). Accordingly, a multi-variable position controller is proposed based on the optimization principle of LMI- \mathcal{H}_∞ . The primary difference of the foregoing controller from a typical position controller is that the sensed torque signal is also utilized to improve the reference (position) tracking performance and robustness against the inertia variation. The controllers are verified through experiments on real EPAS and SbW-FFb hardware.

2 System dynamics

This chapter presents the system dynamics of different simulation models for controller development. In the given problem, the human-machine-environment interaction requires a driver, a steering, and an environment model. Although the simulation models vary in complexity and fidelity, the subsequent models are found sufficient for the proposed steering feedback controllers as demonstrated through real-world experiments in later chapters. The undertaken assumptions for the model simplifications are also motivated.

2.1 Steering system

This thesis focuses on EPAS and SbW systems (Fig. 1.2). In EPAS, the steering rack-mounted servo motor is responsible for providing the required steering feedback to overcome the steering rack force, i.e., the environment interaction dynamics. Whereas in SbW, two actuators, FFb and RWA, are responsible for controlling steering feedback and lateral vehicle motion, respectively. For the latter, the actuator is similar to the steering rack-mounted servo motor in EPAS. The two main sources of excitation are driver and environment, in addition to the corresponding actuator input channel. The former excitation source refers to human initiated steering movements, whereas the latter excitation source is attributed to actual road disturbance. The system dynamics for EPAS and SbW are introduced in the next section.

2.1.1 Electric power assisted steering

The input channels for an EPAS system are steering torque from the driver (M_s), steering rack force from the tire-road interaction (F_{rack}), and motor torque (M_{mot}). A simplified EPAS model is shown in Fig. 2.1. For convenience, the force balance on the steering rack is translated to the moment balance on the steering pinion using the rack-to-pinion transmission ratio, i_{rp} . As a result, the input channel becomes $M_{rack} = F_{rack}/i_{rp}$, i.e., defined as the rack torque. Moreover, there is a transmission ratio between the actuator and pinion, given by i_{mot} as the motor-to-pinion ratio. The resulting equations of motion for the given 3-DOF model are as follows:

$$\begin{aligned} J_s \dot{\omega}_s(t) &= -b_s \omega_s(t) - M_{s,fric}(t) - M_{tb}(t) + M_s(t) \\ J_p \dot{\omega}_p(t) &= -b_p \omega_p(t) - M_{rack}(t) - M_{rack,fric}(t) + M_{tb}(t) + M_{mot,eff}(t) \\ J_{mot} \dot{\omega}_{mot}(t) &= -b_{mot} \omega_{mot}(t) - M_{mot,fric}(t) - M_{belt}(t) + M_{mot}(t) \end{aligned} \quad (2.1)$$

where

$$\begin{aligned} M_{tb}(t) &= k_{tb}(\omega_s(t) - \omega_p(t)) + c_{tb}(\theta_s(t) - \theta_p(t)) \\ M_{belt}(t) &= k_{belt}(\omega_{mot}(t) - i_{mot}\omega_p(t)) + c_{belt}(\theta_{mot}(t) - i_{mot}\theta_p(t)) \quad \text{and} \\ M_{mot,eff}(t) &= i_{mot}M_{belt}(t). \end{aligned}$$

The steering angle and velocity are given by θ_s and ω_s , respectively; the pinion angle and

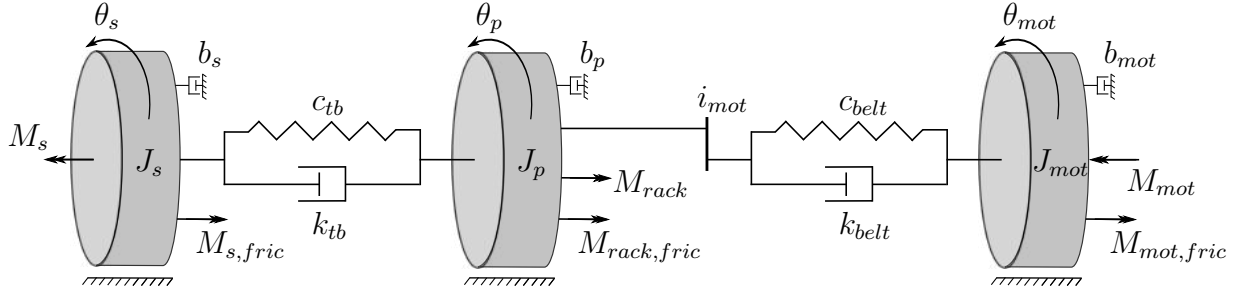


Figure 2.1: Free body diagram of simplified electric power assisted steering system with 3-DOF: steering wheel, pinion (equivalent to steering rack), and motor.

velocity are given by θ_p and ω_p , respectively; the motor angle and velocity are given by θ_{mot} and ω_{mot} , respectively. The impedance parameters are: steering wheel inertia (J_s), steering column damping (b_s), pinion inertia (J_p), pinion damping (b_p), motor inertia (J_{mot}), motor damping (b_{mot}), belt damping (k_{belt}) and belt stiffness (c_{belt}). The sensed torque or torsion bar torque is M_{tb} ; the compliance is defined by the torsion bar stiffness (c_{tb}) and damping (k_{tb}). The effective motor torque on the pinion ($M_{mot,eff}$) depends on the output belt torque (M_{belt}). Lastly, the Coulomb friction torques on each rotating inertia in Fig. 2.1 are given by $M_{s,fric}$, $M_{rack,fric}$, and $M_{mot,fric}$, respectively. For the Coulomb friction, any state-of-the-art model, such as Dahl and LuGre [133], can be used to compute the corresponding friction force/torque.

As presented in some of the appended papers, the following relationship holds for the steering rack force balance: $v_{rack} = \omega_p/i_{rp}$, where v_{rack} is the rack velocity, and x_{rack} is the rack position. The pinion impedance parameters can be translated on to those of the rack such that $m_{rack} = J_p i_{rp}^2$, $k_{rack} = b_p i_{rp}^2$ and $F_{rack,fric} = i_{rp} M_{rack,fric}$, where $F_{rack,fric}$, m_{rack} , and k_{rack} are rack Coulomb friction force, rack mass, and rack damping parameters, respectively. Similarly, the (motor) assist force on the rack is given by $F_{assist} = i_{rp} i_{mot} M_{belt}$. It should be noted that the front wheels' inertia is also lumped to m_{rack} .

In reality, the coupling between the motor and steering rack is more complicated than the aforementioned. Several other components such as ball nut assembly, recirculating balls, and intermediate compliance [29, pp. 409–415] are also present. These components are highly stiff; hence, they are neglected for faster computations in standalone MATLAB simulations. However, for verification and validation, they are included in high fidelity simulation software for vehicle dynamics, i.e., IPG CarMaker.

Another simplification by model order reduction is performed for designing the controller. This assumption is reasonable for two reasons: to derive simplified analytical expressions and enable real-time implementation. Here, the belt compliance between the motor and steering pinion is disregarded also due to high stiffness. Consequently, the pinion and motor dynamics can be combined. Upon model order reduction, $\omega_{mot} = i_{mot} \omega_p$ and $M_{mot,eff} = i_{mot} M_{mot}$ are valid. Hence, the pinion's equation of motion can be reformulated as

$$J_p \dot{\omega}_p(t) = -b_p \omega_p(t) - M_{rack}(t) - M_{p,fric}(t) + M_{tb}(t) + M_{mot,eff}(t) \quad (2.2)$$

where $M_{p,fric}(t) = M_{rack,fric}(t) + i_{mot} M_{mot,fric}(t)$, $J_p = m_{rack}/i_{rp}^2 + J_{mot} i_{mot}^2$ and $b_p = k_{rack}/i_{rp}^2 + b_{mot} i_{mot}^2$. To demonstrate this mathematically, consider the system dynamics

2.1. Steering system

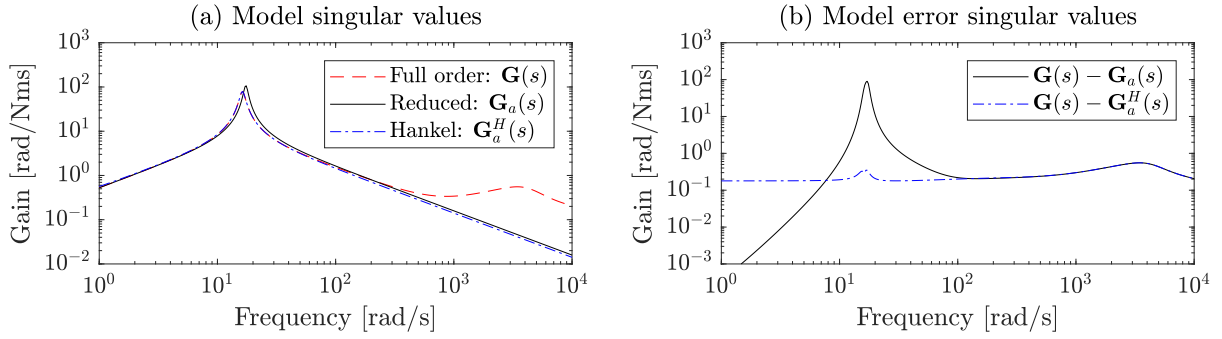


Figure 2.2: Singular values plot for (a) different model orders: full, reduced, and optimal Hankel; (b) reduced and Hankel error functions with respect to full order.

without any friction torques for linear analysis. The state space can be written as

$$\dot{\mathbf{x}}_{str}(t) = \mathbf{A}\mathbf{x}_{str}(t) + \mathbf{B}\mathbf{u}_{str}(t) \text{ and } y_{str}(t) = \mathbf{C}\mathbf{x}_{str}(t) + \mathbf{D}\mathbf{u}_{str}(t) \quad (2.3)$$

where $\mathbf{x}_{str}(t) = [\theta_s \ \omega_s \ \theta_p \ \omega_p \ \theta_{mot} \ \omega_{mot}]^T$ for the full order, $\mathbf{x}_{str}(t) = [\theta_s \ \omega_s \ \theta_p \ \omega_p]^T$ for the reduced order, $y_{str}(t) = \omega_p$ and $\mathbf{u}_{str}(t) = [M_s \ M_{rack} \ M_{mot}]^T$. The Laplace transform of the state space is $\mathbf{G}(s) = \mathbf{C}(s\mathbf{I} - \mathbf{A})^{-1}\mathbf{B} + \mathbf{D}$, assuming a certain rack load such that $M_{rack}(t) = c_p\theta_p(t)$, where c_p is the pinion stiffness, and s is the Laplace operator.

The singular values plot of $\mathbf{G}(s)$ and $\mathbf{G}_a(s)$, see [134, pp. 72–79] for definition, is shown in Fig. 2.2(a) for the full and reduced order models, respectively; the optimal *Hankel* model, represented by $\mathbf{G}_a^H(s)$, is also included for comparison. The corresponding model error's singular values plot, defined by $\mathbf{G}(s) - \mathbf{G}_a(s)$, is further illustrated in Fig. 2.2(b). Model order reduction based on the balanced residualization is sufficient if the infinity norm of the error is bounded by the sum of Hankel singular values in Eq. (2.4), where n and k are the actual and reduced number of states, respectively; σ_i represents the Hankel singular values [134, pp. 459–478].

$$\|\mathbf{G}(s) - \mathbf{G}_a^k(s)\|_\infty \leq 2 \sum_{i=k+1}^n \sigma_i \quad (2.4)$$

The infinity norm of the reduced model error is 90.104 rad/Nms at 17.046 rad/s, thus satisfying the upper bound, 160.014 rad/Nms. The primary reason for choosing the above reduced model order rather than minimizing the peak error similar to that in the Hankel model is due to the smaller error at lower frequencies for a more accurate steady state performance. Therefore, this assumption is considered in Chapter 3, Papers A, and E for the controller design but not for the plant model and rack force state estimator.

2.1.2 Steer-by-wire

An SbW system consists of two hardware units: force-feedback and steering rack. The driver interaction port is found on the former, and the environment interaction port on the latter. Each sub-system has of its own actuator input. Simplified models of the FFb and steering rack are presented as follows.

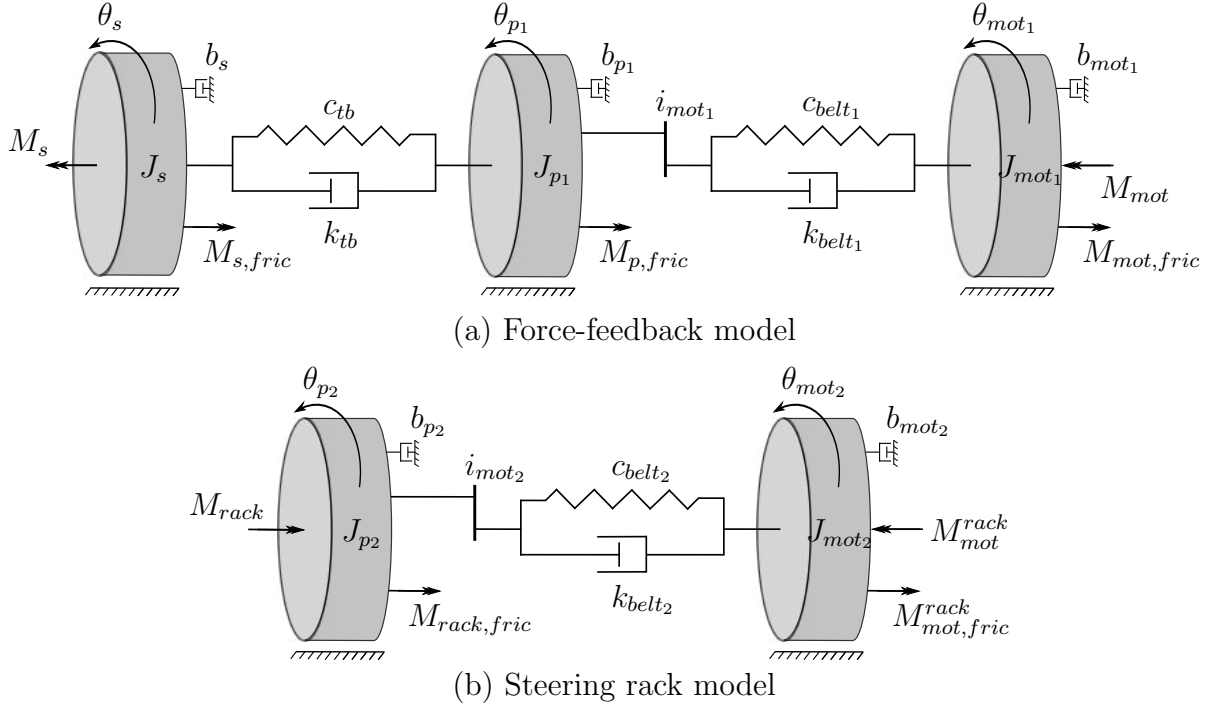


Figure 2.3: Free body diagrams of simplified (a) SbW-FFb with 3-DOF: steering wheel, FFb pinion, and FFb motor; (b) SbW-rack with 2-DOF: RWA pinion and RWA motor.

Force-Feedback (FFb)

The input channels in SbW-FFb are steering torque (M_s) and FFb motor torque (M_{mot}). For the simplified 3-DOF model shown in Fig. 2.3(a), the equations of motion are given by Eq. (2.5):

$$\begin{aligned} J_s \dot{\omega}_s(t) &= -b_s \omega_s(t) - M_{s,fric}(t) - M_{tb}(t) + M_s(t) \\ J_{p1} \dot{\omega}_{p1}(t) &= -b_{p1} \omega_{p1}(t) - M_{p,fric}(t) + M_{tb}(t) + M_{mot,eff}(t) \\ J_{mot1} \dot{\omega}_{mot1}(t) &= -b_{mot1} \omega_{mot1}(t) - M_{mot,fric}(t) - M_{belt1}(t) + M_{mot}(t) \end{aligned} \quad (2.5)$$

where

$$\begin{aligned} M_{tb}(t) &= k_{tb}(\omega_s(t) - \omega_{p1}(t)) + c_{tb}(\theta_s(t) - \theta_{p1}(t)) \\ M_{belt1}(t) &= k_{belt1}(\omega_{mot1}(t) - i_{mot1} \omega_{p1}(t)) + c_{belt1}(\theta_{mot1}(t) - i_{mot1} \theta_{p1}(t)) \quad \text{and} \\ M_{mot,eff}(t) &= i_{mot1} M_{belt1}(t). \end{aligned}$$

The transmission ratio, i_{mot1} , is defined as the FFb motor-to-pinion ratio. The steering angle and velocity are denoted by θ_s and ω_s , respectively; the FFb pinion angle and velocity are denoted by θ_{p1} and ω_{p1} , respectively; the FFb motor angle and velocity are denoted by θ_{mot1} and ω_{mot1} , respectively. The impedance parameters are: steering wheel inertia (J_s), steering column damping (b_s), FFb pinion inertia (J_{p1}), FFb pinion damping (b_{p1}), FFb motor inertia (J_{mot1}), FFb motor damping (b_{mot1}), FFb belt damping (k_{belt1}) and FFb belt stiffness (c_{belt1}). The torsion bar torque is given by M_{tb} such that the torsion bar stiffness is c_{tb} , and torsion bar damping is k_{tb} . The effective motor torque acting on the FFb pinion

2.1. Steering system

is $M_{mot,eff}$, which mechanically depends on the FFb belt torque, M_{belt_1} . Similar to EPAS, the FFb Coulomb friction torques are given by $M_{s,fric}$, $M_{p,fric}$, and $M_{mot,fric}$, as shown in Fig. 2.3(a).

Equation (2.5) is implemented for the FFb plant model (in simulations) and state estimator. However, the FFb belt compliance is again considered as a highly stiff element; hence, it is neglected for the FFb controller design based on the same argument presented in the previous section for EPAS. Consequently, the following simplifications hold for the FFb pinion's equation of motion: $\omega_{mot_1} = i_{mot_1}\omega_{p_1}$ and $M_{mot,eff} = i_{mot_1}M_{mot}$. Moreover, the total FFb pinion Coulomb friction becomes $M_{p,fric} + i_{mot_1}M_{mot,fric}$. The total FFb pinion inertia is $J_{p_1} + J_{mot_1}i_{mot_1}^2$, and the total FFb pinion damping is $b_{p_1} + b_{mot_1}i_{mot_1}^2$. Subsequently, the FFb motor moment balance can be disregarded.

Road Wheel Actuator (RWA)

The input channels in the SbW-rack are steering rack force (F_{rack}) and RWA motor torque (M_{mot}^{rack}). For the simplified 2-DOF model shown in Fig. 2.3(b), the equations of motion are as follows:

$$\begin{aligned} J_{p_2}\dot{\omega}_{p_2}(t) &= -b_{p_2}\omega_{p_2}(t) - M_{rack}(t) - M_{rack,fric}(t) + M_{mot,eff}^{rack}(t) \\ J_{mot_2}\dot{\omega}_{mot_2}(t) &= -b_{mot_2}\omega_{mot_2}(t) - M_{mot,fric}^{rack}(t) - M_{belt_2}(t) + M_{mot}^{rack}(t) \end{aligned} \quad (2.6)$$

where

$$\begin{aligned} M_{belt_2}(t) &= k_{belt_2}(\omega_{mot_2}(t) - i_{mot_2}\omega_{p_2}(t)) + c_{belt_2}(\theta_{mot_2}(t) - i_{mot_2}\theta_{p_2}(t)) \quad \text{and} \\ M_{mot,eff}^{rack}(t) &= i_{mot_2}M_{belt_2}(t). \end{aligned}$$

Again, for convenience, the force balance on the steering rack is translated to the moment balance on the RWA pinion using the rack-to-pinion transmission ratio, i_{rp} . Consequently, the input channel becomes rack torque, defined by $M_{rack} = F_{rack}/i_{rp}$. In the above equations, i_{mot_2} is the RWA motor-to-pinion ratio. The RWA pinion angle and velocity are given by θ_{p_2} and ω_{p_2} , respectively; the RWA motor angle and velocity are given by θ_{mot_2} and ω_{mot_2} , respectively. The impedance parameters are: RWA pinion inertia (J_{p_2}), RWA pinion damping (b_{p_2}), RWA motor inertia (J_{mot_2}), RWA motor damping (b_{mot_2}), RWA belt damping (k_{belt_2}) and RWA belt stiffness (c_{belt_2}). The effective motor torque acting on the RWA pinion is $M_{mot,eff}^{rack}$ as a function of the RWA belt torque, M_{belt_2} . The RWA Coulomb friction torques are given by $M_{rack,fric}$ and $M_{mot,fric}^{rack}$, respectively, as shown in Fig. 2.3(b).

The equivalent rack quantities and/or variables can be defined as follows: $v_{rack} = \omega_{p_2}/i_{rp}$, $m_{rack} = J_{p_2}i_{rp}^2$, $k_{rack} = b_{p_2}i_{rp}^2$, $F_{rack,fric} = i_{rp}M_{rack,fric}$, and $F_{assist} = i_{rp}i_{mot_2}M_{belt_2}$; these notations have the same meaning as those in EPAS.

For the RWA, a typical position controller is implemented. An approach similar to that in EPAS is applied. The RWA belt compliance can be assumed as highly stiff; hence, the following holds: $\omega_{mot_2} = i_{mot_2}\omega_{p_2}$, $M_{mot,eff}^{rack} = i_{mot_2}M_{mot}^{rack}$, and the total RWA pinion friction is $M_{rack,fric} + i_{mot_2}M_{mot,fric}^{rack}$. The total RWA pinion inertia is $J_{p_2} + J_{mot_2}i_{mot_2}^2$, and the total RWA pinion damping is $b_{p_2} + b_{mot_2}i_{mot_2}^2$; subsequently, the RWA motor moment balance can be disregarded. Again, the aforementioned expressions are only assumed for the controller design; otherwise, Eq. (2.6) is implemented for the RWA plant model and state estimator.

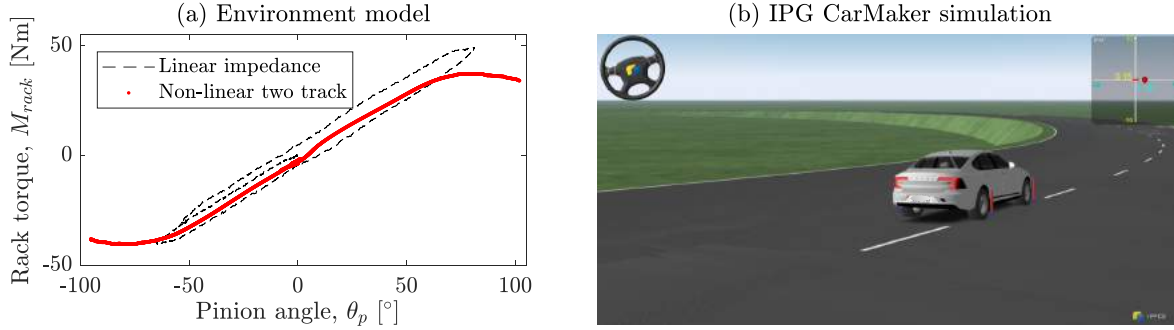


Figure 2.4: (a) Examples of environment models. (b) Screenshot of IPG CarMaker simulation.

2.2 Models for environment interaction

The environment interaction is defined by the rack torque variable, M_{rack} , in Fig. 2.1 and 2.3(b) for EPAS and SbW, respectively. There can be various ways of considering this interaction, depending on how the environment is modeled and at what verification stage.

Linear impedance function

A linear impedance function typically involves a constant spring stiffness at the rack that is suitably translated to the pinion axis such that $M_{rack}(t) = c_p \theta_p(t)$, where c_p is the pinion spring stiffness. This is implemented for a linear analysis and during HIL (hardware-in-the-loop) test rig measurements to tune the controller. An example in which viscous damping is introduced to the system because of HIL rack actuators is shown in Fig. 2.4(a).

Two-track vehicle model

A conventional two-track vehicle model is selected for standalone simulations and verification including a simplified analysis during the controller development. The free body diagram in the global coordinate system is shown in Fig. 2.5. It has 3-DOF: translation in X , translation in Y , and rotation in the XY plane. The non-linear equations of motion with the lateral force balance in the y direction and the yaw moment balance in the z direction (i.e., in the local coordinate system) results in the following expressions:

$$\begin{aligned} m\dot{v}_y(t) &= F_{yf,l}(t) \cos \delta_{f,l}(t) + F_{yf,r}(t) \cos \delta_{f,r}(t) + F_{yr,l}(t) + F_{yr,r}(t) - mv_x \dot{\psi}(t) \\ J_z \ddot{\psi}(t) &= (F_{yf,l}(t) \cos \delta_{f,l}(t) + F_{yf,r}(t) \cos \delta_{f,r}(t))l_f - (F_{yr,l}(t) + F_{yr,r}(t))l_r \end{aligned} \quad (2.7)$$

where v_x is vehicle speed, m is vehicle mass, J_z is yaw inertia, l_f and l_r are the longitudinal distances from the front and rear axles to the vehicle's center of gravity (CG), respectively. The corresponding lateral tire forces are given by $F_{yf,l}$, $F_{yf,r}$, $F_{yr,l}$, and $F_{yr,r}$; the front wheel angles are $\delta_{f,l}$ and $\delta_{f,r}$; the vehicle states are lateral velocity, v_y , and yaw rate, $\dot{\psi}$. A simple relationship between the pinion and front wheel angles is $\delta_{f,l} = \delta_{f,r} = \theta_p / i_{str}$, where i_{str} is the steering ratio. The vehicle body sideslip angle is defined as $\beta = \text{atan}(v_y / v_x)$.

Here, longitudinal vehicle dynamics are neglected for simplicity. Moreover, the model is linearized with respect to a given v_x ; hence, the predefined v_x could be changed to

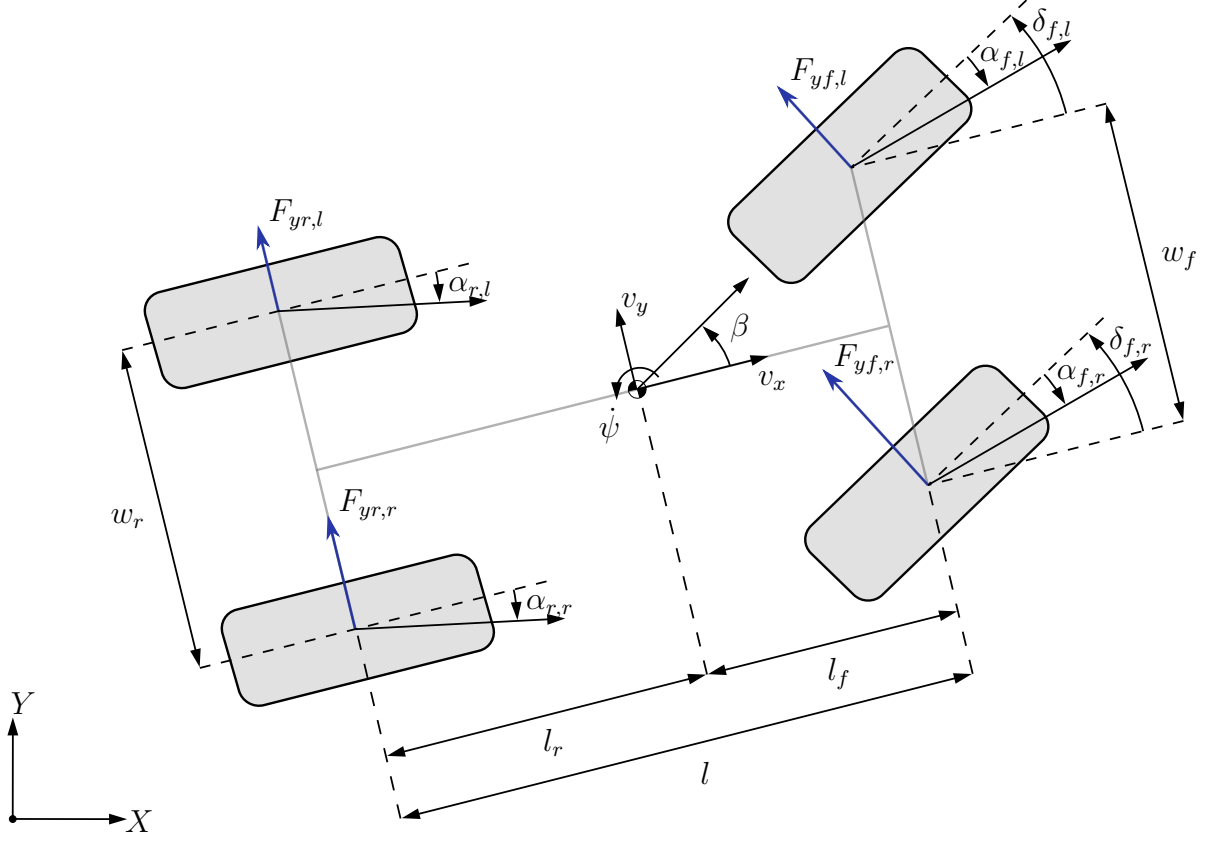


Figure 2.5: Two-track vehicle model in the global coordinate system.

understand the sensitivity at different vehicle speeds. Further details on modeling lateral vehicle dynamics are presented in [135, pp. 20–43].

Based on the geometrical relationships, the lateral tire slip angles ($\alpha_{f,l}$, $\alpha_{f,r}$, $\alpha_{r,l}$, and $\alpha_{r,r}$) are subsequently derived in Eq. (2.8). Typically, the lateral slip angle is required as an input to a tire model for generating the lateral force such that $F_{y,i} = f(\alpha_i)$. Different tire models can be implemented depending on the purpose. The simplest possible model is a linear tire model, defined by $F_{y,i} = C_{\alpha_i} \alpha_i$, where C_{α_i} is the tire cornering stiffness. A linear tire model is only valid for low lateral tire slip angles and consequently for low levels of lateral acceleration, i.e., $a_y(t) = \dot{v}_y(t) + v_x \dot{\psi}(t)$. Another possibility is the use of a non-linear tire model, such as the *tanh* model and the Magic formula or *Pacejka* model [136].

$$\begin{aligned} \alpha_{f,l}(t) &= \delta_{f,l}(t) - \text{atan}\left(\frac{v_y(t) + l_f \dot{\psi}(t)}{v_x - w_f \dot{\psi}(t)/2}\right) & \alpha_{r,l}(t) &= -\text{atan}\left(\frac{v_y(t) - l_r \dot{\psi}(t)}{v_x - w_r \dot{\psi}(t)/2}\right) \\ \alpha_{f,r}(t) &= \delta_{f,r}(t) - \text{atan}\left(\frac{v_y(t) + l_f \dot{\psi}(t)}{v_x + w_f \dot{\psi}(t)/2}\right) & \alpha_{r,r}(t) &= -\text{atan}\left(\frac{v_y(t) - l_r \dot{\psi}(t)}{v_x + w_r \dot{\psi}(t)/2}\right) \end{aligned} \quad (2.8)$$

The Pacejka tire model, which is implemented in this work, is discussed in Section 4.2.1; an example is illustrated in Fig. 2.4(a). The rack torque variable is mathematically related

to the front tire lateral forces, and the corresponding expression is

$$M_{rack}(t) = \frac{1}{i_{str}} ((t_{pf,l}(t) + t_m)F_{yf,l}(t) + (t_{pf,r}(t) + t_m)F_{yf,r}(t)) \quad (2.9)$$

where t_m is the suspension parameter known as mechanical trail and $t_{pf,i}$ is the front tire pneumatic trail [135, pp. 408–409]. For a linear tire model, $t_{pf,i}$ is constant; however, for a non-linear tire model, $t_{pf,i} = f(\alpha_{f,i})$, as described in [137]. Other vehicle suspension effects, such as the tire jacking force and scrub moment, are neglected.

Using a suitable tire model and Eqs. (2.7)–(2.9), the output rack torque/force variable becomes a function of the pinon angle and vehicle speed such that $M_{rack} = f(\theta_p, v_x)$. In a broader context, this implies that the effective pinion stiffness is frequency dependent due to inherent vehicle dynamics and lateral tire slip properties; unlike a constant c_p defined in the linear impedance function. The foregoing is also explicitly discussed in Paper C.

A simplified version of the two-track model is a single-track model [135, pp. 20–43], also described in Paper C. Basically, the left and the right tires can be combined to form an equivalent axle model. It is based on the following assumptions: a linear tire model for the complete axle and small operating angles. Consequently, a state space can be formulated as: $\dot{\mathbf{x}}_{veh}(t) = \mathbf{A}\mathbf{x}_{veh}(t) + \mathbf{B}u_{veh}(t)$, where $\mathbf{x}_{veh}(t) = [v_y \ \psi]^T$ and $u_{veh}(t) = \theta_p$. The resulting state space matrices are as follows.

$$\mathbf{A} = \begin{bmatrix} \frac{C_{\alpha_f} + C_{\alpha_r}}{mv_x} & v_x - \frac{l_r C_{\alpha_r} - l_f C_{\alpha_f}}{J_z v_x} \\ -\frac{l_r C_{\alpha_r} - l_f C_{\alpha_f}}{J_z v_x} & \frac{C_{\alpha_f} l_f^2 + C_{\alpha_r} l_r^2}{J_z v_x} \end{bmatrix} \quad (2.10)$$

$$\mathbf{B} = \begin{bmatrix} \frac{C_{\alpha_f}}{C_{\alpha_f} l_f} \\ \frac{m}{J_z} \end{bmatrix}$$

Accordingly, the rack torque is $M_{rack}(t) = ((t_{pf} + t_m)F_{yf}(t))/i_{str}$, where $F_{yf}(t) = C_{\alpha_f}\alpha_f(t)$. This model is also used in theoretical analysis presented in Paper C.

IPG CarMaker vehicle model

The final verification and validation steps were implemented in IPG CarMaker simulation software before real world experiments were conducted. Figure 2.4(b) shows a screenshot of the simulation of a vehicle driving on closed-circuit proving ground; further details are found in [138]. This software offers various advantages; for example, it provides a high fidelity vehicle model, with lateral and longitudinal load transfers, and multiple DOF (e.g., roll and pitch motions, individual wheel kinematics, and compliance). A non-linear (Magic formula or Pacejka) tire model was also included in this work. More realistic sensor functions were modeled by including specifications pertaining to signal resolution, sampling frequency, and time delay based on the vehicle's controller area network (CAN)-bus.

The simulation setup involved a CarMaker interface with MATLAB/Simulink. The controllers were implemented in MATLAB/Simulink such that the requested motor torque was subsequently communicated to the CarMaker model. The selected solver time step was 1 ms, which was same as the available real-time capabilities and resources for rapid prototyping. This was because the aforementioned controllers were compiled using real-time

interface blocks with the explicit Euler method and then implemented in dSPACE Autobox and MicroAutobox; the experimental setup details are found in Appendix A.

An important remark: the same vehicle-steering plant model in IPG CarMaker was used for different iterations, i.e., varying from open loop to closed-loop control. The EPAS plant model parameters were validated using actual measurements from state-of-the-art Volvo S90 and typical vehicle dynamic maneuvers, such as frequency response, on-center sinus, and slow ramp steer. However, model validation step remains out of context.

This type of a simulation software is useful for reproducing results, particularly for environmental uncertainty. For instance, objectified and consistent comparison can be conducted in case of a tire–road interaction uncertainty scenario that subsequently causes rack force disturbance. In contrast, this is extremely difficult to reproduce in reality using certain disturbance on the proving ground because of several factors, such as varying vehicle speed, conditions, and driver reactions.

2.3 A model for driver interaction

A driver model for steering interactions requires mechanics or impedance of the driver arm. This is required to analyze (the driver port) coupled stability and perform basic steering maneuvers in simulations. Therefore, the simplest driver model form is presented with certain arm stiffness (c_{arm}) and arm damping (b_{arm}) parameters; it is equivalent to an admittance PD controller. The equation of motion for the 1-DOF driver model is as follows:

$$\begin{aligned} J_{arm}\dot{\omega}_s(t) &= M_{arm}(t) - M_s(t) \\ M_{arm}(t) &= b_{arm}(\omega_{s,req}(t) - \omega_s(t)) + c_{arm}(\theta_{s,req}(t) - \theta_s(t)) \end{aligned} \quad (2.11)$$

where J_{arm} is the arm inertia; M_{arm} is the arm torque; $\theta_{s,req}$ and $\omega_{s,req}$ are the requested steering angle and velocity, respectively. Typically, inputs $\theta_{s,req}$ and $\omega_{s,req}$ are provided by the path-following control layer [113, 114], but the requested trajectory is assumed to be already known. Note that a high steady state error, $e_\theta(t) = \theta_{s,req}(t) - \theta_s(t)$, occurs because no integral action is implemented. Therefore, an integrator may be included, if necessary.

Although the driver arm impedance parameters are time-variant [139], but these are considered constant here. The values are adopted from [114] for the worst-case scenario, i.e., a condition under which arm muscles are highly stiff or tensed. This is because intrinsic muscle stiffness and reflex gain for evasive maneuvers and high frequency steering inputs are higher as compared to a relaxed muscle condition. This implies rigid coupling between driver arm inertia and steering wheel inertia, which is important for the stability of a haptic controller during human interaction, as discussed in Papers A and B. Analytically, $\omega_{s,req} = 0$ rad/s is the prerequisite condition for coupled stability, given $\theta_{s,req}$. Under a zero initial condition, the driver model impedance function can be defined as follows.

$$G_{drv}(s) = \frac{M_s(s)}{\omega_s(s)} = -\left(J_{arm}s + b_{arm} + \frac{c_{arm}}{s} \right) \quad (2.12)$$

The above expression implicitly indicates that the effective steering system input is M_{arm} , and the total inertia on the steering wheel becomes $J_{arm} + J_s$ for stability, performance, and robustness analyses.

3 Steering feedback control

The physical human-machine interaction defines the *haptic* feedback in a mechatronic system [8]. The corresponding interaction is provided through an HMI, and the haptic regulation is referred to as interaction control [31]. Although the performance of HMI devices is subjectively evaluated, the controller development has to be objective. Moreover, different stability aspects (e.g., with and without human interaction) must be ensured.

For road vehicles, the haptic interaction between the driver and steering is defined as steering feedback. Subsequently, the servo motor connected to the steering system can be used to manipulate the steering feedback as required. Accordingly, this chapter introduces different control methods to achieve that purpose. The underlying principles differ in terms of how the motor torque control law is defined.

Initially, a brief explanation on the interaction dynamics between driver, steering system, and environment is presented. This is important for thoroughly understanding the system dynamics, before considering the controller details. Regarding the control methods, the state-of-the-art (i.e., open loop) strategy is first introduced, and its drawbacks are addressed. Then, closed-loop solutions are proposed with two causalities: torque and position control. For each closed-loop method, the following aspects are discussed and compared: linear stability, tracking performance, and robustness.

3.1 Interaction dynamics

An EPAS system constitutes of a hardware responsible for both the driver and environment interactions. The respective interaction ports are at the steering wheel and steering rack. In robotics, similar examples of different exoskeletons in which the *leader* device is responsible for both human-machine and machine-environment interactions are observed [23, 30, 31, 46, 47, 49]. For EPAS, a causal representation of haptic interaction is shown in Fig. 3.1(a). Other driver feedback cues: optical, acoustical, and motion are excluded for simplicity. The torque or force and velocity exchange variables represent a physical causality obtained by combining the steering model presented in Section 2.1.1, environment model in Section 2.2 and driver model in Section 2.3. Thus, the steering system inputs are driver torque (M_s), rack force (F_{rack}), and motor torque (M_{mot}).

An SbW system represents a *leader-follower* configuration. The driver interaction port is on the leader device (i.e., the steering wheel), whereas the follower (i.e., the steering rack) constitutes the environment interaction port. These configurations with physically separated (human-machine and machine-environment) interaction ports are common in robotics and used for teleoperation purposes, see e.g. [8, 12, 65, 73, 140, 141]. The FFb model presented in Section 2.1.2 and driver model in Section 2.3 are used for the driver interaction. The steering rack model presented in Section 2.1.2 and environment model in Section 2.2 for the environment interaction. The resulting causal representation can be seen in Fig. 3.1(b). As a result, the FFb system inputs are driver torque (M_s) and FFb motor torque (M_{mot}); the steering rack inputs are rack force (F_{rack}) and RWA torque (M_{mot}^{rack}).

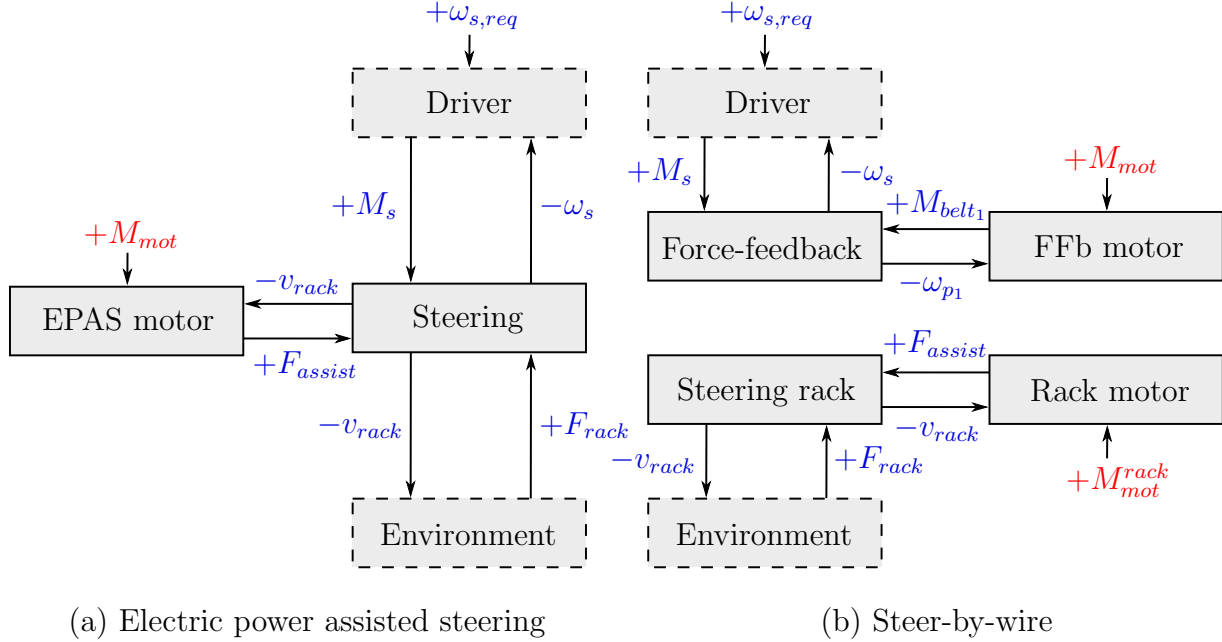


Figure 3.1: A mechanical causal representation of the driver–steering and environment–steering interactions for (a) EPAS and (b) SbW systems, respectively.

The driver interaction performance defines the required steering feedback. In reality, it is based on an individual’s perception, the driver arm impedance, other feedback cues, etc.; hence, different subjective interpretations may be drawn. However, an objective assessment of the steering feedback is attempted depending on the excitation signal for a single-input single-output (SISO) characteristic. Therefore, each possibility has different boundary conditions, see Table 3.1, as elaborated next.

With driver excitation, the system is persistently excited through M_s without any environmental uncertainty. In this case, $F_{rack}(t) = f(v_{rack})$ is the boundary condition for anticipated vehicle and tire response using typical vehicle dynamic maneuvers, such as frequency response, on-center sinus, ramp steer, and lane change, under flat and dry road surface conditions [29]. The relationship between $M_s(t)$ and $\theta_s(t)$ defines the driver’s haptic performance.

With environmental excitation, F_{rack} becomes the disturbance input, and the driver is coupled to the steering system (Table 3.1). The boundary condition is $\omega_{s,req}(t) = 0$ rad/s for the driver model, thus keeping a fixed steering angle under a given initial condition. Some examples are driving on a varying tire–road friction surface, rough road conditions, and cornering near the uncertain vehicle–tire handling limits. Accordingly, *transparency* for evaluating the road feedback performance can be defined, that is, to what degree and how much frequency content of F_{rack} can be transmitted and reflected back to the driver in the steering torque. The leader–follower configuration is inherently *non-transparent*, and so as SbW. Therefore, control algorithms are required to achieve transparency.

The culmination of the above cases can be used to analyze the effect of motor torque excitation on steering torque (Table 3.1); thereby, coupling the driver and environment is assumed such that $\omega_{s,req}(t) = 0$ rad/s under a given initial condition and $F_{rack}(t) = f(v_{rack})$.

Table 3.1: Performance measure: Objective definition of steering feedback

Excitation source	Input	Output	Condition
Driver	M_s	ω_s	Coupled environment, s.t. $F_{rack} = f(v_{rack})$
Environment*	F_{rack}	M_s	Coupled driver, s.t. $\omega_{s,req} = 0$ rad/s
Motor	M_{mot}	M_s	Coupled driver, s.t. $\omega_{s,req} = 0$ rad/s and coupled environment, s.t. $F_{rack} = f(v_{rack})$

*This case defines the steering feedback transparency.

Table 3.2: Stability measure for a given interaction port and its admittance function

Interaction port	Admittance	Condition
Driver	$\omega_s(s)/M_s(s)$	Uncoupled environment, s.t. $F_{rack} = 0$ N
Driver	$\omega_s(s)/M_s(s)$	Coupled environment, s.t. $F_{rack} = f(v_{rack})$
Environment	$v_{rack}(s)/F_{rack}(s)$	Uncoupled driver, s.t. $M_s = 0$ Nm
Environment	$v_{rack}(s)/F_{rack}(s)$	Coupled driver, s.t. $\omega_s = \omega_{s,req} = 0$ rad/s

This case, in particular, could be used to analyze the effect of an ADAS request (via M_{mot} channel) and/or the influence of motor torque disturbance on the steering feedback.

Before seeking to achieve high performance, the important aspect of a haptic controller is stability. Table 3.2 summarizes the different cases for ensuring stable interaction with driver and environment models. The driving and environment port admittance transfer functions are given by $\omega_s(s)/M_s(s)$ and $v_{rack}(s)/F_{rack}(s)$, respectively. Both coupled and uncoupled stability should be analyzed, because two uncoupled and isolated stable systems could result in an unstable closed-loop interconnection upon coupling at the given port [31].

For analyzing stability at the driver interaction port, the environment model could be either coupled (i.e., $F_{rack} = f(v_{rack})$) or uncoupled (i.e., $F_{rack} = 0$ N). Similarly, the driver model can be considered either uncoupled (i.e., a free steering wheel and $M_s = 0$ Nm) or coupled (such that $\omega_{s,req}(t) = 0$ rad/s) to achieve stable environment interaction, as defined in Table 3.2. Here, the coupled driver scenario assumes an *ideal* driver model such that $\omega_s = \omega_{s,req}$, for simplicity; implying a fixed steering wheel condition, i.e., $(\theta_s, \omega_s) = (0, 0)$.

The subsequent sections and chapters refer to this subsection, particularly Tables 3.1 and 3.2, in discussing a given test scenario for performance evaluation and deriving the required stability conditions.

3.2 State of the art: Open loop

The “open loop” control strategy directly manipulates hardware dynamics without *error minimization* in the inner loop. This is to achieve a desired impedance behavior by minimizing the effect of the actual impedance; thus defining the device’s *transparency*. This is subsequently elaborated according to the steering system dynamics (EPAS or SbW-FFb).

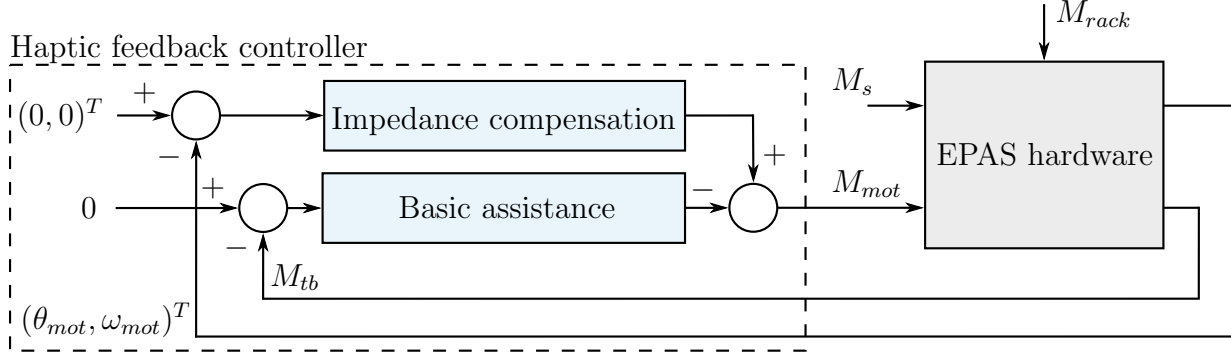


Figure 3.2: EPAS open loop control strategy.

3.2.1 Electric power assisted steering control

A simplified open loop EPAS control, basically representing an impedance manipulation with two primary functions, is shown in Fig. 3.2. They are described as follows. Here, other sophisticated “steering feel” functions, such as active return, disturbance compensation, and understeer/oversteer correction, are excluded. Further information about them can be found in [29, 75, 87].

The *basic assistance* function is a *non-linear* P-controller for the measured torque with a null reference. The aim of the function is to achieve a desired quasi-static force/moment balance between M_{tb} , M_{mot} , and M_{rack} at a given vehicle speed. It intuitively implies how much driver torque should be applied at a certain rack force and vehicle speed. The mathematical representation is as follows

$$M_{mot,1}(t) = f_1(M_{tb}(t), v_x) = K_{assist}(M_{tb}(t), v_x)M_{tb}(t), \text{ s.t. } K_{assist} > 0 \quad (3.1)$$

where K_{assist} is non-linear gain dependent on M_{tb} and v_x . Although the discussion of the shape of K_{assist} is avoided, note that it has evolved over the years since its introduction to the hydraulic power assisted systems as stated in [29, 142] and Paper C. One probable reason for its non-linear characteristic could be attributed to the driver’s steering posture and corresponding limb movements during the arm’s muscular activity [143].

The impedance compensation function is a combination of three sub-functions to explicitly compensate for hardware dynamics through inertia, viscous damping, and Coulomb friction parameters. The *inertia compensation* function is necessary to compensate for the motor inertia, which has a significant influence on transparency¹. For this purpose, this work relies on the estimated motor acceleration ($\hat{\omega}_{mot}$) or equivalently the estimated pinion acceleration ($\hat{\omega}_p$), assuming that the belt compliance is neglected. Equation (3.2) defines the control actuation, where J_{comp} is the compensating inertia, which may be dependent on v_x . For an analytical explanation, $\hat{\omega}_{mot}(t) \approx \dot{\omega}_{mot}(t)$ is presumed. In reality, this is a broad assumption considering the noise and time delay in the $\hat{\omega}_{mot}$ signal. Moreover, closed-loop

¹Higher effective system inertia/mass implies reduced (high frequency) transparency due to low mechanical eigenfrequency, thus inheriting a low frequency low-pass filter characteristic.

stability could be affected. Hence, this function has certain practical implications and performance limitations.

$$M_{mot,2}(t) = f_2(\hat{\omega}_{mot}(t), v_x) = -J_{comp}(v_x)\hat{\omega}_{mot}(t) \approx -J_{comp}(v_x)\dot{\omega}_{mot}(t) \quad (3.2)$$

The *active damping* function controls the system's overall viscous damping, particularly for avoiding any steering wheel overshoot. The motor torque, given in Eq. (3.3) is a function of ω_{mot} and v_x . The compensating damping coefficient, b_{comp} , may also be parameterized as a function of θ_{mot} ; however, this is avoided for simplicity.

$$M_{mot,3}(t) = f_3(\omega_{mot}(t), v_x) = -b_{comp}(v_x)\omega_{mot}(t) \quad (3.3)$$

The *friction compensation* function reduces mechanical Coulomb friction to achieve a desired on-center steering feedback [144]. Although Coulomb friction is highly non-linear, it can only be compensated to a certain extent with a discrete solution for real-time compatibility. The Dahl friction model [145], consisting of two friction effects (pre-sliding and hysteresis), is implemented. The corresponding motor torque is a function of the compensating motor friction torque, $M_{mot,fric}^{comp}$, given by

$$M_{mot,4}(t) = f_4(\omega_{mot}(t), v_x) = M_{mot,fric}^{comp}(t) \quad (3.4)$$

$$\text{where } f_4 := \frac{d}{dt}(M_{mot,fric}^{comp}(t)) = c_{mot,fric} \left(\omega_{mot}(t) - \frac{M_{mot,fric}^{comp}(t)}{M_{mot,fric}^0(v_x)} |\omega_{mot}(t)| \right), \quad (3.5)$$

$M_{mot,fric}^0$ is the peak compensating motor friction torque, and $c_{mot,fric}$ is the motor's friction model stiffness. Ideally, friction model stiffness should be high; however, it is limited by the discrete time step to avoid numerical instability and limit cycle [146, 147].

The *active return* function ensures that a desired steering wheel trajectory toward the on-center position during a free steer release (i.e., an uncoupled driver port) at an offset steering angle is achieved. It operates as a position and/or velocity controller with null reference states. Similarly, other functions are implemented based on their specific operation and added to the motor torque, assuming that it is given by $M_{mot,5}$. Accordingly, open loop control is defined as the summation of the aforementioned motor torque components, thus resulting in

$$M_{mot}(t) = K_{assist}M_{tb}(t) - J_{comp}\dot{\omega}_{mot}(t) - b_{comp}\omega_{mot}(t) + M_{mot,fric}^{comp}(t) + M_{mot,5}(t). \quad (3.6)$$

The typical open loop control architecture, shown in Fig. 3.2, is primarily tuned to achieve a desired haptic response within 5 Hz, i.e., maximum periodic driver excitation frequency [83]. However, for the transparent steering feedback during the rack force excitation, the limitation of EPAS becomes evident due to an attenuated haptic response [29]. In general, coupling a passive system with a servo motor results in a higher overall mechanical impedance [30, 47]. This effect is further amplified by the square of the transmission ratio between the motor and rack/pinion (if any). Hence, the equivalent system mass/inertia increases, as described in Paper A. To mitigate this effect, the inertia compensation function is explicitly implemented.

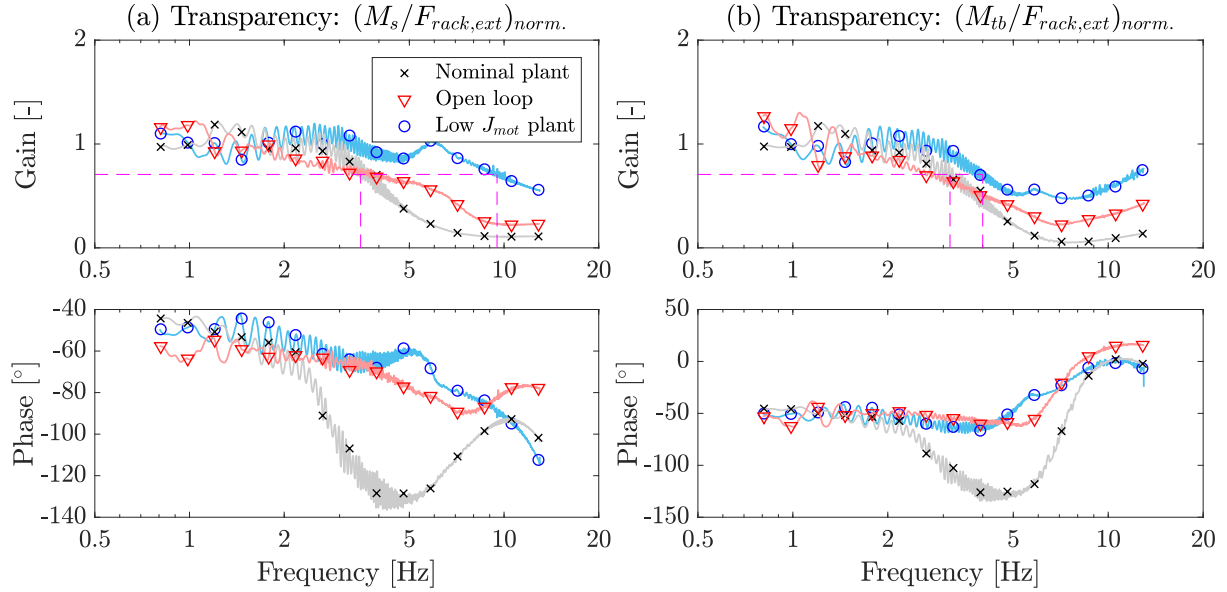


Figure 3.3: Simulated transparency result of open loop EPAS: normalized $M_s(s)/F_{rack,ext}(s)$ and $M_{tb}(s)/F_{rack,ext}(s)$ frequency responses at 75 km/h. The normalization is done with respect to the corresponding steady state gain. The magenta lines (---) define the transparency bandwidth.

However, it continues to cause an immense high frequency driver–environment transparency loss, which may contain useful tire–road feedback information.

Assume an infinitely stiff belt compliance such that $\omega_p = \omega_{mot}/i_{mot}$. Using the pinion’s equation of motion from Eq. (2.2) and the control law in Eq. (3.6) as well as neglecting $M_{mot,5}$, the closed-loop formulation is given by Eq. (3.7), where $J_{p,eff} = J_p + i_{mot}^2 J_{comp}$, $b_{p,eff} = b_p + i_{mot}^2 b_{comp}$, $M_{p,fric}^{eff} = M_{p,fric} - i_{mot} M_{mot,fric}^{comp}$, and $K'_{assist} = 1 + K_{assist} i_{mot}$. Thus, the driver–steering interaction depends on these effective parameters [31], i.e., $J_{p,eff}$, $b_{p,eff}$, $M_{p,fric}^{eff}$, and K'_{assist} . For the given system, $J_{comp} < 0$ and $b_{comp} > 0$, which imply reducing pinion inertia and increasing pinon damping, respectively, to achieve the desired response.

$$\begin{aligned} J_p \dot{\omega}_p(t) &= -b_p \omega_p(t) - M_{p,fric}(t) - M_{rack}(t) + M_{tb}(t) + i_{mot} M_{mot}(t) \\ \implies J_{p,eff} \dot{\omega}_p(t) &= -b_{p,eff} \omega_p(t) - M_{p,fric}^{eff}(t) - M_{rack}(t) + K'_{assist} M_{tb}(t) \end{aligned} \quad (3.7)$$

The importance of $J_{p,eff}$ on the driver–environment transparency using simulation results from IPG CarMaker is further discussed. The nominal plant includes a state-of-the-art steering model from [148] with an open loop software function to perform software-in-the-loop (SIL) tests. The normalized $M_s(s)/F_{rack,ext}(s)$ and $M_{tb}(s)/F_{rack,ext}(s)$ frequency response functions (FRFs) are shown in Fig. 3.3, where $F_{rack,ext}$ is the rack force excitation input. The former exhibits the response on the steering wheel, and the latter represents the pinion response (i.e., what is actually measured and eventually controlled). These responses are normalized using their steady state gains, which are approximately given by K'_{assist} , to focus on high frequencies. The nominal plant without an active control ($M_{mot} = 0$ Nm) understandably has a damped response². With open loop control, transparency improves

²It can also be expressed in terms of bandwidth, i.e., the frequency with a gain -3 dB or 0.707.

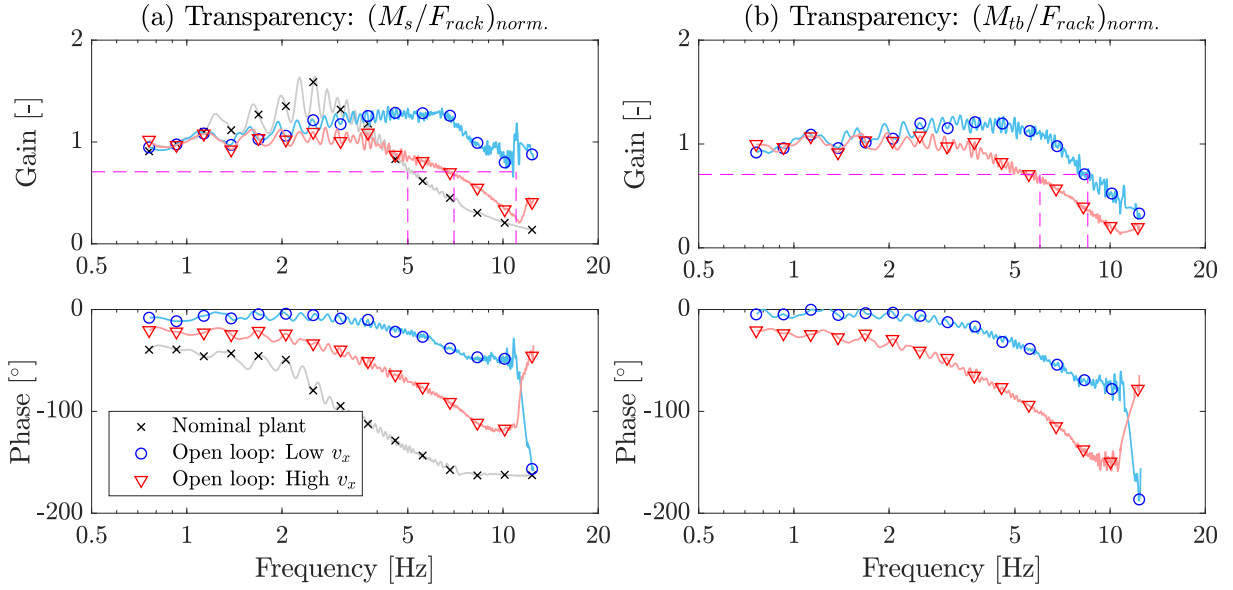


Figure 3.4: HIL test rig transparency result of open loop EPAS: normalized $M_s(s)/F_{rack}(s)$ and $M_{tb}(s)/F_{rack}(s)$ frequency responses. The open loop control FRF responses are shown for two vehicle speeds: 0 km/h and 75 km/h. Normalization is done with respect to the corresponding steady state gain. The magenta lines (---) define the transparency bandwidth.

because of the less attenuated gain response and low phase delay. Although the bandwidth is similar to that of the nominal plant, $\omega_c \approx 22.62$ rad/s, the high frequency gain is higher due to inertia compensation. To illustrate this further, consider a hypothetical case in which J_{mot} is reduced and motor control is absent. Due to low system inertia, the high frequency response is inherently more transparent and faster because $\omega_c \approx 59.69$ rad/s in Fig. 3.3(a).

The above theory can also be corroborated in practice. With an external rack force excitation, the following experiments on a HIL test rig were performed. The rig was equipped with two external rack force actuators, mechanically connected to the steering tie-rods and force sensors. The excitation was generated on one of the actuators in the position control mode with a sine sweep signal in the rack position, whereas the other actuator simulated a linear impedance function (Section 2.2) with 70 Nm/rad as pinion stiffness. For deriving the transparency results, the steering wheel was externally controlled to a fixed zero initial position using a steering robot such that $(\theta_{s,req}, \omega_{s,req}) = (0, 0)$.

The normalized $M_s(s)/F_{rack}(s)$ and $M_{tb}(s)/F_{rack}(s)$ FRF responses are shown in Fig. 3.4. Again, steady state gain normalization is performed for comparing high frequency behavior. The nominal plant has an overshoot and exhibits the slowest response with $\omega_c = 31.42$ rad/s, shown in Fig. 3.4(a); correspondingly $M_{tb}(s)/F_{rack}(s)$ FRF does not exist because the EPAS motor and entire CAN-bus were disabled. With open loop control, the response is faster, overshoot is reduced, and transparency is higher due to the state-of-the-art functions. The cut-off frequencies are 69.12 rad/s and 43.98 rad/s at low and high vehicle speeds, respectively, for the given control setting. A similar qualitative observation can be made from Fig. 3.4(b). The key point is that a lower $J_{p,eff}$ is required to achieve higher steering feedback transparency and a less attenuated high frequency response in $M_s(s)/F_{rack}(s)$ and

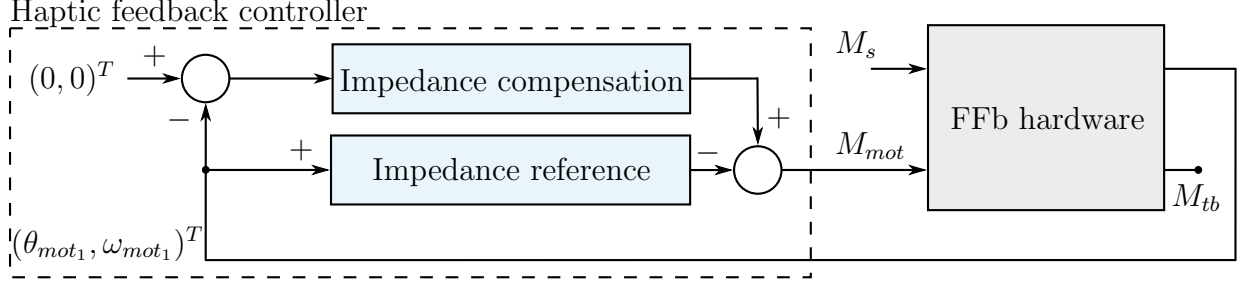


Figure 3.5: SbW-FFb open loop control strategy.

$M_{tb}(s)/F_{rack}(s)$. Based on this analysis, two questions emerge. How can the closed-loop steering feedback control architecture be defined? How can transparency be achieved in closed-loop control?

3.2.2 Steer-by-wire force-feedback control

An open loop SbW-FFb control example, including impedance reference and compensation functions, is shown in Fig. 3.5. Although this configuration is inherently non-transparent toward environment interaction, it is not discussed here; only the FFb device and its open loop control algorithm are covered.

The impedance compensation function involves manipulating the FFb system parameters: *inertia*, *damping*, and *Coulomb friction*. The goal is to minimize the effect of hardware impedance such that a target impedance reference is tracked as closely as possible. Typically, as a straightforward solution, it can be excluded [93, 94, 149]; otherwise, the required motor torque is formulated as follows

$$M_{mot,1}(t) = -J_{comp}\dot{\omega}_{mot1}(t) - b_{comp}\omega_{mot1}(t) + M_{mot,fric}^{comp}(t) \quad (3.8)$$

where $M_{mot,fric}^{comp}$ is the compensating friction torque computed using Eq. (3.5); J_{comp} and b_{comp} are the compensating inertia and damping parameters, respectively.

Assuming a stiff motor to pinion connection, the reference torque ($M_{tb,ref}$) is defined using the *impedance reference* function. The input signals are the trajectory variables, i.e., angular position, velocity, and acceleration, such that

$$M_{mot,2}(t) = -\frac{1}{i_{mot1}}M_{tb,ref}(t) = -\frac{1}{i_{mot1}}(J_{ref}\dot{\omega}_{p1}(t) + b_{ref}\omega_{p1}(t) + c_{ref}\theta_{p1}(t)) \quad (3.9)$$

where J_{ref} , b_{ref} , and c_{ref} are the reference inertia, damping, and stiffness parameters, respectively; and $\omega_{p1} = \omega_{mot1}/i_{mot1}$. Equation (3.9) determines the required haptic feedback. The overall control law is the summation of Eqs. (3.8) and (3.9). Consequently, the FFb-pinion's equation of motion, from Eq. (2.5), can be resolved as following, where $J_{p,eff} = J_{p1} + i_{mot1}^2 J_{comp}$, $b_{p,eff} = b_{p1} + i_{mot1}^2 b_{comp}$, and $M_{p,fric}^{eff} = M_{p,fric} - i_{mot1} M_{mot,fric}^{comp}$.

$$(J_{p,eff} + J_{ref})\dot{\omega}_{p1}(t) = -(b_{p,eff} + b_{ref})\omega_{p1}(t) - c_{ref}\theta_{p1}(t) - M_{p,fric}^{eff}(t) + M_{tb}(t) \quad (3.10)$$

In the above formulation, $J_{comp} < 0$ and $b_{comp} < 0$ should be applied such that the hardware impedance parameters, J_{p1} and b_{p1} , cause minimal high frequency distortion. For

3.3. Closed-loop strategy

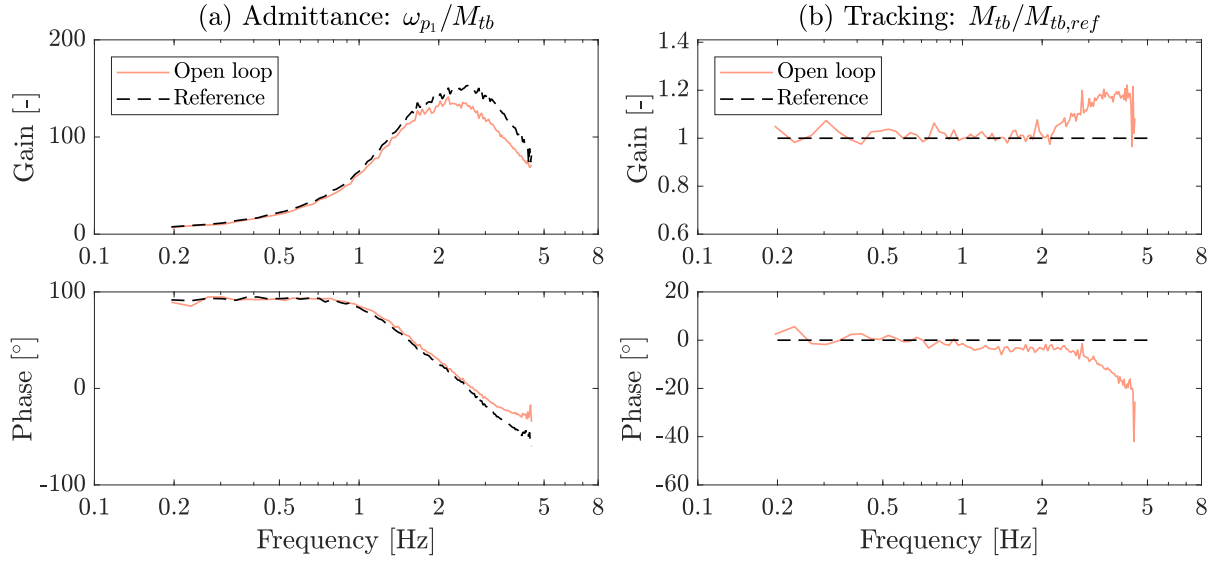


Figure 3.6: Open loop SbW-FFb test result: (a) measured admittance FRF, $\omega_{p1}(s)/M_{tb}(s)$; and (b) tracking FRF, $M_{tb}(s)/M_{tb,ref}(s)$.

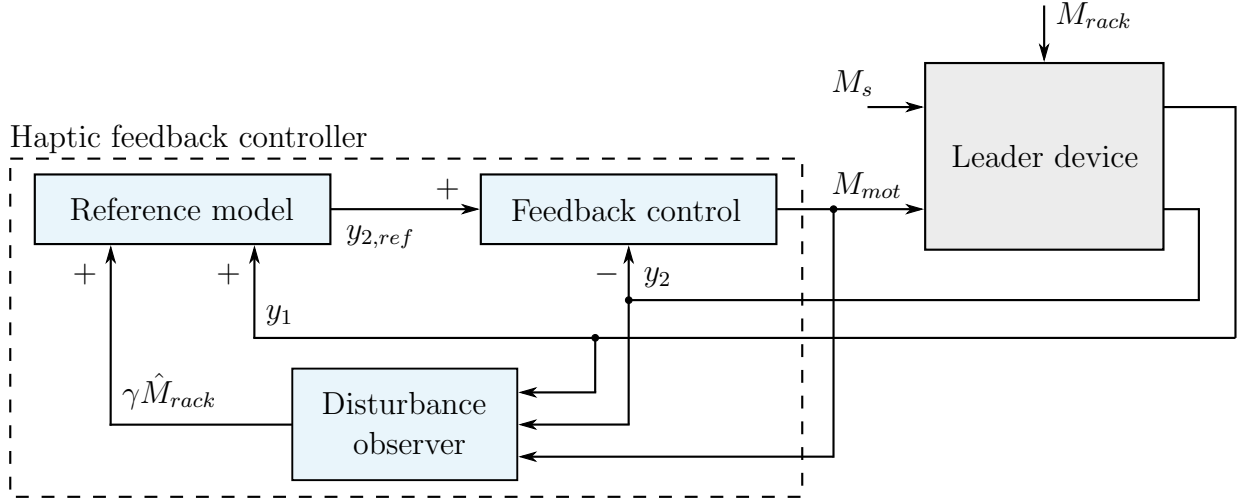
ideal reference tracking, $J_{p,eff} = 0 \text{ kgm}^2$ and $b_{p,eff} = 0 \text{ Nms/rad}$ are required. However, in reality, the above is difficult to achieve in open loop control due to the estimation of $\dot{\omega}_{mot1}$, measurement noise in ω_{mot1} and/or parametric uncertainties.

Consider a measurement where the impedance compensation function was deactivated and the steering wheel excitation was performed by the driver. Moreover, J_{ref} , b_{ref} , and c_{ref} were predefined for a certain (virtual) haptic feedback. The corresponding measured admittance FRF response is shown in Fig. 3.6(a); here, the impedance reference operator is defined by the inverse of $\omega_{p1}(s)/M_{tb,ref}(s) = (J_{ref}s + b_{ref} + c_{ref}/s)^{-1}$ in the Laplace domain. The high frequency reference tracking (i.e., exceeding 2 Hz) deteriorates as shown in Fig. 3.6(a) and 3.6(b), because of the uncompensated FFb hardware impedance parameters, J_{p1} and b_{p1} .

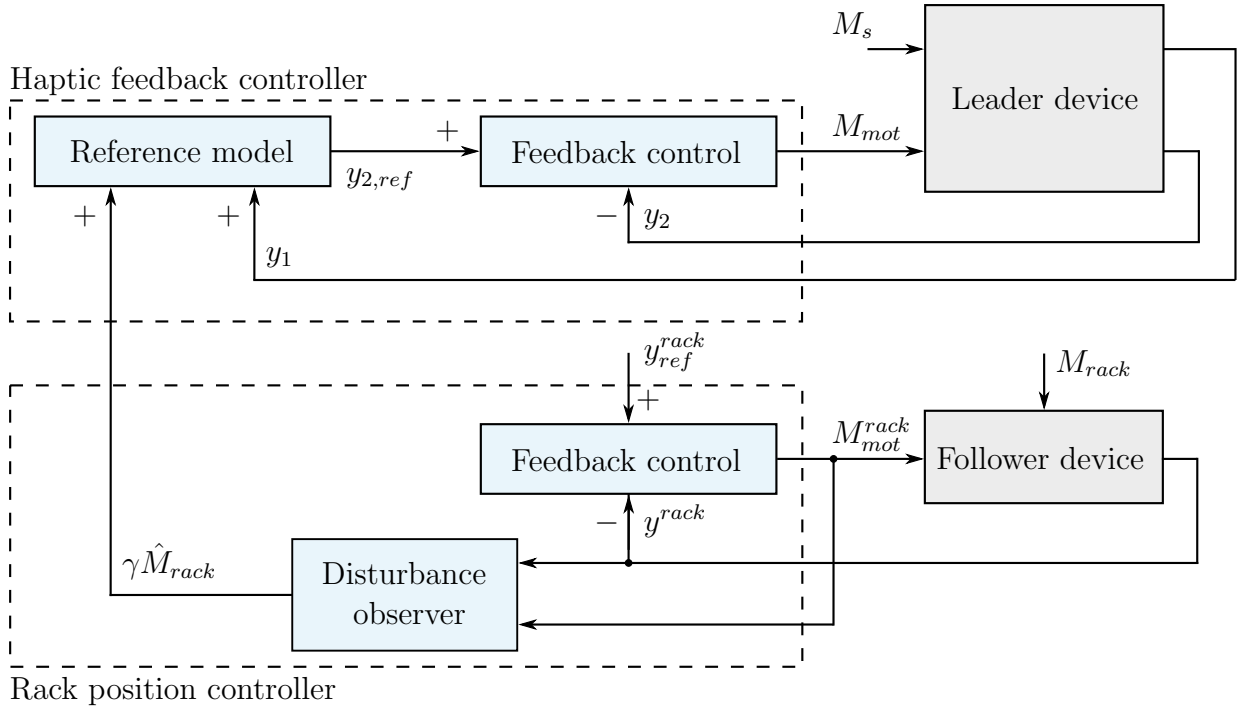
Even with the impedance compensation function, the reference tracking can only be improved up to a certain extent in the low frequency range; it remains insufficient to achieve a desired behavior up to 20 Hz, which is the steering feedback transparency requirement [150]. Therefore, a better SbW-FFb control solution with higher bandwidth is sought. Hence, the following questions are investigated. How much tracking performance can be improved using the closed loop method? How could the reference be formulated for transparency in closed-loop control?

3.3 Closed-loop strategy

Closed-loop control methods are defined when the reference signal is tracked by error minimization. As described in Chapter 1, two closed-loop concepts are under consideration: torque and position control. Regardless of the system dynamics, the primary benefit is hardware independent haptic feedback response such that the same higher level control (or



(a) Electric power assisted steering control



(b) Steer-by-wire force-feedback and rack control

Figure 3.7: Generic closed-loop steering feedback control architecture for (a) EPAS and (b) SbW. The two-channel bilateral SbW control architecture consists of a leader (FFb) and a follower (steering rack or RWA).

the reference model) can be executed in different environments (e.g., driving simulators and closed-loop vehicle steering systems). This approach, as compared to open loop control, is more intuitive in tuning the steering feedback because of the model-based architecture.

Typical closed-loop haptic feedback control architectures for EPAS (including rehabilitation robots) and SbW (as well as telerobotic devices) are shown in Fig. 3.7(a) and 3.7(b), respectively. Two interconnected loops, inner and outer, are formulated for error minimization and reference generation, respectively; examples are reported in [43, 47, 49, 151, 152]. Three input channels are found in EPAS (i.e., a leader): one for the actuator and two interaction ports (human and environment). Whereas in SbW, a leader (SbW-FFb) has two input channels: human interaction port and for the FFb actuator; moreover, a follower (SbW-rack) has two input channels: environment interaction port and for the RWA. With respect to the leader device, closed-loop control requires the measured signals of torsion bar torque and pinion angular position for non-transparency. Because one of them is used to generate the reference for the other variable; the error (i.e., the difference between reference and actual variables) is subsequently minimized in the feedback control block, as it can be observed in the haptic feedback controller shown in Fig. 3.7. Consequently, the two approaches are complimentary due to causality inversion.

In torque control, the outer loop generates the reference torque using the measured angular position through virtual impedance³. On the contrary, the measured torque generates the reference angular position through virtual admittance in position control. This is true for a virtual (or non-transparent) haptic reference variable. For transparency, the estimated rack torque \hat{M}_{rack} (representing the estimated environment interaction dynamics) is assumed to be known by the disturbance observer block in Fig. 3.7. It is further multiplied with a time-invariant transparency gain, γ , as feedback to the reference model. As a result, the torque and position reference variables ($M_{tb,ref}$ and $\theta_{p,ref}$, respectively) can be expressed in the Laplace domain for further analysis, as follows:

$$\begin{aligned} M_{tb,ref}(s) &= (J_{ref}s^2 + b_{ref}s + c_{ref})\theta_p(s) + \gamma\hat{M}_{rack}(s) \\ &= H_{ref}^{-1}(s)\theta_p(s) + \gamma\hat{M}_{rack}(s) \end{aligned} \quad (3.11)$$

and

$$\begin{aligned} \theta_{p,ref}(s) &= (J_{ref}s^2 + b_{ref}s + c_{ref})^{-1}(M_{tb}(s) - \gamma\hat{M}_{rack}(s)) \\ &= H_{ref}(s)(M_{tb}(s) - \gamma\hat{M}_{rack}(s)) \end{aligned} \quad (3.12)$$

where J_{ref} , b_{ref} , and c_{ref} are the reference inertia, damping, and stiffness parameters; the torque (or impedance) and position (or admittance) reference transfer functions are $H_{ref}^{-1}(s)$ and $H_{ref}(s)$, respectively. Although the implemented reference model, discussed in Chapter 4, is more complicated than the aforementioned equations, in principle, it has the same meaning. Two important conditions must be considered: $\gamma = 0$ (for non-transparency), and $\gamma > 0$ (for transparency); note that $\gamma = 1$ means full transparency.

For SbW-FFb, the above definitions and the following results are the same; only the notations have to be modified by replacing θ_p , ω_p , J_p , b_p , and i_{mot} with θ_{p1} , ω_{p1} , J_{p1} , b_{p1} , and

³The impedance operator is defined as the transfer function between torque and angular velocity in a power-continuous coupling and vice versa for the admittance operator [31].

i_{mot_1} , unless stated otherwise. This is because the two leader devices are exactly the same when M_{rack} is null. A position controller for the SbW-rack (or RWA) implies $y_{ref}^{rack}(t) = \theta_{p_1}$ and $y^{rack}(t) = \theta_{p_2}$ for a response similar to that in EPAS, as shown in Fig. 3.7(b).

Stability can be studied from both uncoupled and port-coupled perspectives. Uncoupled stability is defined for the system's isolated behavior, whereas a haptic feedback controller interacting with either a human or an environment or both defines coupled stability. Uncoupled stability is evaluated for two cases. First, for the inner loop with and without a (non-transparent) reference model. Second, given the inner loop tracking, the boundary condition of a reference parameter is determined in the outer loop. A small loop gain is ideally sufficient for stability from the small gain arguments or according to the small gain theorem [134, pp. 155–156], although in a conservative manner. This implies that the shape of the loop transfer function with the given reference model mainly depends on the reference stiffness and inertia in torque and position control, respectively, as also reported in [49, 64, 68]. Consequently, the non-transparent torque and position loop gains ($L_M(s)$ and $L_\theta(s)$, respectively) are defined as

$$\begin{aligned} L_M(s) &= H_{fb,M}(G_M(s) - H_{ref}^{-1}(s)G_\theta(s)) \\ L_\theta(s) &= H_{fb,\theta}(G_\theta(s) - H_{ref}(s)G_M(s)) \end{aligned} \quad (3.13)$$

where $G_M(s) = M_{tb}(s)/M_{mot}(s)$ and $G_\theta(s) = \theta_p(s)/M_{mot}(s)$ are nominal plant model transfer functions; $H_{fb,M}(s)$ and $H_{fb,\theta}(s)$ are torque and position feedback control transfer functions, respectively.

Uncoupled stability does not guarantee coupled stability [30]; hence, the latter is analyzed under non-transparency using the passivity definition. The human coupled instability associated with a haptic controller (also known as contact instability) is a well-known phenomenon, particularly in position control [49, 140]. The main reason for such instability is high coupling impedance. Taking a step further toward coupled stability under transparency, an upper bound condition is derived for the transparency gain, defined by $\bar{\gamma}$, assuming that the driver is part of system dynamics, refer Table 3.2. The linear control theory is used for stability analysis throughout the chapter. First, torque control is presented, then followed by position control.

3.4 Torque control

The torque control architecture implies that $y_2(t) = M_{tb}$, $y_1(t) = \theta_p$ and $y_{2,ref}(t) = M_{tb,ref}$, in Fig. 3.7(a) and 3.7(b) for EPAS and SbW-FFb, respectively. Consider a proportional-integral (PI) torque feedback control law because it can sufficiently attain the desired objectives of hardware impedance compensation and reference tracking, as described in Papers A and B. Consequently, the motor torque control law is given by Eq. (3.14), where the torque tracking error is defined as $e_M(t) = M_{tb,ref}(t) - M_{tb}(t)$; the controller gains are $\alpha_0 > 0$ and $\alpha_1 > 0$. The effective motor torque on the pinion is $M_{mot,eff} = i_{mot}M_{mot}$. Based on the following equation, $H_{fb,M}(s) = -(\alpha_1 + \alpha_0/s)$ defines the torque feedback control transfer function.

$$M_{mot}(t) = -(\alpha_1 e_M(t) + \alpha_0 \int_0^t e_M(\tau) d\tau) \quad (3.14)$$

3.4.1 Stability analysis

With the proportional torque feedback, the mechanical impedance (i.e., J_p , b_p , and M_{rack}) is reduced by a factor $\alpha'_1 = 1 + i_{mot}\alpha_1$ [31, 35]. Whereas, a higher integral gain (α_0) ensures a lower steady state error, e_M , and a better disturbance attenuation. Here, α_0 and α_1 should be as high as possible; however, they are typically limited due to practical reasons, such as measured signal noise, CAN-bus sampling, signal latency, controller's discrete time step, and actuator saturation. In the continuous-time domain and using the simplified Nyquist criterion (Definition 3.4.1), a necessary and sufficient uncoupled stability condition can be derived using Eq. (3.13) for the inner loop as follows; it is also illustrated in Fig. 3.8(a) for the given EPAS system.

$$\alpha_0 < \frac{1}{i_{mot}} \left[\left(\alpha'_1 + \frac{J_p}{J_s} \right)^2 \frac{k_{tb}}{J_p} + \alpha'_1 \frac{b_p}{J_p} + \frac{J_p b_s}{J_s^2} + \frac{(\alpha'_1 k_{tb} + b_p) c_p}{J_p c_{tb}} \right] \quad (3.15)$$

The assumption is $H_{ref}^{-1}(s) = 0$ and some small terms with respect to the stiff torque sensor, i.e., the torsion bar stiffness, c_{tb} , are neglected. For SbW-FFb, $c_p = 0$ Nm/rad because environment coupling does not exist. An important remark: both α_0 and α_1 can be simultaneously increased for faster reference tracking without violating Eq. (3.15).

Definition 3.4.1 (Simplified Nyquist criterion). Let $L(j\omega)$ be the loop transfer function with no poles in the closed right half-plane, except for single poles on the imaginary axis. Then, the closed-loop system is stable if and only if $L(j\omega)$, $\forall \omega \in (-\infty, \infty)$, has no net encirclement of the critical point $(-1, 0)$ in the Nyquist complex plane [132].

Non-transparent torque reference

For the next step, the torque reference model is considered to be given with $\gamma = 0$ for virtual steering feedback. Thereby, uncoupled stability is analyzed such that the system remains stable in isolation. The torque reference is defined as $H_{ref}^{-1}(s) = J_{ref}s^2 + b_{ref}s + c_{ref}$; hence, the closed-loop plant is enforced to have admittance causality. Although $H_{ref}^{-1}(s)$ is improper, assume that this for theoretical analysis. For real-time implementation, $H_{ref}^{-1}(s)$ can be made causal using a low-pass filter, which would compromise the haptic performance. Nevertheless, stability is primarily dependent on the reference stiffness, c_{ref} , because it determines the shape of the overall loop gain, i.e., $L_M(s)$ in Eq. (3.13). Assume that the inner loop is already given with a certain reference tracking cut-off frequency, ω_{in} , and the corresponding transfer function is $H_{servo}(s) = M_{tb}(s)/M_{tb,ref}(s) = \omega_{in}/(\omega_{in} + s)$. Upon simplification and further assuming $J_{ref} = 0$ kgm², $b_{ref} = 0$ Nms/rad, and $k_{tb} \approx 0$ Nms/rad, the resulting loop gain shown in Fig. 3.9(a) can be derived as follows.

$$L_M(s) = -H_{ref}^{-1}(s)H_{servo}(s)\frac{G_\theta(s)}{G_M(s)} = c_{ref} \left(\frac{\omega_{in}}{\omega_{in} + s} \right) \left(\frac{1}{J_s s^2 + b_s s} + \frac{1}{c_{tb}} \right) \quad (3.16)$$

Again, a necessary and sufficient uncoupled stability condition is derived for $L_M(j\omega)$ using Definition 3.4.1. Therefore, the quadratic inequality constraint with a non-negative

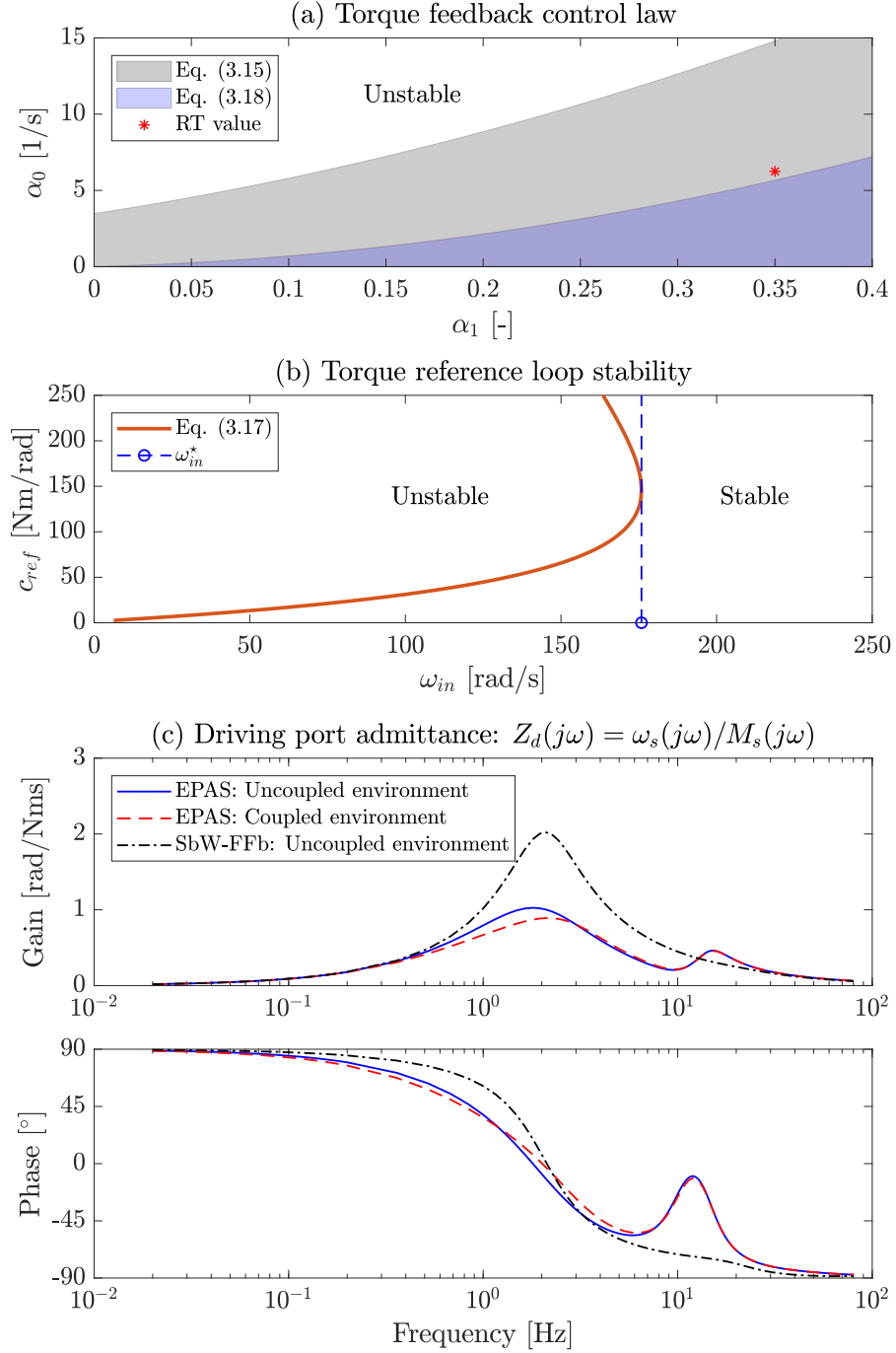


Figure 3.8: (a) EPAS torque feedback control stability regions given by Eqs. (3.15) and (3.18) between $\alpha_1 - \alpha_0$ and implemented real-time (RT) value. (b) EPAS torque reference port loop stability condition in Eq. (3.17). (c) Closed-loop (torque control) driver interaction port admittance functions for EPAS (with and without coupled environment) and SbW-FFb.

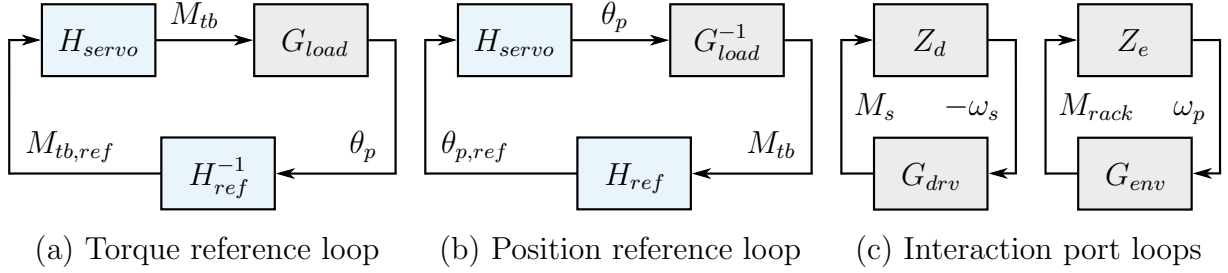


Figure 3.9: Interconnection between the uncoupled closed-loop plant and (a) torque and (b) position reference functions such that $G_{load}(s) = -G_{\theta}(s)/G_M(s)$. (c) Driving and environment port admittance functions, $Z_d(s)$ and $Z_e(s)$, coupled with their models.

c_{ref} solution in Eq. (3.17) provides an upper bound for the maximum reference stiffness. The solution depends on the inner loop tracking performance and its cut-off frequency, ω_{in} .

$$c_{ref}^2 + c_{tb} \left(2 + \frac{1}{\omega_{in}} \left(\frac{b_s}{J_s} - \frac{c_{tb}}{b_s} \right) \right) c_{ref} + c_{tb}^2 \left(1 + \frac{b_s}{\omega_{in} J_s} \right) > 0 \quad (3.17)$$

Special case: if $\omega_{in} > (c_{tb} - b_s^2/J_s)^2/(4b_sc_{tb}) = \omega_{in}^*$, then stability is mathematically ensured irrespective of $c_{ref} > 0$. This is graphically represented in Fig. 3.8(b) for the given EPAS system.

An opposite approach requires the selection of α_0 and α_1 to obtain maximum c_{ref} . Equation (3.18) ensures stability for $c_{ref} > 0$, which is derived using $L_M(s)$ from Eq. (3.13) and applying Definition 3.4.1. When compared with Eq. (3.15), it causes a higher tracking error at low frequencies due to the lower α_0 value, given a certain α_1 value in Fig. 3.8(a).

$$\alpha_0 < \alpha_1 \frac{b_p + \alpha'_1 k_{tb}}{J_p} \implies c_{ref} \in [0, \infty) \quad (3.18)$$

Definition 3.4.2 (Passivity). A linear single interaction port system defined by admittance operator $Z(s) = \omega_i(s)/M_i(s)$ is passive if and only if

1. $Z(s)$ has no right half-plane poles;
2. any pure imaginary poles of $Z(s)$ are simple with positive real residues;
3. $\text{Re}\{Z(j\omega)\} \geq 0 \forall \omega \in \mathbb{R}$.

A passive port implies that $Z(s)$ is a positive real transfer function [31, 62]. The last condition ensures the Nyquist contour of $Z(j\omega)$ to fully lie within the open right half-plane and the phase angle is in the interval $(-90^\circ, 90^\circ)$.

For the driver and environment coupled stability, the admittance functions of interaction ports listed in Table 3.2, $Z_d(s) = \omega_s(s)/M_s(s)$ and $Z_e(s) = v_{rack}(s)/F_{rack}(s) = \omega_p(s)/M_{rack}(s)$, respectively, are evaluated. The controller parameters should be chosen to achieve passive port admittance, i.e., a positive real transfer function (Definition 3.4.2). If $Z_d(s)$ and $Z_e(s)$ are passive, then port coupled stability is guaranteed for passive driver arm impedance (i.e., $G_{drv}(s)$ in Eq. (2.12)) and passive environment impedance (defined as $G_{env}(s) = M_{rack}(s)/\omega_p(s) = c_p/s$). For instance, $Z_d(s)$ is passive for different cases shown in

Fig. 3.8(c) because the phase angle lies within -90° and 90° . Hence, closed-loop stability is ensured regardless of the coupling arm stiffness, c_{arm} , and arm inertia, J_{arm} . This is because when a passive port is coupled to an arbitrary passive human or environment model, as shown in Fig. 3.9(c), coupled stability is ensured as a necessary and sufficient condition [30]. A similar deduction can be reached using the passivity theorem: the feedback connection of two passive systems is passive [62], although it is not sufficient to guarantee asymptotic stability [153]. A coupled system is asymptotically stable, if either of the two systems is *strictly* passive [31].

Transparent torque reference

This particular section is based on Paper D, where a transparent reference variable requires the \hat{M}_{rack} feedback with $\gamma > 0$. For analyzing stability under transparency, the driver model must be coupled, see Table 3.2. Subsequently, for the EPAS shown in Fig. 3.7(a), $Z_e(s) = \omega_p(s)/M_{rack}(s)$ is computed considering the following.

- (a) The driver model is ideal, thus implying fixed steering, i.e., $(\theta_s, \omega_s) = (0, 0)$.
- (b) The observer transfer function is $H_{obs}(s) = \hat{M}_{rack}(s)/M_{rack}(s) = \omega_{obs}/(\omega_{obs} + s)$.
- (c) The inner loop tracking performance is given by $M_{tb}(s)/M_{tb,ref}(s) = \omega_{in}/(\omega_{in} + s)$.
- (d) The reference torque is defined as $M_{tb,ref}(s) = b_{ref}\omega_p(s) + \gamma\hat{M}_{rack}(s)$ from Eq. (3.11). The reference stiffness, c_{ref} , is suitably assumed null for the case of pure disturbance feedback (or maximum transparency), and J_{ref} is neglected for simplicity.

$$Z_e(s) = \frac{((J_p s^2 + (b_p + k_{tb})s + c_{tb})\frac{\gamma}{1+T_{obs}s} + (c_{tb} + k_{tb}s)T_{in}s)}{(J_p s^2 + (b_p + k_{tb})s + c_{tb})((c_{tb} + k_{tb}s)(1 + T_{in}s) + b_{ref}s)} \quad (3.19)$$

Equation (3.19) is the environment port's resulting admittance function, where $T_{obs} = \omega_{obs}^{-1}$ and $T_{in} = \omega_{in}^{-1}$. Definition 3.4.2 can be applied to this expression for deriving the stability condition.

The inequality expression in Eq. (3.20) is the transparency gain upper bound, $\bar{\gamma}$, which is derived for passive $Z_e(s)$. Thus, it ensures that the closed-loop system shown in Fig. 3.9(c) remains stable regardless of the environment dynamics, i.e., $c_p \in [0, \infty)$, if $G_{env}(s) = c_p/s$.

$$\gamma < \frac{1}{\omega_{obs}J_p} \left[b_{ref} + k_{tb} \left(1 + \frac{b_p + k_{tb}}{\omega_{in}J_p} \right) \right] = \bar{\gamma} \quad (3.20)$$

The above result is quite conservative since it is derived using passivity; therefore, the haptic performance could deteriorate by consistently adhering to the equation. To achieve higher limiting transparency for a given system, observer, and controller, higher reference damping is required. This would occur at the cost of damped (high frequency) steering feedback transparency. However, if Eq. (3.20) is not satisfied, then there exists an upper bound for c_p , rendering the closed-loop unstable. If and only if $\gamma \in [0, \bar{\gamma})$, then $Z_e(j\omega)$ and its loop transfer function, $Z_e(j\omega)G_{env}(j\omega)$, do not cross the negative real axis irrespective of c_p .

A similar procedure can be applied to the torque–position SbW control architecture in Fig. 3.7(b) to compute $Z_e(s) = \omega_{p2}(s)/M_{rack}(s)$ with the following considerations.

- (a) The driver model is ideal, i.e., $(\theta_s, \omega_s) = (0, 0)$.
- (b) The observer transfer function is $H_{obs}(s) = \hat{M}_{rack}(s)/M_{rack}(s) = \omega_{obs}/(\omega_{obs} + s)$.
- (c) The FFb tracking performance is given by $M_{tb}(s)/M_{tb,ref}(s) = \omega_{in1}/(\omega_{in1} + s)$.
- (d) The reference torque is given by $M_{tb,ref}(s) = b_{ref}\omega_{p1}(s) + \gamma\hat{M}_{rack}(s)$ from Eq. (3.11). Again, c_{ref} is assumed null for maximum transparency, and J_{ref} is neglected.
- (e) For the SbW-rack (or RWA) position control: $y_{ref}^{rack}(t) = \theta_{p1}$, $y^{rack}(t) = \theta_{p2}$, and the position tracking performance is given by $\theta_{p2}(s)/\theta_{p1}(s) = \omega_{in2}/(\omega_{in2} + s)$.

$$Z_e(s) = \frac{((J_{p2}s + b_{p2})\frac{\gamma}{1+T_{obs}s} + T_{in2}(b_{ref}s + c_{tb}(1 + T_{in1}s)))s}{(1 + T_{in2}s)(J_{p2}s + b_{p2})(b_{ref}s + c_{tb}(1 + T_{in1}s))} \quad (3.21)$$

The corresponding environment port's admittance function is given by Eq. (3.21), where $T_{obs} = \omega_{obs}^{-1}$, $T_{in1} = \omega_{in1}^{-1}$, and $T_{in2} = \omega_{in2}^{-1}$. Applying Definition 3.4.2 for a similar stability condition as that in EPAS, the resulting expression is as follows.

$$\gamma < \frac{1}{\omega_{obs}J_{p2}} \left(1 + \frac{b_{p2}}{\omega_{in2}J_{p2}} \right) \left(b_{ref} + \frac{c_{tb}}{\omega_{in1}} \right) = \bar{\gamma} \quad (3.22)$$

Equations (3.20) and (3.22) are important to ensure stability during transparent steering feedback in (torque controlled) EPAS and SbW-FFb, respectively. Although they are derived here for convenience, their relevance is presented in the next chapter.

3.4.2 Tracking performance and robustness

The inner loop's (non-transparent) reference tracking performance can be evaluated by applying frequency response excitation to the $M_{tb,ref}$ channel. For both EPAS and SbW-FFb, the measurements from real hardware are used to plot the FRF of $M_{tb}(j\omega)/M_{tb,ref}(j\omega)$ shown in Fig. 3.10(a). A reasonable tracking response is obtained using a simple but methodologically tuned PI controller with a feedback linearization request. Nevertheless, the phase response of EPAS primarily caused by the motor torque request signal latency can still be improved. The controller bandwidths or cut-off frequencies (ω_c) of EPAS and SbW-FFb are 108.20 rad/s and 124.09 rad/s, respectively.

For ensuring contact stability and robustness, two parametric uncertainties in the haptic controller exist at the interaction port: coupling stiffness and inertia. Accordingly, the effects of coupling pinion stiffness (at the environment port) and coupling arm inertia (at the driver port) are investigated. The influence of coupling arm stiffness can be implicitly understood from the driver interaction port's admittance function, as shown in Fig. 3.8(c), and it is also described earlier. The effect of coupling inertia at the environment port is disregarded due to its unrealistic possibility for the given systems.

Figure 3.10(b) illustrates the percentage change in the EPAS controller bandwidth with increasing coupling pinion stiffness, c_p , where the nominal (uncoupled) bandwidth is given by ω_{c0} without any uncertainty. The torque control method appears robust within the defined c_p interval. Similarly, robustness against the coupled driver arm inertia, J_{arm} , can be analyzed from Fig. 3.10(c). For both systems, the controller bandwidths decrease marginally. Hence, the torque control approach can be adjudged as reasonably robust against port uncertainties.

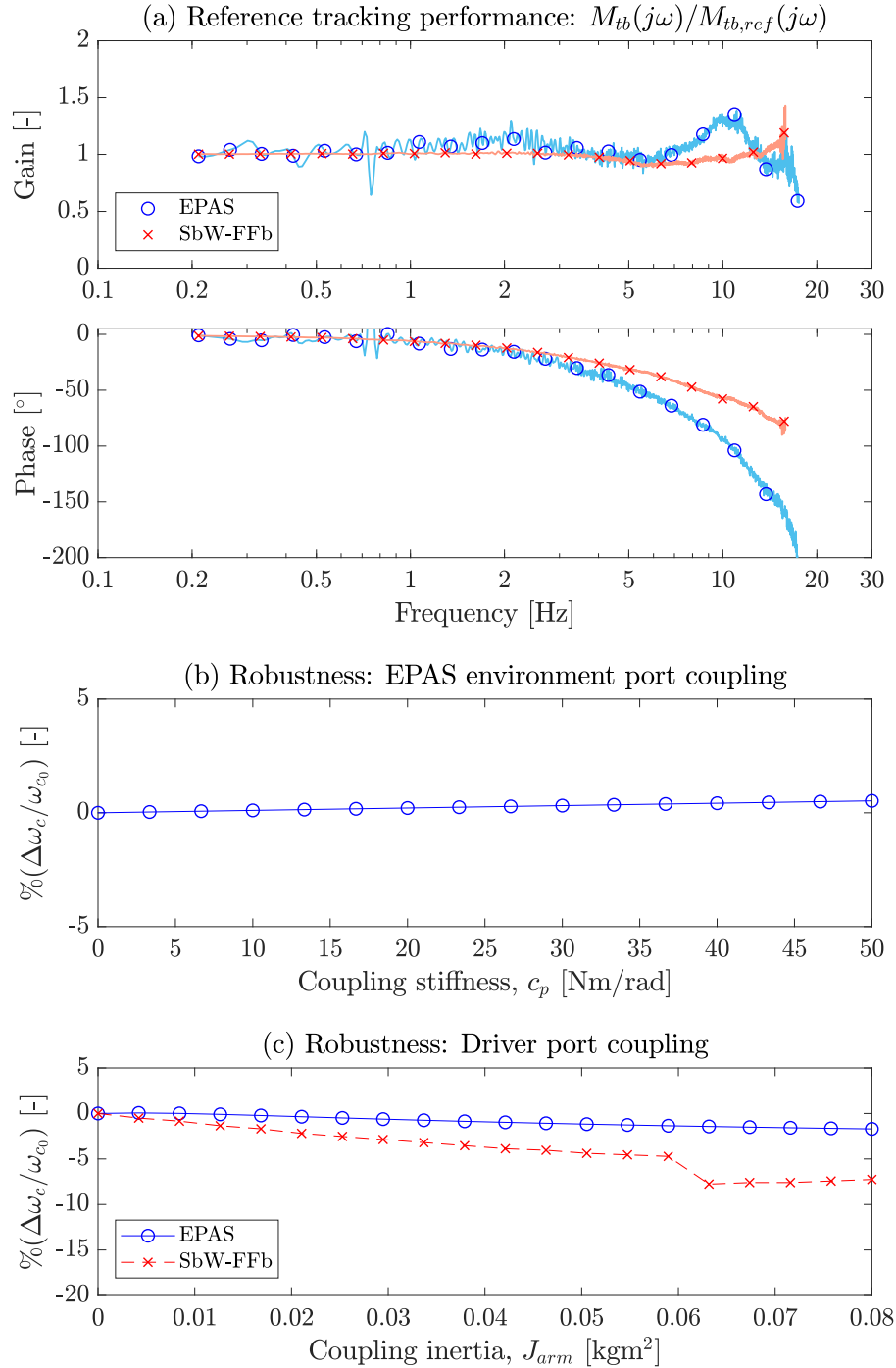


Figure 3.10: (a) The torque feedback controller's reference tracking performance illustrated in the FRF plot. (b) The robustness plot for EPAS exhibits the percentage change in the nominal controller bandwidth with increasing coupling pinion stiffness at the environment interaction port. (c) The robustness plot for EPAS and SbW-FFb exhibits the percentage change in the nominal controller bandwidth with increasing coupled arm inertia at the driver interaction port.

3.5 Position control

For the architectures in Fig. 3.7, the position control setting requires the following: $y_2(t) = \theta_p$, $y_1(t) = M_{tb}$, and $y_{2,ref}(t) = \theta_{p,ref}$ for EPAS and SbW-FFb, respectively. A sufficient position control law is derived using the previously defined torque controller because of the inverted causality. Thereby, the two non-transparent loop gains from Eq. (3.13) are equated to obtain the position feedback control transfer function $H_{fb,\theta}(s)$ in Eq. (3.23). This theoretically ensures a comparable result, given $G_\theta(s) - H_{ref}(s)G_M(s) \neq 0$. Note that Eq. (3.23) is deduced using $H_{fb,M}(s) = -(\alpha_1 + \alpha_0/s)$ and $H_{ref}^{-1}(s) = (J_{ref}s^2 + b_{ref}s + c_{ref})$ from Eq. (3.11).

$$L_M(s) = L_\theta(s) \iff H_{fb,\theta}(s) = -H_{fb,M}(s)H_{ref}^{-1}(s) = \beta_3 s^2 + \beta_2 s + \beta_1 + \beta_0/s \quad (3.23)$$

From the above expression, the inner loop is construed to minimize the tracking error in the motion trajectory variables, i.e., angular position, velocity, and acceleration. Consequently, Eq. (3.24) defines the motor torque, where $e_\theta(t) = \theta_{p,ref}(t) - \theta_p(t)$ is the position tracking error; the controller gains are $\beta_0 > 0$, $\beta_1 > 0$, $\beta_2 > 0$, and β_3 . Each gain fulfills a specific purpose: β_3 , β_2 , and β_1 manipulate the system inertia, damping, and stiffness, respectively; β_0 ensures reference tracking and disturbance attenuation (Papers A and B).

$$M_{mot}(t) = \beta_3 \ddot{e}_\theta(t) + \beta_2 \dot{e}_\theta(t) + \beta_1 e_\theta(t) + \beta_0 \int_0^t e_\theta(\tau) d\tau \quad (3.24)$$

3.5.1 Stability analysis

In general, the essential aspects for position control stability require to compensate the system inertia and increase damping. The former can typically be achieved directly by assuming $\dot{\omega}_{p,ref} = 0$ rad/s² and $\beta_3 < 0$, similar to open loop control. As a result, the feedback control law in Eq. (3.24) becomes a non-minimum phase. However, a different approach is adopted by implementing a minimum phase control law, given $\dot{\omega}_{p,ref}$ and $\beta_3 > 0$, because the aim is to follow the reference trajectory variables ($\theta_{p,ref}$, $\omega_{p,ref}$, and $\dot{\omega}_{p,ref}$) while ensuring stability and reasonable reference tracking. A causal $H_{fb,\theta}(s)$ is required for real-time execution unless all required error states are known. Therefore, the same low-pass filter as that in $H_{ref}^{-1}(s)$ is implemented for fair comparison.

$$\beta_0 < \frac{1}{i_{mot}} \left(\frac{b_s + b_p + \beta_2 i_{mot}}{J_s + J_p + \beta_3 i_{mot}} \right) (c_p + \beta_1 i_{mot}) \quad (3.25)$$

Equation (3.25) is a necessary and sufficient uncoupled stability condition for the inner loop. It is derived using Definition 3.4.1 and Eq. (3.13), assuming that $H_{ref}(s) = 0$ and an infinitely stiff torque sensor (i.e., $c_{tb} \rightarrow \infty$ and $k_{tb} = 0$ Nms/rad) exists. Again, $c_p = 0$ Nm/rad for SbW-FFb. A graphical representation of the aforementioned inequality between β_3 - β_0 is shown in Fig. 3.11(a) for the given EPAS system. A higher β_0 value ensures a lower tracking error, e_θ , at low frequencies; whereas a higher β_3 value ensures a reduced error and a more damped response at high frequencies. In Fig. 3.11(a), β_1 and β_2 are selected beforehand to achieve a desired tracking performance, as described in Papers A and B. An important remark: due to a hyperbolic relationship, β_3 and β_0 cannot be increased simultaneously.

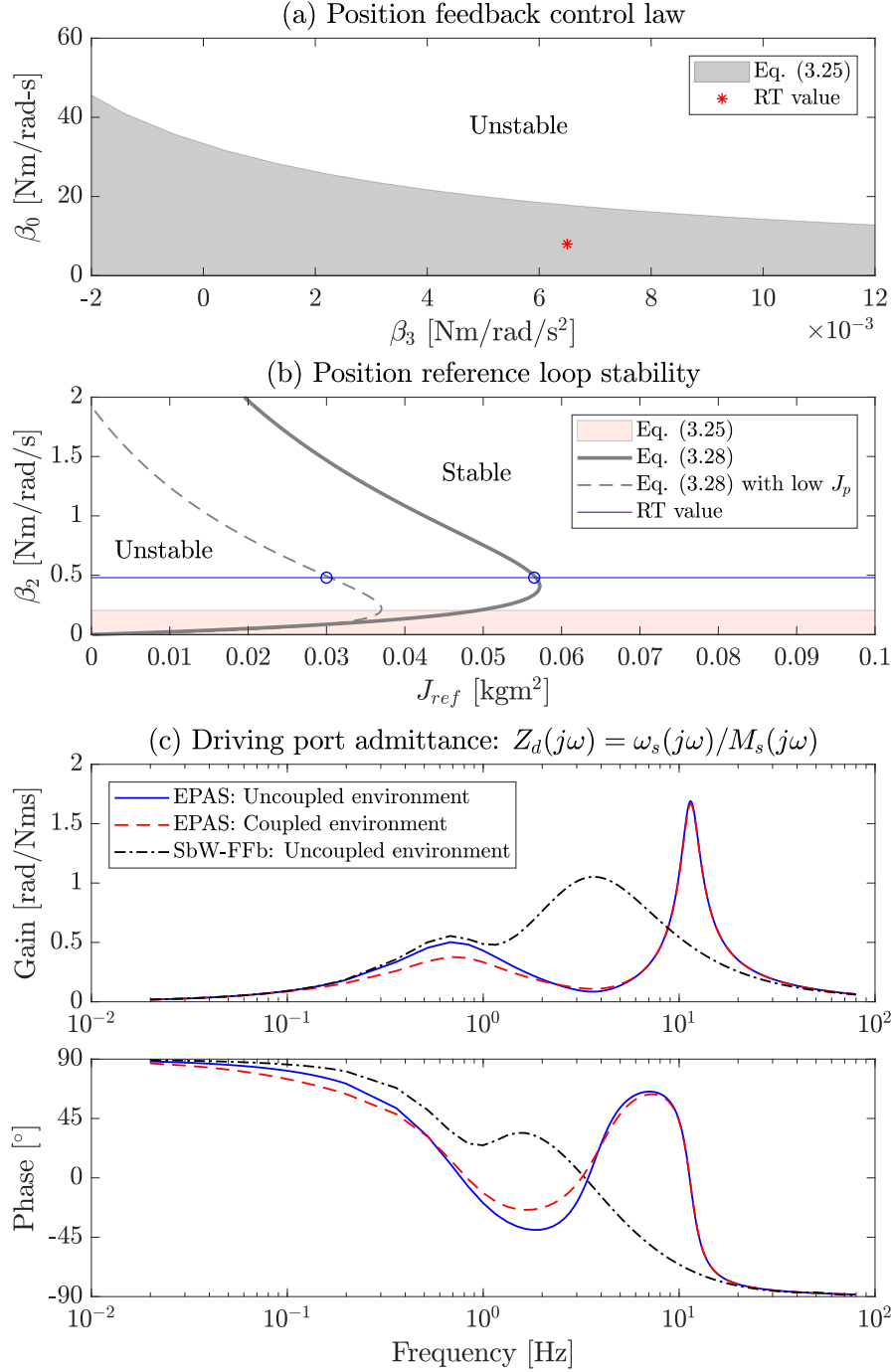


Figure 3.11: (a) EPAS position feedback control stability region given by Eq. (3.25) between $\beta_3 - \beta_0$ and implemented real-time (RT) value. (b) EPAS position reference loop stability condition in Eq. (3.28). (c) The closed-loop (position control) driver interaction port admittance functions for EPAS (with and without coupled environment) and SbW-FFb.

Non-transparent position reference

With a virtual admittance function in the outer loop, i.e., $H_{ref}(s) = (J_{ref}s^2 + b_{ref}s + c_{ref})^{-1}$ and $\gamma = 0$, the closed-loop plant is constrained to have impedance causality. The first uncoupled stability condition is derived by assuming that the inner loop is already known with a certain tracking performance and defined by $H_{servo}(s) = \omega_{in}/(\omega_{in} + s)$, see Fig. 3.9(b), where ω_{in} is the position controller's cut-off frequency. As stated, $L_\theta(s)$ in Eq. (3.13) determines the closed-loop stability, which primarily depends on the reference inertia (J_{ref}) because a smaller J_{ref} value implies a larger $L_\theta(s)$. Therefore, the assumption that $b_{ref} = 0$ Nms/rad and $c_{ref} = 0$ Nm/rad is sufficient. Hence, the resulting loop gain is as follows.

$$L_\theta(s) = -H_{ref}(s)H_{servo}(s)\frac{G_M(s)}{G_\theta(s)} = \frac{1}{J_{ref}s^2} \left(\frac{\omega_{in}}{\omega_{in} + s} \right) \left(\frac{(J_s s^2 + b_s s)(c_{tb} + k_{tb}s)}{J_s s^2 + (b_s + k_{tb})s + c_{tb}} \right) \quad (3.26)$$

Applying Definition 3.4.1 to $L_\theta(j\omega)$ for a necessary and sufficient uncoupled stability condition, a lower bound inequality constraint is derived for J_{ref} in Eq. (3.27). It signifies the extent to which a lower J_{ref} value can be realized in the outer loop admittance function without causing instability, given a certain inner loop tracking performance. Mathematically, the smaller the reference inertia, the faster the admittance reference dynamics for human interaction. As ω_{in} increases, implying a faster reference tracking, the lower bound on J_{ref} in Eq. (3.27) decreases. In hindsight, achieving a lower J_{ref} value with a higher coupled driver arm inertia and a lower ω_{in} is difficult; it is the main reason behind contact instability.

$$J_{ref} > \frac{J_s}{b_s + k_{tb}} \left(\frac{-J_s k_{tb} \omega_{in}^2 + (J_s c_{tb} - k_{tb}^2) \omega_{in}}{J_s \omega_{in}^2 + (b_s + k_{tb}) \omega_{in} + c_{tb}} \right) \quad (3.27)$$

In another possibility where a certain J_{ref} is required, the inner loop should be designed by manipulating the (high frequency) loop gain using β_2 . Here, the other parameters (c_{ref} , b_{ref} , b_s , b_p , β_0 , β_1 , and β_3) are neglected due to their minimal influence on the stability condition. According to [22], if the torque sensor is assumed to be infinitely stiff, then sufficient stability condition $J_{ref} \geq J_p$ can be derived based on the small gain theorem. However, with limited compliance, realizing $J_{ref} < J_p$ with a higher β_2 value as given by Eq. (3.28) is possible, as illustrated in Fig. 3.11(b) for the given EPAS system. This quadratic constraint is also derived by applying Definition 3.4.1 to $L_\theta(s)$ from Eq. (3.13).

$$\beta_2^2 + \left[\left(\frac{1 - \frac{J_p}{J_{ref}}}{\frac{1}{J_s} + \frac{1}{J_{ref}}} \right) \frac{c_{tb}}{k_{tb}} + k_{tb} \left(1 + \frac{J_p}{J_s} \right) \right] \beta_2 + \frac{c_{tb} \left(\frac{J_p}{J_s} + 1 \right)^2}{\frac{1}{J_s} + \frac{1}{J_{ref}}} > 0 \quad (3.28)$$

If β_0 , β_1 , and β_3 are not neglected, then there exists a lower bound condition on β_2 , as defined by Eq. (3.25), for the inner loop stability; the corresponding unstable region is also highlighted in Fig. 3.11(b). This figure also exhibits a special case: for a given β_2 value and a system with low pinion inertia (i.e., either J_p is reduced or compensated using β_3) a smaller J_{ref} value can be realized for faster reference admittance dynamics with ensured uncoupled stability.

Coupled stability is evaluated using Definition 3.4.2, as explained in torque control. For the driver interaction port, the frequency response of $Z_d(s) = \omega_s(s)/M_s(s)$ can be observed

in Fig. 3.11(c) for different cases and a given controller tuning. Because the phase response is bounded within -90° and 90° , $Z_d(s)$ is passive (or a positive real function). Hence, the driver coupled/contact stability is ensured with $G_{drv}(s)$ from Eq. (2.12), as shown in Fig. 3.9(c), irrespective of the arm impedance parameters: c_{arm} and J_{arm} . The environment coupled stability is discussed under the robustness topic.

Transparent position reference

The discussion on coupled stability under transparency, where the position reference variable is a function of \hat{M}_{rack} and $\gamma > 0$, and is based on Paper D. First, the environment port's admittance function, $Z_e(s) = \omega_p(s)/M_{rack}(s)$, is computed for EPAS according to the position control architecture in Fig. 3.7(a) considering the following.

- (a) The driver model condition is ideal, i.e., $(\theta_s, \omega_s) = (0, 0)$ in Table 3.2.
- (b) The observer transfer function is $H_{obs}(s) = \hat{M}_{rack}(s)/M_{rack}(s) = \omega_{obs}/(\omega_{obs} + s)$.
- (c) The inner loop tracking performance is given by $\theta_p(s)/\theta_{p,ref}(s) = \omega_{in}/(\omega_{in} + s)$.
- (d) Using Eq. (3.12), the reference velocity becomes $\omega_{p,ref}(s) = (M_{tb}(s) - \gamma\hat{M}_{rack}(s))/b_{ref}$. The reference stiffness, c_{ref} , is assumed null for maximum transparency and the reference inertia, J_{ref} , is neglected for simplicity.

As a result, Eq. (3.29) defines the environment port's admittance function, as follows:

$$Z_e(s) = \frac{((J_p s^2 + (b_p + k_{tb})s + c_{tb})\frac{\gamma}{1+T_{obs}s} + b_{ref}T_{in}s^2)s}{(J_p s^2 + (b_p + k_{tb})s + c_{tb})(c_{tb} + k_{tb}s + (1 + T_{in}s)b_{ref}s)} \quad (3.29)$$

where $T_{obs} = \omega_{obs}^{-1}$ and $T_{in} = \omega_{in}^{-1}$. With the foregoing, Definition 3.4.2 can be applied to derive a necessary and sufficient stability condition similar to that of torque control. Equation (3.30) is the inequality constraint for the transparency gain upper bound, $\bar{\gamma}$, for passive $Z_e(s)$.

$$\gamma < \frac{1}{\omega_{obs}J_p} \left[b_{ref} \left(1 + \frac{b_p + k_{tb}}{\omega_{in}J_p} \right) + k_{tb} \right] = \bar{\gamma} \quad (3.30)$$

Thus, adhering to the above condition ensures coupled stability under transparency, regardless of the coupling environment stiffness c_p , given $G_{env}(s) = c_p/s$, as shown in Fig. 3.9(c). A remark: the steering feedback transparency gain upper bound can be increased by realizing a higher reference damping value, b_{ref} , given a certain system, observer and controller. This expression is analogous to the EPAS torque control result in Eq. (3.20).

For the position–position SbW control architecture shown in Fig. 3.7(b), similar steps are followed to obtain $Z_e(s) = \omega_{p2}(s)/M_{rack}(s)$ with the following considerations.

- (a) The driver model condition is ideal, i.e., $(\theta_s, \omega_s) = (0, 0)$.
- (b) The observer transfer function is $H_{obs}(s) = \hat{M}_{rack}(s)/M_{rack}(s) = \omega_{obs}/(\omega_{obs} + s)$.
- (c) The FFb tracking performance is given by $\theta_{p1}(s)/\theta_{p1,ref}(s) = \omega_{in1}/(\omega_{in1} + s)$.
- (d) The reference velocity is defined as $\omega_{p1,ref}(s) = (M_{tb}(s) - \gamma\hat{M}_{rack}(s))/b_{ref}$ using Eq. (3.12) with a null c_{ref} for maximum transparency and neglecting J_{ref} .

(e) For the SbW-rack (or RWA) position control: $y_{ref}^{rack}(t) = \theta_{p1}$, $y^{rack}(t) = \theta_{p2}$, and the position tracking performance is given by $\theta_{p2}(s)/\theta_{p1}(s) = \omega_{in2}/(\omega_{in2} + s)$. The corresponding environment port's admittance function is given by

$$Z_e(s) = \frac{((J_{p2}s + b_{p2})\frac{\gamma}{1+T_{obs}s} + T_{in2}(b_{ref}s(1 + T_{in1}s) + c_{tb}))s}{(1 + T_{in2}s)(J_{p2}s + b_{p2})(b_{ref}s(1 + T_{in1}s) + c_{tb})}. \quad (3.31)$$

where $T_{obs} = \omega_{obs}^{-1}$, $T_{in1} = \omega_{in1}^{-1}$, and $T_{in2} = \omega_{in2}^{-1}$. Compared with previous similar results, an interesting conclusion is as follows: $b_{ref} > 0$ is the only necessary and sufficient condition to achieve passive $Z_e(s)$ in Eq. (3.31), which is derived using Definition 3.4.2. This implies that the position–position SbW control architecture is stable under transparency due to its defined causality, given $b_{ref} \neq 0$. However, the steering feedback performance in reality depends significantly on presumably known parameters (ω_{in1} , ω_{in2} , and other neglected aspects, such as time delay).

3.5.2 Typical shortcomings

In the non-transparent setting, the tracking performance of the inner loop can be evaluated using the reference pinion angle excitation. Subsequently, a frequency response plot based on real-time experiments is obtained, as shown in Fig. 3.12(a) for EPAS ($\theta_p(s)/\theta_{p,ref}(s)$), SbW-FFb ($\theta_{p1}(s)/\theta_{p1,ref}(s)$), and SbW-rack ($\theta_{p2}(s)/\theta_{p2,ref}(s)$). The implemented LTI controllers consist of four gains, namely β_0 , β_1 , β_2 , and β_3 , for different error states e_θ , \dot{e}_θ , and \ddot{e}_θ . Explicit feedback linearization should be performed to compensate for the system's Coulomb friction (Paper E) to attain a small position tracking error, e_θ , at low frequencies regardless of controller tuning. Finally, the controller cut-off frequencies are estimated from the corresponding FRF shown in Fig. 3.12(a); they are 39.92 rad/s (EPAS), 70.69 rad/s (SbW-FFb), and 61.26 rad/s (SbW-rack). The SbW-rack position controller is more than sufficient to achieve the desired vehicle lateral motion performance, which is implicitly stated in the literature as a requirement [154–159]; therefore, it is not discussed any further. However, the position controller in EPAS and SbW-FFb requires improvement, especially for the latter, in terms of reference tracking (compared with torque control) and a lower overshoot (or a more damped) response. This is the major drawback of position control.

The closed-loop sensitivity is the next point for discussion. For contact stability and robustness, uncertainties due to coupling pinion stiffness (at the environment port) and coupled arm inertia (at the driver port) are investigated. The percentage change in the EPAS controller bandwidth (defined by ω_c) with increasing coupling stiffness, c_p , at the environment port is shown in Fig. 3.12(b). This percentage change is with respect to the nominal value, given by ω_{c0} (i.e., without any port uncertainty). From the same plot, it can be claimed that the closed-loop system is robust against coupling stiffness variations.

Although the closed-loop driver port admittance remains stable regardless of c_{arm} and J_{arm} , as has been shown using the $Z_d(s)$ passivity in Fig. 3.11(c), the influence of J_{arm} causes significant loss in the position tracking performance (Fig. 3.12(c)). For both EPAS and SbW-FFb, their respective controller bandwidths significantly decreased with increasing J_{arm} . Hence, this approach is considerably less robust against the coupled arm inertia uncertainty at the driver interaction port. This leads to the next question: how can the robustness of a typical single-variable position controller be improved?

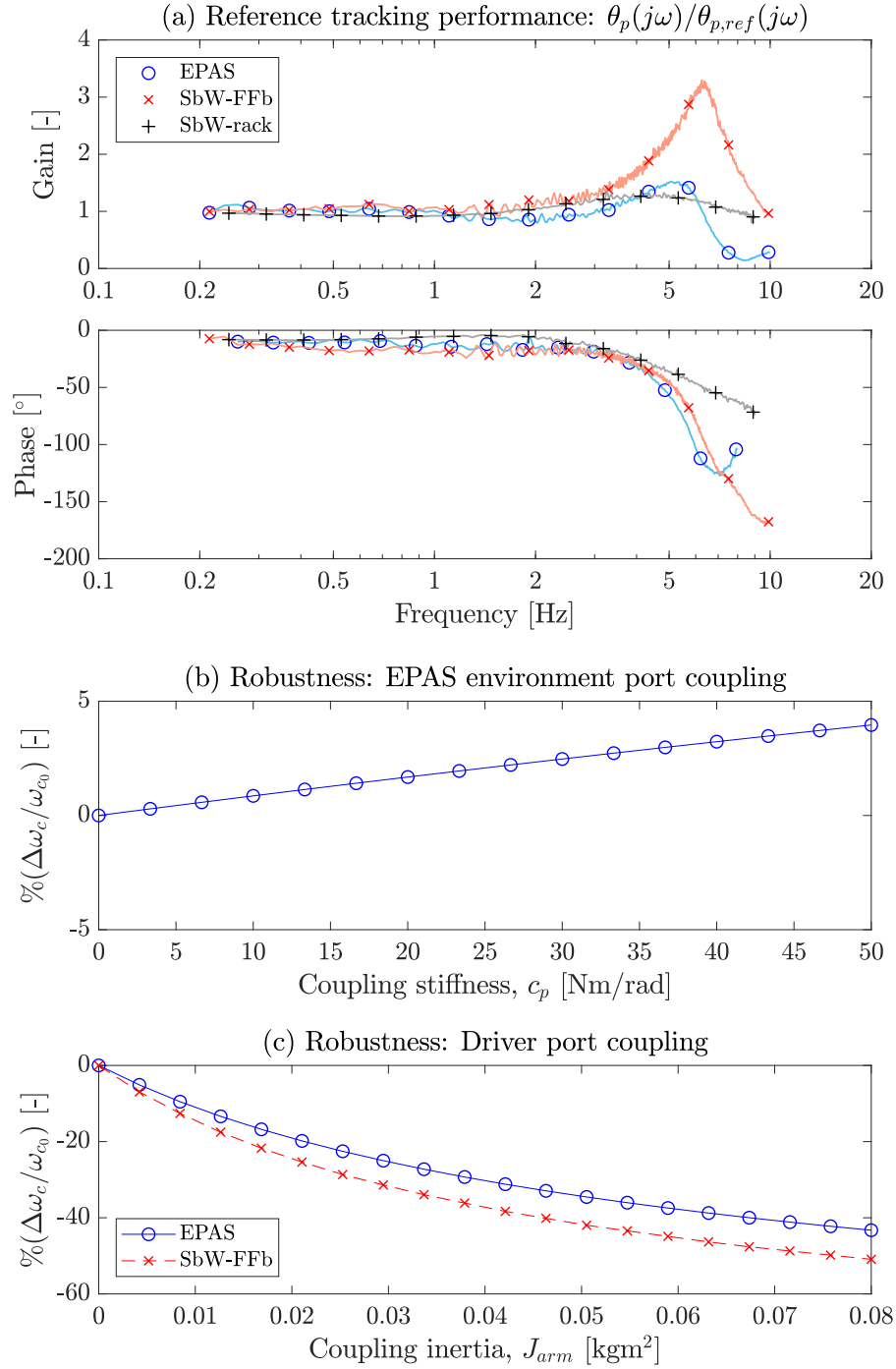


Figure 3.12: (a) The position feedback controller's reference tracking performance illustrated in the FRF plot. (b) The robustness plot for EPAS exhibits the percentage change in the nominal controller bandwidth with increasing coupling pinion stiffness at the environment interaction port. (c) The robustness plot for EPAS and SbW-FFb exhibits the percentage change in the nominal controller bandwidth with increasing coupled arm inertia at the driver interaction port.

3.5.3 A more robust solution: \mathcal{H}_∞ control

This section and brief overview are entirely based on Paper E. A typical position control law relies on the principle of a single-variable, as given in Eq. (3.24), where the position error and its subsequent states are minimized. A better solution is proposed in Paper E based on the multi-variable approach. The concept involves the minimization of typical position error with the sensed torsion bar torque signal in the position feedback controller; the ultimate aim is to improve tracking and robustness.

In the same paper, a systematic approach to develop a robust \mathcal{H}_∞ position controller is shown. First, the control law in Eq. (3.24) is directly modified by including a static torque feedback with the proportional gain, α'_1 . As a result, the multi-variable position control law becomes as follows.

$$M_{mot}(t) = \beta_3 \ddot{e}_\theta(t) + \beta_2 \dot{e}_\theta(t) + \beta_1 e_\theta(t) + \beta_0 \int_0^t e_\theta(\tau) d\tau + \alpha'_1 M_{tb}(t) \quad (3.32)$$

The analysis of the influence of α'_1 on reference tracking and robustness is extensively presented in Paper E. Based on those propositions, the following are summarized:

- (a) Negative torque feedback, i.e., $\alpha'_1 < 0$, improves the position tracking performance without affecting robustness to a certain extent.
- (b) With $\alpha'_1 < 0$, mitigating an existing overshoot is insufficient because it decreases the reference tracking FRF damping ratio that further increases the overshoot.
- (c) Higher order torque feedback is necessary for better robustness.
- (d) Small inner loop gain at high frequencies should be achieved because it implies the possibility of realizing a lower J_{ref} value in the outer loop for faster haptic performance based on the small gain arguments.

The above findings are taken into consideration to seek for an optimal torque feedback response instead of a static gain, α'_1 , in the position controller. The corresponding weighting functions and exogenous input–output (w – z) formulation are presented in Paper E. Hence, an \mathcal{H}_∞ controller, which is solvable by the linear matrix inequality (LMI) methods is proposed. A general framework for its computation is adopted from [134, pp. 357–372], where the transfer functions of plant $P(s)$ and controller $K(s)$ are represented with the following state-space:

$$P := \left[\begin{array}{c|cc} A & B_1 & B_2 \\ \hline C_1 & D_{11} & D_{12} \\ C_2 & D_{21} & 0 \end{array} \right] \text{ and } K := \left[\begin{array}{c|c} A_k & B_k \\ \hline C_k & D_k \end{array} \right]. \quad (3.33)$$

The closed-loop transfer function from input w to output z is given by the linear fractional transformation $F_l(P, K)$. By minimizing $F_l(P, K)$ with the \mathcal{H}_∞ system norm criteria⁴, the optimization problem is solved for the objective $\|z(t)\|_2^2 - \gamma^2 \|w(t)\|_2^2$, as follows:

$$\min_K \|F_l(P, K)\|_\infty = \min_K \max_{w(t) \neq 0} \frac{\|z(t)\|_2}{\|w(t)\|_2} < \gamma \quad (3.34)$$

⁴The \mathcal{H}_∞ norm is defined as the maximum singular value of $F_l(P, K)$ in the frequency domain.

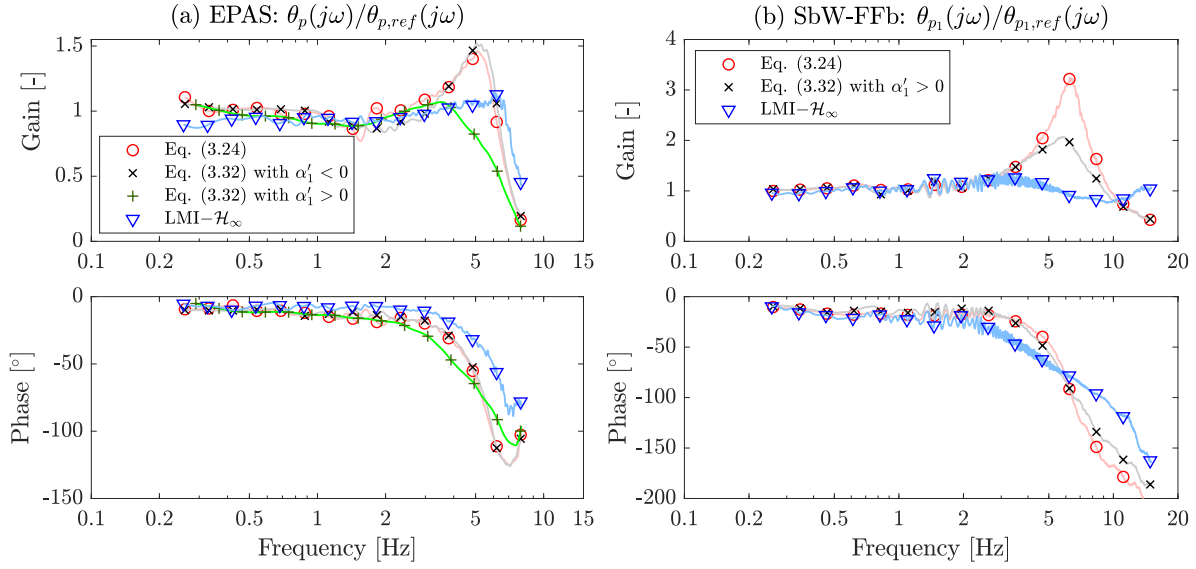


Figure 3.13: (Figure from Paper E) Measured position tracking $\theta_p(s)/\theta_{p,ref}(s)$ FRF plot from real-time implementation in (a) EPAS and (b) SbW-FFb with different control laws; Eq. (3.24) for a single-variable, Eq. (3.32) for static gain multi-variable, and \mathcal{H}_∞ solution from Eq. (3.35).

such that the peak bounded by $\gamma > 0$ is minimized. Let X be the Lyapunov solution of the bounded real lemma shown below. Subsequently, K is implicitly reconstructed using the algorithm presented in [160]:

$$\begin{aligned} & \min \gamma \\ & \text{s.t.} \quad \begin{bmatrix} A_{cl}^T X + X A_{cl} & X B_{cl} & C_{cl}^T & 0 \\ B_{cl}^T X & -\gamma I & D_{cl}^T & 0 \\ C_{cl} & D_{cl} & -\gamma I & 0 \\ 0 & 0 & 0 & -X \end{bmatrix} \prec 0 \end{aligned} \quad (3.35)$$

where

$$\begin{aligned} A_{cl} &= \begin{bmatrix} A + B_2 D_k C_2 & B_2 C_k \\ B_k C_2 & A_k \end{bmatrix} \\ B_{cl} &= \begin{bmatrix} B_1 + B_2 D_k D_{21} \\ B_k D_{21} \end{bmatrix} \\ C_{cl} &= \begin{bmatrix} C_1 + D_{12} D_k C_2 & D_{12} C_k \end{bmatrix} \quad \text{and} \\ D_{cl} &= \begin{bmatrix} D_{11} + D_{12} D_k D_{21} \end{bmatrix}. \end{aligned}$$

The controller is synthesized using MATLAB Robust Control Toolbox. Before final implementation, some important aspects of the proposed solution are as follows.

- (a) The \mathcal{H}_∞ loop shaping procedure is applied to explicitly include an integral state of e_θ to achieve better disturbance attenuation and lower steady state tracking error. Consequently, the controller inputs are $e_\theta(t)$, $\dot{e}_\theta(t)$, and $M_{tb}(t)$.

3.6. Summary

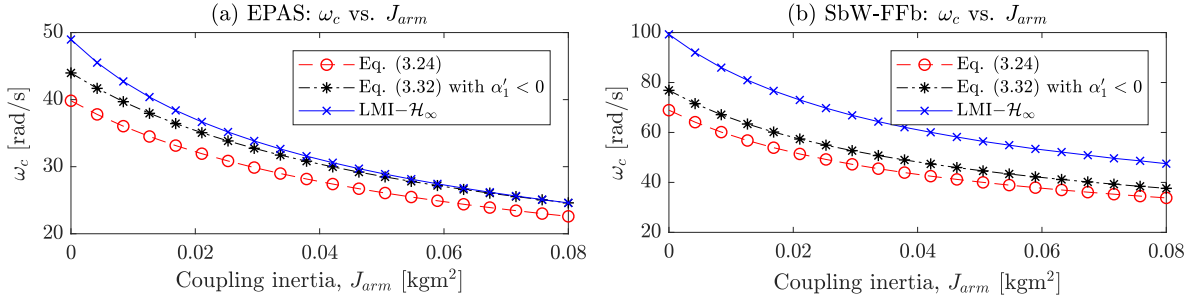


Figure 3.14: (Figure from Paper E) Reference tracking cut-off frequency, ω_c , over J_{arm} uncertainty in (a) EPAS and (b) SbW-FFb for different position controllers. The control laws are given by Eq. (3.24) for a single-variable, Eq. (3.32) for static gain multi-variable, and \mathcal{H}_∞ solution from Eq. (3.35).

- (b) For real-time digital execution, the explicit Euler solver was used, and the controller's eigenvalues were constrained within the circular disc, $\mathcal{D} := |1 + h\lambda_i| \leq 1, \forall \lambda_i \in \mathbb{C}$, using the LMI technique, where λ_i represents the eigenvalues, and h is the solver time.
- (c) A robustly stable closed-loop plant is obtained with the derived \mathcal{H}_∞ controller regardless of the coupled arm inertia because the dominant closed-loop eigenvalues converge toward the origin as $J_{arm} \rightarrow \infty$.

Figure 3.13 clearly illustrates the difference in the position reference tracking performance with different control laws. As mentioned, negative static torque feedback gain can improve the tracking performance at the cost of a higher overshoot response. In contrast, a positive torque feedback gain ensures greater damping but with a lower reference tracking cut-off frequency. However, both tracking cut-off frequency and overshoot response improve using an \mathcal{H}_∞ controller in EPAS and SbW-FFb; the cut-off frequency values are 48.69 rad/s and 94.25 rad/s, respectively. The improvement in robustness, as a function of the coupled arm inertia, can implicitly be observed in Fig. 3.14, where the reference tracking cut-off frequency varies with J_{arm} for different controllers. As anticipated, the \mathcal{H}_∞ controller is more robust. Hence, the proposed solution compared with that of a typical position controller offers improvement in performance and robustness.

3.6 Summary

In this chapter, different steering feedback control strategies for EPAS and SbW-FFb are discussed in the context of driver–steering–vehicle interaction. A typical open loop control and its shortcomings are first introduced and then closed-loop methods (torque and position control) are proposed. The linear control design aspects, i.e., stability, performance, robustness, and transparency are considered to answer the first research question (Section 1.2). The model and controller parameters are found in Appendix B.

A final remark is as follows: the torque control method compared with position control exhibits better reference tracking and robustness against coupling uncertainties. Accordingly,

an \mathcal{H}_∞ position controller is proposed to mitigate the adversity to a certain extent; however, its robustness continues to be insufficient with increasing coupling inertia.

4 Steering feedback reference

This chapter deals with the control architecture problem of the reference model for achieving the desired steering feedback. It begins with a general discussion of the reference model presented in Section 4.1, followed by a detailed description for both torque and position control causalities. First, the computation of the reference trajectory for a non-transparent control setting is elaborated (Section 4.2). This is partially based on the results from Paper C; the proposed solution depends on the virtual environment model.

For the steering feedback transparency, an estimate of the tire–road interaction at the environment port is required. Consequently, two disturbance observer algorithms presented in Section 4.3 and Paper D are compared. In the next step, the best available estimated disturbance signal is realized in the reference trajectory to achieve transparency, as described in Section 4.4. Lastly, an algorithm is formulated for optimal driver–environment transparency as a function of vehicle motion states and based on the model predictive control (MPC) framework. The concept is introduced in Section 4.5.

4.1 Model structure

The reference model shown in Fig. 3.7 is responsible for the reference trajectory. For a relevant HMI, different sources of excitation should be considered to compute the reference trajectory. These excitation sources are: driver, environment and interventions from active safety functions. The control structure of the reference model, which is valid for both EPAS and SbW systems, is discussed in this section.

The discussion begins with the driver excitation source and its implication. As explained in Section 3.3, the measured and/or estimated angular position, velocity, and acceleration signals are required to compute an impedance reference in torque control; whereas, an admittance reference is calculated using the measured torsion bar torque signal in position control. A straightforward mathematical representation for non-transparent haptic feedback based on Newton’s second law of motion requires reference inertia, damping, stiffness, and Coulomb friction parameters. In particular, the virtual stiffness function is non-trivial and depends on the modeled environment dynamics. For the desired steering feedback, certain aspects of the non-linear tire and vehicle dynamics must be included; the details are presented in Section 4.2.1.

The inclusion of actual environment interaction is the second excitation source, that also determines driver–environment transparency. The performance explicitly depends on the quality of the estimated disturbance, i.e., estimated rack force or equivalent rack torque signal, and its subsequent feedback to the reference model. The estimated rack torque can be superimposed with the virtual rack torque such that the resulting rack torque defines the required reference variable. Furthermore, this superimposition can be intelligently manipulated. A novel approach to control transparency by computing an “optimal” rack torque is proposed in Section 4.5.2, followed by some simulation results in Section 4.5.3.

For the last excitation source, an interface for handling the external signal requests from active safety functions within the reference model is discussed in Chapter 5. At this point,

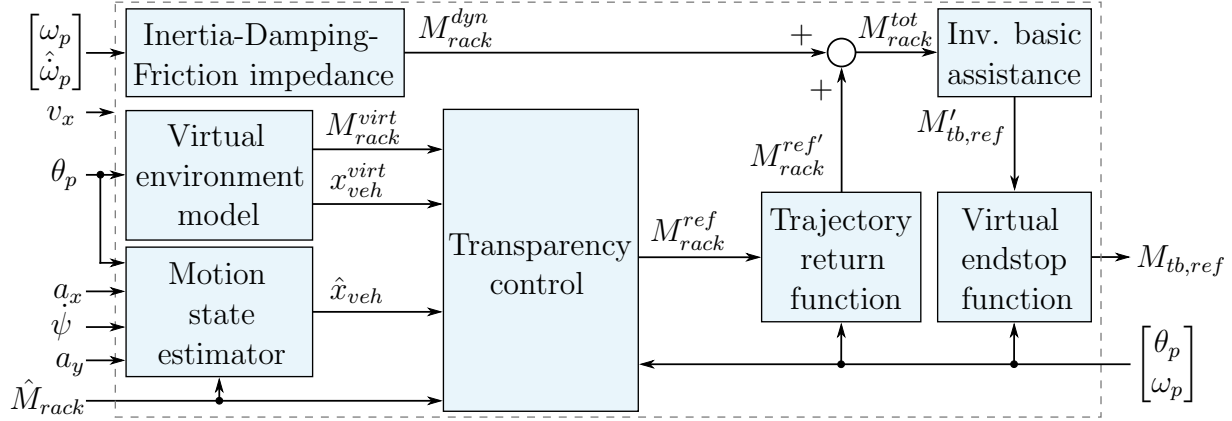


Figure 4.1: Schematic of control structure for deriving the torque (or impedance) reference trajectory using model-based haptic functions.

the two control structures for torque and position reference are introduced.

4.1.1 Torque reference

The reference torque is computed using different haptic functions and a variety of sensed and estimated signals. Figure 4.1 shows the corresponding reference model. Before discussing the purpose of each function and its mathematical description, some clarifications have to be mentioned. With respect to the *virtual environment model*, $M_{rack}^{virt}(t) = f(\theta_p(t), v_x)$ is the virtual rack torque variable; details are covered in the latter part of chapter. A simplified expression can be assumed here: $M_{rack}^{virt}(t) = c_{ref}\theta_p(t)$. Moreover, the estimated signals, i.e., rack torque (\hat{M}_{rack}) and pinion acceleration ($\hat{\omega}_p$), are assumed to be known. Moreover, the contribution of the *motion state estimator* is disregarded here.

Inertia–Damping–Friction impedance

The reference impedance dynamics, defined by M_{rack}^{dyn} , includes the following torque components: inertial, damping, and Coulomb friction. The respective parameters J_{ref} , b_{ref} , and $M_{ref,fric}^0$ are dependent on v_x , as described in Paper C. Subsequently, they are tuned for the desired steering feedback. The mathematical representation is given by Eq. (4.1). For computing the reference Coulomb friction ($M_{ref,fric}$), the Dahl model equation is integrated at each sample time, T_s , with the friction model stiffness, $c_{ref,fric}$, and peak friction, $M_{ref,fric}^0$.

$$\begin{aligned} M_{rack}^{dyn}(t) &= J_{ref}\hat{\omega}_p(t) + b_{ref}\omega_p(t) + M_{ref,fric}(t) \\ &= J_{ref}\hat{\omega}_p(t) + b_{ref}\omega_p(t) + \int_0^{T_s} c_{ref,fric} \left(\omega_p(t) - \frac{M_{ref,fric}(\tau)}{M_{ref,fric}^0} |\omega_p(t)| \right) d\tau \end{aligned} \quad (4.1)$$

A remark: the reference parameters should ideally be equal to the effective parameters in Eq. (3.7) from open loop control. A system identification procedure for estimating them is illustrated in Paper C from a typical EPAS system.

From the frequency response measurements, J_{ref} and b_{ref} were estimated for a linearized solution around the zero steering angle at different v_x values. Whereas, $M_{ref,fric}^0$ was estimated using a steady state maneuver. With the approach proposed in Paper C, a good initial point on J_{ref} , b_{ref} , and $M_{ref,fric}^0$ can be obtained for objectively tuning the steering feedback and eventually reaching the subjective acceptance.

Transparency control

The purpose of this block is to manipulate transparency by choosing appropriate weighting on the virtual rack torque, M_{rack}^{virt} , and the estimated rack torque, \hat{M}_{rack} , respectively. As a result, the effective rack torque variable, M_{rack}^{ref} , becomes

$$M_{rack}^{ref}(t) = (1 - \gamma_1)M_{rack}^{virt}(t) + \gamma_2\hat{M}_{rack}(t) \quad (4.2)$$

such that

$$0 \leq \gamma_1 \leq 1$$

$$0 \leq \gamma_2 \leq 1$$

$$\gamma_1 - \gamma_2 = 0$$

where γ_1 and γ_2 are the transparency gains on virtual and estimated rack torque variables. In an ideal case, they must be equal; however, they are separately introduced to achieve additional degrees of freedom (if necessary) while seeking *optimal* transparency, as presented later in Section 4.4. Previously, for simplicity, only γ was introduced in Eqs. (3.11) and (3.12).

The boundary conditions are: $\gamma_1 = \gamma_2 = 0$ for non-transparent steering feedback (such that M_{rack}^{virt} is fed through), and $\gamma_1 = \gamma_2 = 1$ for a fully transparent system (such that \hat{M}_{rack} is fed through).

Trajectory return function

As the name suggests, the *trajectory return* function controls the motion trajectory of steering system and safely brings the system toward (closed-loop) equilibrium starting from an initial position (x_0) other than equilibrium point (x_e), i.e., zero position. Although the nominal motion (i.e., excluding this function) must be stable, the aim is to further control energy dissipation by reducing initial acceleration and adding more damping.

A simple way, to execute this notion, is by changing the reference stiffness during the return motion. This implies a non-linear reference model, assuming a second-order inertia–spring–damper system. Hence, the following non-linear equation is used to change the reference stiffness component (or basically, M_{rack}^{ref}):

$$\delta(t) = 1 + (\delta_0 - 1)(1 - e^{-m(\theta_p(t)\omega_p(t))^2}) \quad (4.3)$$

where m is the energy dissipation rate, and δ_0 is the stiffness reduction factor. Consider the non-transparent case such that $M_{rack}^{ref'}(t) = \delta(t)c_{ref}\theta_p(t)$ can be obtained using the simplified definition of M_{rack}^{virt} . As a result, the stiffness is c_{ref} near the equilibrium point and $\delta_0 c_{ref}$ is the stiffness at $x_0(t) \neq x_e = 0$ during return motion. With the foregoing, stability can now be proved using second-order dynamics.

Proposition 1. Given the definition of $\delta(t)$ in Eq. (4.3), the non-linear equation of motion for a second-order system is as follows.

$$J_{ref}\dot{\omega}_p(t) = -b_{ref}\omega_p(t) - \delta(t)c_{ref}\theta_p(t) \quad (4.4)$$

Then, the system is stable and has less energy during the return trajectory, given by the condition $\theta_p(t)\omega_p(t) < 0$, if $m > 0$ and $\delta_0 < 1$.

Proof. During the return motion, the total mechanical energy of the system can be used to define the Lyapunov function, $V(\theta_p, \omega_p)$, as follows (the time operator notation “ t ” is dropped for convenience).

$$V(\theta_p, \omega_p) = \frac{1}{2}\delta c_{ref}\theta_p^2 + \frac{1}{2}J_{ref}\omega_p^2 \quad (4.5)$$

This function is globally positive definite because $\mathbf{x} = (\theta_p, \omega_p) \neq (0, 0) \implies V(\theta_p, \omega_p) > 0$ over the entire state-space. The time-derivative of $V(\theta_p, \omega_p)$ can be subsequently deduced and resolved as Eq. (4.6), using Eqs. (4.3) and (4.4).

$$\begin{aligned} \dot{V}(\theta_p, \omega_p) &= -b_{ref}\omega_p^2 + \frac{1}{2}c_{ref}\theta_p^2\dot{\delta} \\ &= -b_{ref}\omega_p^2 + m(\delta_0 - 1)(\theta_p\omega_p)(\omega_p^2 + \theta_p\dot{\omega}_p)e^{-m(\theta_p\omega_p)^2}c_{ref}\theta_p^2 \end{aligned} \quad (4.6)$$

The return condition, $\theta_p(t)\omega_p(t) < 0$, can be differentiated to obtain: $\omega_p(t)^2 + \theta_p(t)\dot{\omega}_p(t) < 0$. Using these results, $\dot{V}(\theta_p, \omega_p)$ becomes negative definite (for $\mathbf{x} \neq 0$) if $m > 0$ and $\delta_0 < 1$. Thus, the system is asymptotically convergent to $\mathbf{x} = 0$. \square

The conditions, $m > 0$ and $\delta_0 < 1$, intuitively mean that a less stiff system returns with reduced energy and low ω_p from its starting position, given that there is no driver torque input. The complete function is summarized in Algorithm 1, which is applied to the reference model.

Algorithm 1: Trajectory return function.

```

 $\delta_0 < 1$ ; // initialization
 $m > 0$ ; // initialization
if  $\theta_p(t)\omega_p(t) < 0$  then // return motion trajectory condition
    |  $\delta(t) = 1 + (\delta_0 - 1)(1 - e^{-m(\theta_p(t)\omega_p(t))^2})$ ;
    |  $M_{rack}^{ref'}(t) = \delta(t)M_{rack}^{ref}(t)$ ;
else
    |  $M_{rack}^{ref'}(t) = M_{rack}^{ref}(t)$ ;
end

```

The example shown in Fig. 4.2 exhibits the measured phase portrait of an EPAS system at $v_x = 0$ km/h. The steering wheel is manually rotated to an offset position (close to the end position), as separately shown in the first and third quadrants. Then, the driver releases the steering wheel to capture the return motion trajectory, i.e., highlighted in the second and fourth quadrants because $\theta_p(t)\omega_p(t) < 0$ holds. The trajectory return function with $m = 0.0145$ and $\delta_0 = 0.35$ compared with the nominal case (i.e., without the trajectory return function, as shown in Fig. 4.2(a)) reduces the peak in ω_p by approximately 50%.

4.1. Model structure

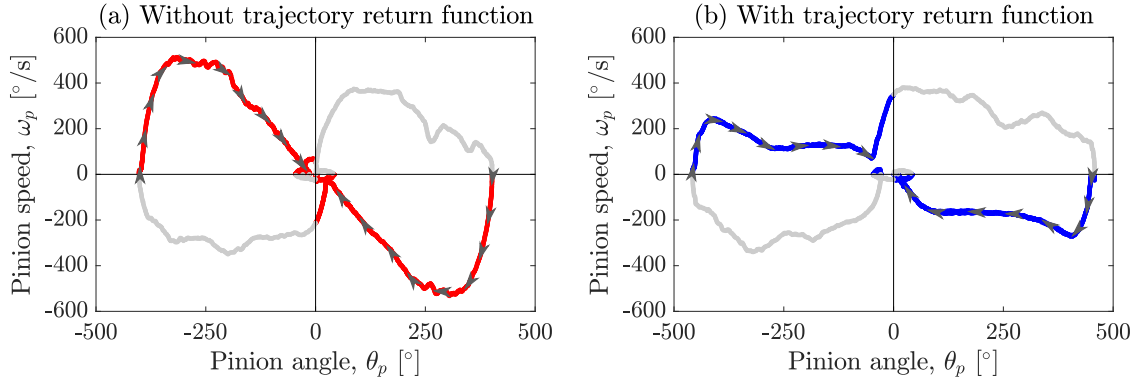


Figure 4.2: Measured phase portraits of an EPAS system at $v_x = 0$ km/h: (a) without and (b) with the trajectory return function; the highlighted trajectories signify the return motion.

Inverse basic assistance

This function is literally an inverse of the basic assistance introduced in Section 3.2.1. It implies that, at a given vehicle speed and quasi-static rack force (or equivalent M_{rack}^{tot}), how much should be the reference torque, $M'_{tb,ref}$, for a desired steady state steering feedback response. It can be formulated as follows:

$$M'_{tb,ref}(t) = (K'_{assist})^{-1} M_{rack}^{tot}(t) = (1 + K_{assist} i_{mot})^{-1} M_{rack}^{tot}(t) \quad (4.7)$$

where K_{assist} is defined in Eq. (3.1) and $M_{rack}^{tot}(t) = M_{rack}^{ref}(t) + M_{rack}^{dyn}(t)$.

A steady state maneuver can be performed to estimate K_{assist} from an existing open loop EPAS control for an initial tuning reference, as presented in Paper C. A typical v_x dependent K_{assist} characteristic can also be found in the same paper.

Virtual endstop function

To avoid reaching the mechanical end position of a given system, this function is required. The reference torque here is supplemented with an additional torque, $\Delta M_{tb,ref}$, when a certain position threshold ($\theta_{p,end}$) is exceeded, see Algorithm 2. The output reference torque, $M_{tb,ref}$, increases significantly between $\theta_{p,end}$ and actual endstop, given by Eq. (4.8), where $c_{ref,end}$ and $k_{ref,end}$ are the endstop stiffness and damping parameters, respectively.

$$\Delta M_{tb,ref}(t) = c_{ref,end}(|\theta_p(t)| - \theta_{p,end}) + k_{ref,end}|\omega_p(t)| \quad (4.8)$$

Algorithm 2: Virtual endstop function.

```

 $c_{ref,end} > 0$ ; // initialization
 $k_{ref,end} > 0$ ; // initialization
if  $|\theta_p(t)| > \theta_{p,end}$  then // endstop region condition
     $\Delta M_{tb,ref}(t) = c_{ref,end}(|\theta_p(t)| - \theta_{p,end}) + k_{ref,end}|\omega_p(t)|$ ;
     $M_{tb,ref}(t) = M'_{tb,ref}(t) + \text{sign}(\theta_p(t))\Delta M_{tb,ref}(t)$ ;
else
     $M_{tb,ref}(t) = M'_{tb,ref}(t)$ ;
end

```

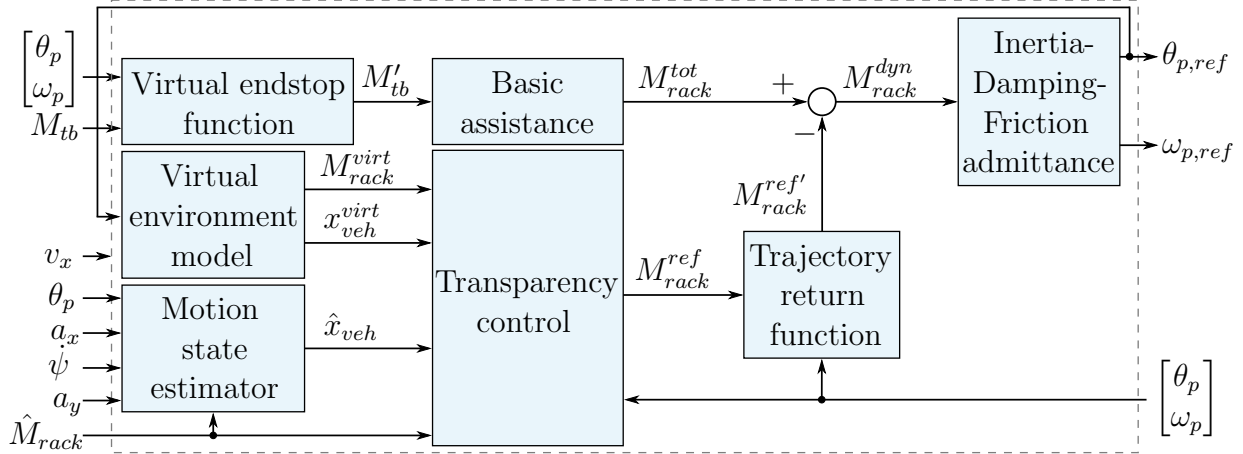


Figure 4.3: Schematic of control structure for deriving the position (or admittance) reference trajectory using model-based haptic functions.

4.1.2 Position reference

The reference angular position and velocity are the output variables of this model, as shown in Fig. 4.3. Due to opposing causality, the position reference model is complementary to the torque reference model in Fig. 4.1. Consequently, the *virtual endstop* function transforms into $M'_{tb}(t) = M_{tb}(t) - \text{sign}(\theta_p(t))\Delta M_{tb,ref}(t)$, where $\Delta M_{tb,ref}(t)$ is given by Eq. (4.8). The *basic assistance* function is defined as $M^{tot}_{rack}(t) = (1 + K_{assist}i_{mot})M'_{tb}(t)$ due to inversion from Eq. (4.7) of the torque reference model.

Furthermore, the *transparency control* and *trajectory return* functions have the same meaning and formulation as Eq. (4.2) and Algorithm 1, respectively. The backbone of this concept, i.e., the *admittance* function, is discussed as follows.

Inertia–Damping–Friction admittance

The dynamics of the reference admittance function is defined by the second-order differential equation (Eq. (4.9)). Again, the parameters J_{ref} , b_{ref} , and $M^0_{ref,fric}$ have the same meaning as previously defined and are v_x dependent. $M_{ref,fric}$ can be calculated using any state-of-the-art friction model, such as the Dahl model.

$$\begin{aligned}
 J_{ref}\dot{\omega}_{p,ref}(t) &= -b_{ref}\omega_{p,ref}(t) - M_{ref,fric}(t) + M^{dyn}_{rack}(t) \\
 &= -b_{ref}\omega_{p,ref}(t) - \int_0^{T_s} c_{ref,fric} \left(\omega_{p,ref}(t) - \frac{M_{ref,fric}(\tau)}{M^0_{ref,fric}} |\omega_{p,ref}(t)| \right) d\tau + M^{dyn}_{rack}(t)
 \end{aligned} \tag{4.9}$$

Given the reference parameters, the differential equation above generates the solution in terms of $\theta_{p,ref}(t)$ and $\omega_{p,ref}(t)$. Ideally, these parameters correspond to Eq. (4.1) provided that the stability conditions discussed in Section 3.5.1 are satisfied.

A remark: $M^{dyn}_{rack}(t)$ depends on the *virtual environment model*, which is a function of $\theta_{p,ref}(t)$ due to non-linear dynamics. Therefore, for real-time digital implementation, a time delay of T_s is required to avoid an algebraic loop in this model-based solution.

4.2 Non-transparency using virtual environment

This section presents an *environment model* for generating the virtual steering feedback. In EPAS, this is required during the attenuation of actual environmental by the feedback controller; whereas, due to mechanical disconnection in SbW, the virtual dynamics provide the only haptic sensation. Here, vehicle and tire models comprise the virtual dynamics. The causality requires the pinion angle as the input variable at a given vehicle speed and the rack torque is the output variable. Therefore, the proposed environment model represents a time-variant non-linear spring stiffness. This model is further termed as a *rack force model*.

4.2.1 Rack force model

Consider the 3-DOF two-track vehicle model introduced in Section 2.2 with lateral velocity (v_y) and yaw rate ($\dot{\psi}$) as state variables. Again, longitudinal dynamics are ignored, the equations of motion are linearized around a known v_x value, and a small wheel angle is assumed. The following equations of motion are derived in the body frame coordinate system (based on Eq. (2.7)) such that the input signals are the front and rear lateral tire forces (i.e., $F_{yf,l}$, $F_{yf,r}$, $F_{yr,l}$, and $F_{yr,r}$).

$$\begin{aligned}\dot{v}_y(t) &= -v_x\dot{\psi}(t) + \frac{1}{m}(F_{yf,l}(t) + F_{yf,r}(t) + F_{yr,l}(t) + F_{yr,r}(t)) \\ \ddot{\psi}(t) &= \frac{1}{J_z}(l_f(F_{yf,l}(t) + F_{yf,r}(t)) - l_r(F_{yr,l}(t) + F_{yr,r}(t)))\end{aligned}\quad (4.10)$$

The lateral tire slip angles are defined in Eq. (4.11). A modification of Eq. (2.8) is implemented by including the first-order dynamics given by the front and rear tire relaxation time constants, T_{0f} and T_{0r} , details are found in [161]. Moreover, the Ackerman geometry is included such that the inner wheel is steered more than the outer wheel. Consequently, $\delta_{f,l} = \delta_{f0}l/(l - \delta_{f0}w_f/2)$ and $\delta_{f,r} = \delta_{f0}l/(l + \delta_{f0}w_f/2)$, where $\delta_{f0} = \theta_p/i_{str}$ is the nominal wheel angle.

$$\begin{aligned}T_{0f}\dot{\alpha}_{f,l}(t) &= -\alpha_{f,l}(t) - \text{atan}\left(\frac{v_y(t) + l_f\dot{\psi}(t)}{v_x - w_f\dot{\psi}(t)/2}\right) + \delta_{f,l}(t) \\ T_{0f}\dot{\alpha}_{f,r}(t) &= -\alpha_{f,r}(t) - \text{atan}\left(\frac{v_y(t) + l_f\dot{\psi}(t)}{v_x + w_f\dot{\psi}(t)/2}\right) + \delta_{f,r}(t) \\ T_{0r}\dot{\alpha}_{r,l}(t) &= -\alpha_{r,l}(t) - \text{atan}\left(\frac{v_y(t) - l_r\dot{\psi}(t)}{v_x - w_r\dot{\psi}(t)/2}\right) \\ T_{0r}\dot{\alpha}_{r,r}(t) &= -\alpha_{r,r}(t) - \text{atan}\left(\frac{v_y(t) - l_r\dot{\psi}(t)}{v_x + w_r\dot{\psi}(t)/2}\right)\end{aligned}\quad (4.11)$$

Equations (4.10) and (4.11) can now be used to formulate a non-linear vehicle model:

$$\dot{\mathbf{x}}_{veh}^{virt}(t) = \mathbf{f}(\mathbf{x}_{veh}^{virt}(t), \mathbf{u}_{veh}^{virt}(t))$$

where $\mathbf{x}_{veh}^{virt}(t) = [v_y \ \dot{\psi} \ \alpha_{f,l} \ \alpha_{f,r} \ \alpha_{r,l} \ \alpha_{r,r}]^T$ and $\mathbf{u}_{veh}^{virt}(t) = [F_{yf,l} \ F_{yf,r} \ F_{yr,l} \ F_{yr,r} \ \delta_{f,l} \ \delta_{f,r}]^T$ are state and input vectors, respectively. A further simplification can be to resolve these

Table 4.1: Frequency response parameter identification for a linear rack force model

Parameters	Measured signals	Frequency range
$C_{\alpha_f}, C_{\alpha_r}$	$v_y, \dot{\psi}, a_y$	0.2 – 0.5 Hz
J_z	$v_y, \dot{\psi}, a_y$	0.2 – 5 Hz
t_{pf}	F_{rack}	0.2 – 0.5 Hz
T_{0f}, T_{0r}	F_{rack}	0.2 – 5 Hz

equations for a single-track vehicle model, similar to Eq. (2.10), such that $F_{yf,l} + F_{yf,r} = F_{yf}$, $F_{yr,l} + F_{yr,r} = F_{yr}$, $\alpha_{f,l} = \alpha_{f,r} = \alpha_f$ and $\alpha_{r,l} = \alpha_{r,r} = \alpha_r$.

The next step is to compute the lateral tire forces using an appropriate tire model. For a single track model with linear tires, $F_{yf} = C_{\alpha_f} \alpha_f$ and $F_{yr} = C_{\alpha_r} \alpha_r$ can be used in Eq. (4.10), where C_{α_f} and C_{α_r} are the front and rear axle tire cornering stiffness. Subsequently, the virtual rack force is given by $F_{rack}^{virt} = i_{rp} M_{rack}^{virt}$, and the virtual rack torque is

$$M_{rack}^{virt}(t) = \frac{1}{i_{str}}(t_{pf} + t_m)F_{yf}(t) = \frac{1}{i_{str}}(t_{pf} + t_m)C_{\alpha_f}\alpha_f(t) \quad (4.12)$$

where t_{pf} is the nominal tire pneumatic trail and t_m is the mechanical trail. This linear rack force model is proposed in Paper C, which also shows how to identify the unknown parameters under a nominal road condition, as summarized in Table 4.1. The stated parameters can be identified by minimizing the mean squared error between measured and model FRFs for the corresponding measured signals with δ_{f0} as the input variable. Moreover, the specific frequency range listed in Table 4.1 highlights the domain of interest for the optimization problem. The effective tire parameters C_{α_f} , C_{α_r} , and t_{pf} vary over v_x due to vehicle suspension effects. Therefore, the same procedure must be performed at different vehicle speeds, as described in Paper C.

Though the linear aspects of the aforementioned rack force model at low and high frequencies are captured under nominal road conditions; however, its foremost limitation is the absence of a non-linear steady state tire characteristic, as stated in Paper C. As a result, the performance is only valid up to 4 m/s² lateral acceleration (i.e., $\approx 40\%$ of the peak value), subsequently corresponding to low magnitude lateral tire slip angles. This drawback can be overcome by including a non-linear tire model. To achieve more expected *non-transparency*, the foregoing point is discussed next, thereby extending the results presented in Paper C.

To realize non-linear tire behavior, the Pacejka tire model equation described in [137] is used. The lateral tire force is given by the following expression:

$$F_{y,i} = D_{y,i} \sin \left(C_{y,i} \operatorname{atan}(B_{y,i} \alpha_i) - E_{y,i} (B_{y,i} \alpha_i - \operatorname{atan}(B_{y,i} \alpha_i)) \right) \quad (4.13)$$

where

$$\begin{aligned} D_{y,i} &= \sqrt{(\lambda_{\mu y,i} \mu_{y0} F_{z,i})^2 - F_{x,i}^2} \\ K_{y,\alpha_i} &= C_{\alpha_i,0} \sin \left(2 \operatorname{atan}(F_{z,i} / (p K_{y,i} F_{z,nom})) \right) \lambda_{K y,i} \quad \text{and} \\ B_{y,i} &= K_{y,\alpha_i} / (C_{y,i} D_{y,i}). \end{aligned}$$

4.2. Non-transparency using virtual environment

Moreover, $\lambda_{\mu y,i}$, $\lambda_{Ky,i}$, and $p_{Ky,i}$ are the tuning parameters; μ_{y0} is the peak lateral tire-road friction coefficient; $D_{y,i}$ is the maximum lateral tire force potential; $C_{y,i}$ and $F_{z,nom}$ are tire model parameters. Because longitudinal dynamics are neglected, the longitudinal tire forces are assumed null, i.e., $F_{x,i} = 0$ N. The vertical tire forces, $F_{z,i}$, can be chosen as either static, given by $F_{zf0} = mgl_r/(2l)$ and $F_{zr0} = mgl_f/(2l)$, or under a load transfer condition, such as for a rigid axle suspension. For the latter, the measured longitudinal and lateral acceleration signals (i.e., a_x and a_y) are required, as follows:

$$F_{zf,i} = \frac{mgl_r}{2l} \left(1 \mp \frac{2h_{cg}}{w_f} \frac{a_y}{g} + \frac{h_{cg}}{l_r} \frac{a_x}{g} \right) \text{ and } F_{zr,i} = \frac{mgl_f}{2l} \left(1 \mp \frac{2h_{cg}}{w_r} \frac{a_y}{g} - \frac{h_{cg}}{l_f} \frac{a_x}{g} \right) \quad (4.14)$$

where g is gravitational acceleration; h_{cg} is the height of the center of gravity (CG) from the ground; w_f and w_r are the front and rear track widths, respectively.

Finally, Eqs. (4.10), (4.11), (4.13), and (4.14) can be solved altogether, given δ_{f0} and v_x , to derive the lateral tire forces. Then, to compute the rack torque variable, the front tire pneumatic trail, t_{pf} , is required. According to the Pacejka tire model [137], it is defined as

$$t_{pf,i} = t_{pf} \cos \left(C_{tf} \operatorname{atan}(B_{tf} \alpha_{f,i}) - E_{tf} (B_{tf} \alpha_{f,i} - \operatorname{atan}(B_{tf} \alpha_{f,i})) \right) \quad (4.15)$$

where B_{tf} , C_{tf} , and E_{tf} are the tire model parameters. Subsequently, the virtual rack torque can be defined using $F_{y,i}$ and $t_{pf,i}$ from Eqs. (4.13) and (4.15), respectively, as follows.

$$M_{rack}(t) = \frac{1}{i_{str}} \left((t_{pf,l}(t) + t_m) F_{yf,l}(t) + (t_{pf,r}(t) + t_m) F_{yf,r}(t) \right) \quad (4.16)$$

The next question is, how can the unknown tire model parameters for the rack force model be estimated? For this, a slow ramp steer maneuver at a given v_x value was performed to capture the non-linear steady state effects. The road conditions were nominal (i.e., flat, uniform, and dry road surface) with $\mu_{y0} \approx 1$. The measured signals are v_y , $\dot{\psi}$, a_y , and F_{rack} , as shown in Fig. 4.4 and 4.5 at 75 km/h and 90 km/h, respectively. These signals were synchronized and sampled at $T_s = 10$ ms and the maneuver end time is given by t_1 . The measurements were performed on a Volvo S90 vehicle with a standard tire configuration.

The steady state condition implies that $\dot{\mathbf{x}}_{veh}^{virt}(t) = 0 \implies \mathbf{f}(\mathbf{x}_{veh}^{virt}(t), \mathbf{u}_{veh}^{virt}(t)) = 0$. Using the measured quantities (v_y and $\dot{\psi}$) and input δ_{f0} at a given v_x value, Eq. (4.11) can be solved for the steady state tire slip angles. Similarly, the front and rear axle lateral tire forces, F_{yf} and F_{yr} , can be computed from Eq. (4.10), given $(\dot{v}_y, \ddot{\psi}) = (0, 0)$. The results are shown in Fig. 4.4 and 4.5, where the corresponding axle slip angle is given by the mean of the left and right tire slip angles.

The constrained non-linear optimization problem in Eq. (4.17) can be independently solved for each axle to estimate the individual lateral tire forces, $F_{y,i}^{virt}$, defined by Eq. (4.13). Basically, the squares of $F_{yf} - (F_{yf,l}^{virt} + F_{yf,r}^{virt})$ and $F_{yr} - (F_{yr,l}^{virt} + F_{yr,r}^{virt})$ are minimized. Thus, Eqs. (4.11), (4.13), and (4.14) are a part of the objective function. The following is assumed for simplicity: $E_{y,i} = 0$ and $a_x \approx 0$ m/s². The initial value of unknown parameters can be selected from the tire data file (if provided by the tire manufacturer) or as unity.

$$\begin{aligned} & \underset{\Theta = [C_{y,i} \ \lambda_{\mu y,i} \ \lambda_{Ky,i} \ p_{Ky,i}]^T}{\text{minimize}} & \sum_{k=1}^{t_1/T_s} (F_{y,i}(k) - F_{y,i}^{virt}(k))^2 \\ & \text{subject to} & \Theta_0 = \mathbf{I}_{4 \times 4}, \quad \Theta^- < \Theta < \Theta^+ \end{aligned} \quad (4.17)$$

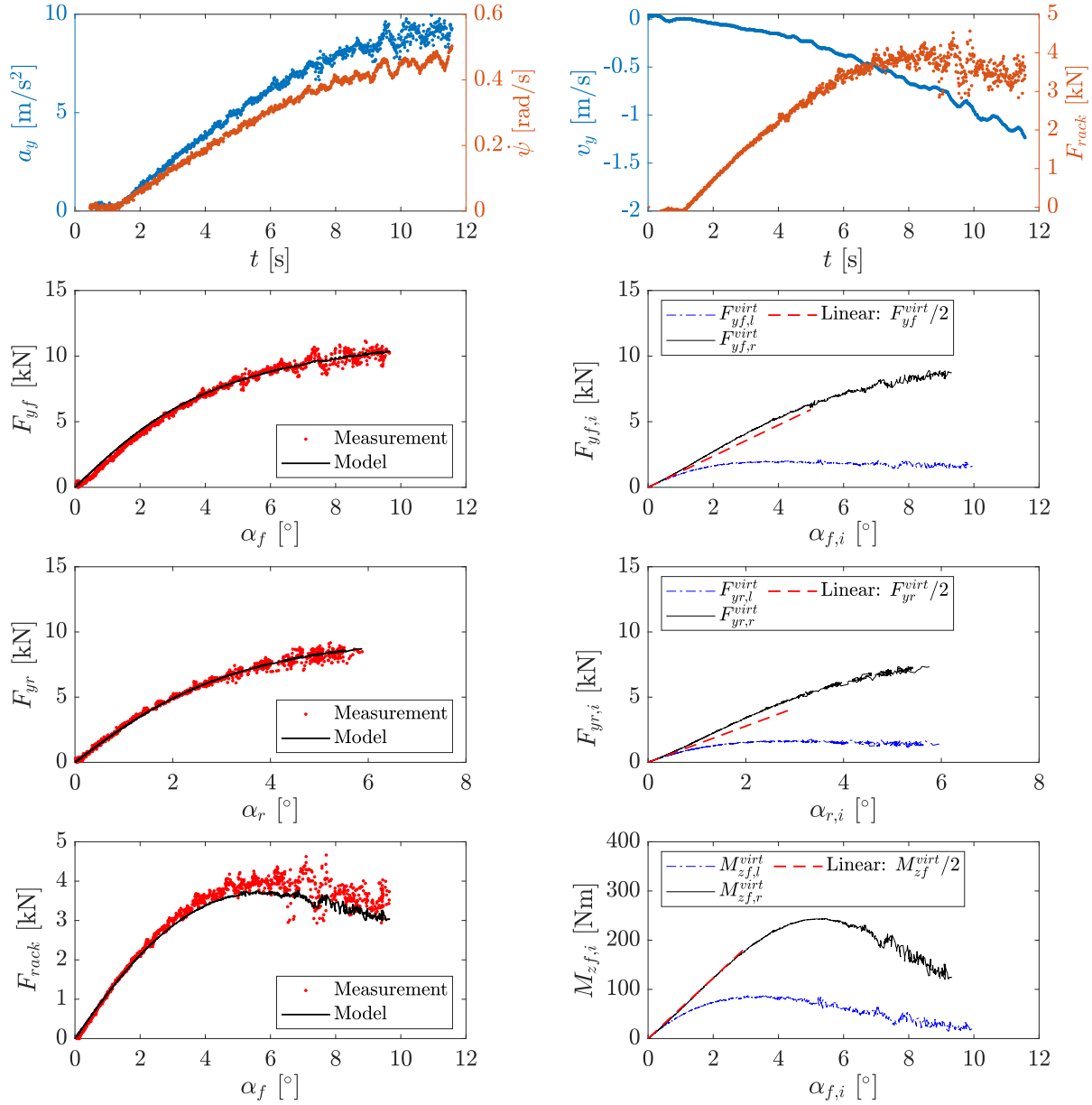


Figure 4.4: Slow ramp steer maneuver performed at 75 km/h with the measured signals, a_y and $\dot{\psi}$ (top left) and v_y and F_{rack} (top right). The following are plotted: the measured and modeled front axle (second row, left) and rear axle (third row, left) lateral forces versus the corresponding axle slip angle; the modeled front (second row, right) and rear (third row, right) lateral tire forces versus the corresponding tire slip angle; the measured and modeled rack forces versus the front axle slip angle (bottom left); and the modeled front tire aligning moment versus the corresponding front tire slip angle (bottom right).

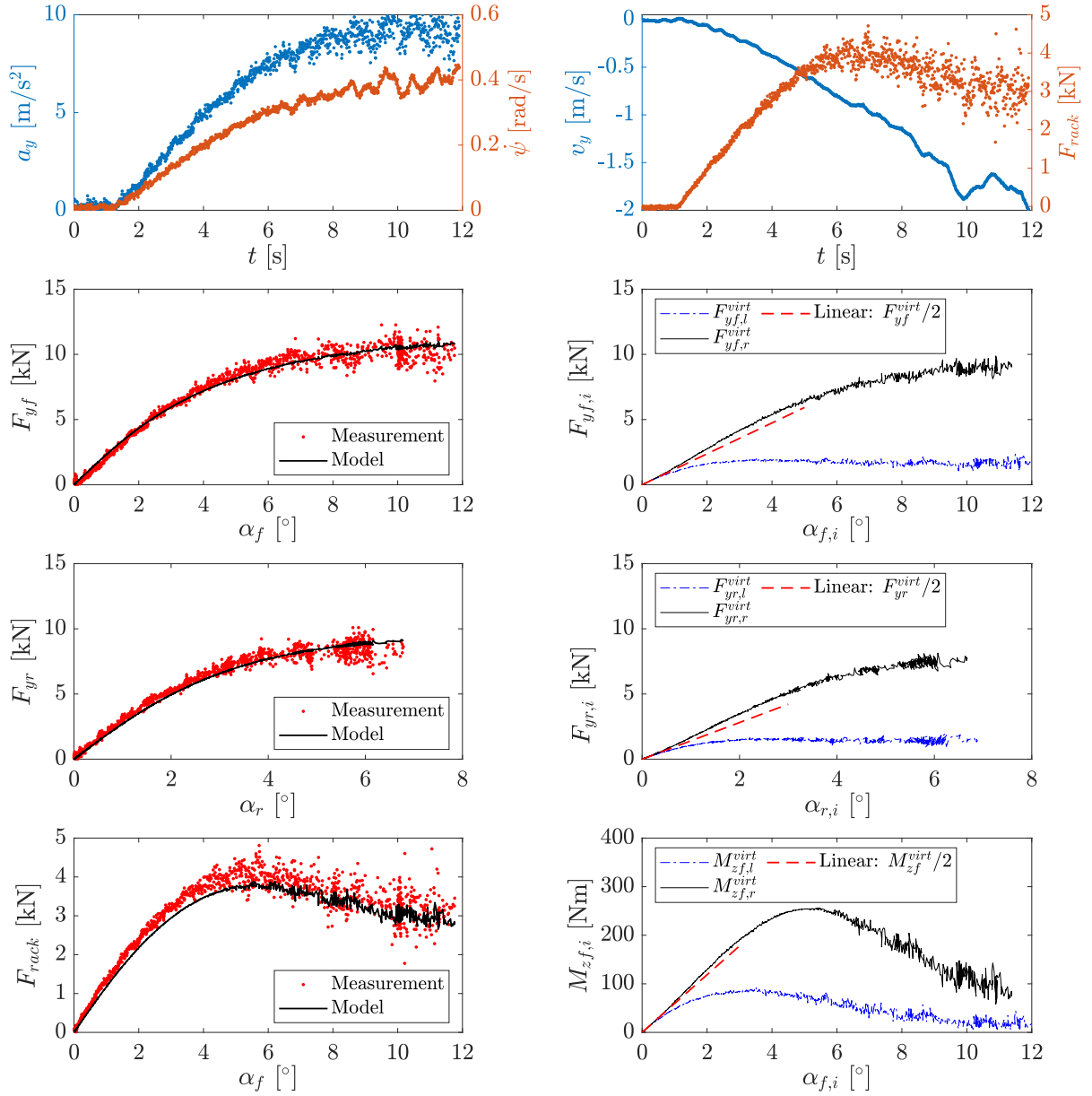


Figure 4.5: Slow ramp steer maneuver performed at 90 km/h with the measured signals, a_y and $\dot{\psi}$ (top left) and v_y and F_{rack} (top right). The following are plotted: the measured and modeled front axle (second row, left) and rear axle (third row, left) lateral forces versus the corresponding axle slip angle; the modeled front (second row, right) and rear (third row, right) lateral tire forces versus the corresponding tire slip angle; the measured and modeled rack forces versus the front axle slip angle (bottom left); and the modeled front tire aligning moment versus the corresponding front tire slip angle (bottom right).

Table 4.2: Steady state parameter identification for a non-linear rack force model

Vehicle speed	$C_{y,f}$	$\lambda_{\mu y,f}$	$\lambda_{Ky,f}$	$p_{Ky,f}$	$C_{y,r}$	$\lambda_{\mu y,r}$	$\lambda_{Ky,r}$	$p_{Ky,r}$	C_{tf}	B_{tf}	E_{tf}
75 km/h	0.940	0.988	0.499	10.02	1.235	0.982	0.508	9.980	1.091	1.276	-7.89
90 km/h	0.953	0.982	0.409	9.991	1.309	0.978	0.369	10.03	1.088	1.273	-7.78

The lateral tire forces from parameter estimation (or fitted model) are shown in Fig. 4.4 and 4.5. These plots also show the linearized response from Paper C such that the quantities are halved from the total axle response to represent on each wheel.

In the last step, parameters C_{tf} , B_{tf} , and E_{tf} are estimated for the front tire pneumatic trail using the measured F_{rack} signal. Here, the square of $F_{rack} - i_{rp} M_{rack}^{virt}$ is minimized to estimate the unknown parameters. M_{rack}^{virt} is computed using Eqs. (4.15), (4.16), and the previously modeled front lateral tire forces, $F_{yf,l}^{virt}$ and $F_{yf,r}^{virt}$. The modeled rack force result is shown in Fig. 4.4 and 4.5. Similarly, the front tire aligning moment can also be calculated and plotted, as given by $M_{zf,i}^{virt} = t_{pf,i}^{virt} F_{yf,i}^{virt}$. The estimated Pacejka tire model parameters from these optimization steps are also summarized in Table 4.2.

In summary, this section (including Paper C) briefly describes an approach to model an environment using measurement data for virtual steering feedback. The aforementioned rack force (or virtual environment) model can be suitably implemented for the torque reference (Fig. 4.1) and position reference (Fig. 4.3). The sequential optimization steps presented in this section can be improved for better results. However, the choice of optimization method was not the primary focus. The section centered on the means for computing a sufficient virtual rack torque, M_{rack}^{virt} , by capturing the important elements of vehicle and tire dynamics, ultimately generating the required haptic feedback.

4.2.2 Evaluation of non-transparent setting

The basic performance of the virtual environment model (Section 4.2.1) and its effect on the non-transparent steering feedback setting are discussed in this section. The two primary aspects considered in the proposed haptic response are: (a) non-linear steady state and (b) frequency response phenomena. Paper C presents the results on each aspect with a linear rack force model in closed-loop EPAS and SbW-FFb. However, as explained, it lacked the non-linear steady state tire performance, which is important for illustrating the virtual vehicle handling limit around high lateral acceleration values.

Using the proposed non-linear rack force model and previously defined haptic functions, the EPAS results can be seen in Fig. 4.6 and 4.7 from driving on a proving ground under nominal road conditions; the implemented settings were non-transparent torque and position control, respectively. The rack force plot also shows the difference between virtual (F_{rack}^{virt}) and actual (F_{rack}^{act}) rack force signals, defined by $e_{F_{rack}}$. The difference is small during normal driving except at the limit of handling, i.e., around $a_y \approx \pm 9 \text{ m/s}^2$. The contributing factors include tire-road interaction uncertainty, low fidelity rack force model due to unmodeled suspension effects, and the disregard of longitudinal dynamics.

4.2. Non-transparency using virtual environment

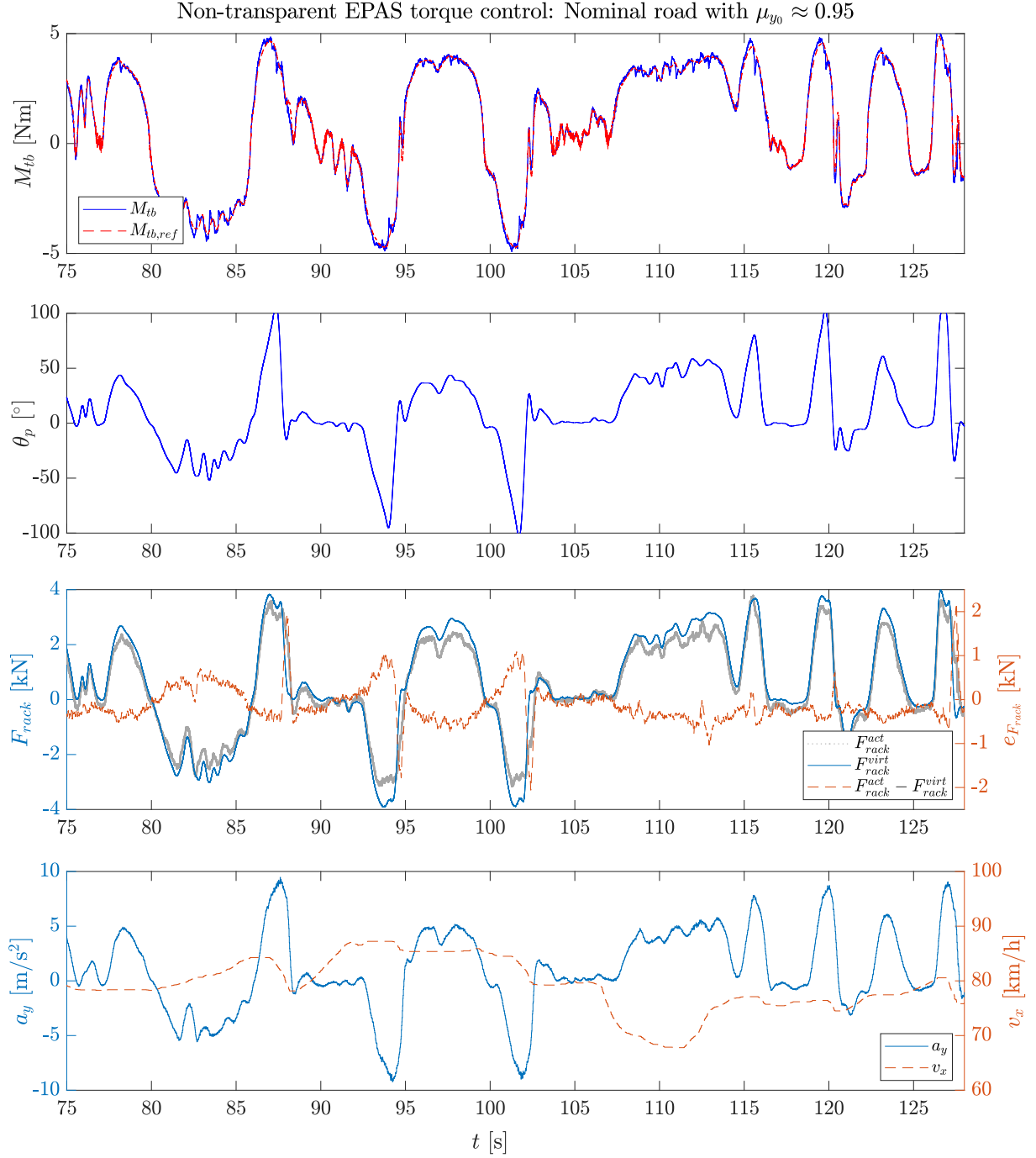


Figure 4.6: A non-transparent EPAS torque control response measured on proving ground (during closed-circuit driving) under nominal road conditions ($\mu_{y_0} \approx 0.95$) and varying v_x . The time-based signals are: pinion torque (top), pinion angle (second from top), rack force (third from top), lateral acceleration, and vehicle speed (bottom).

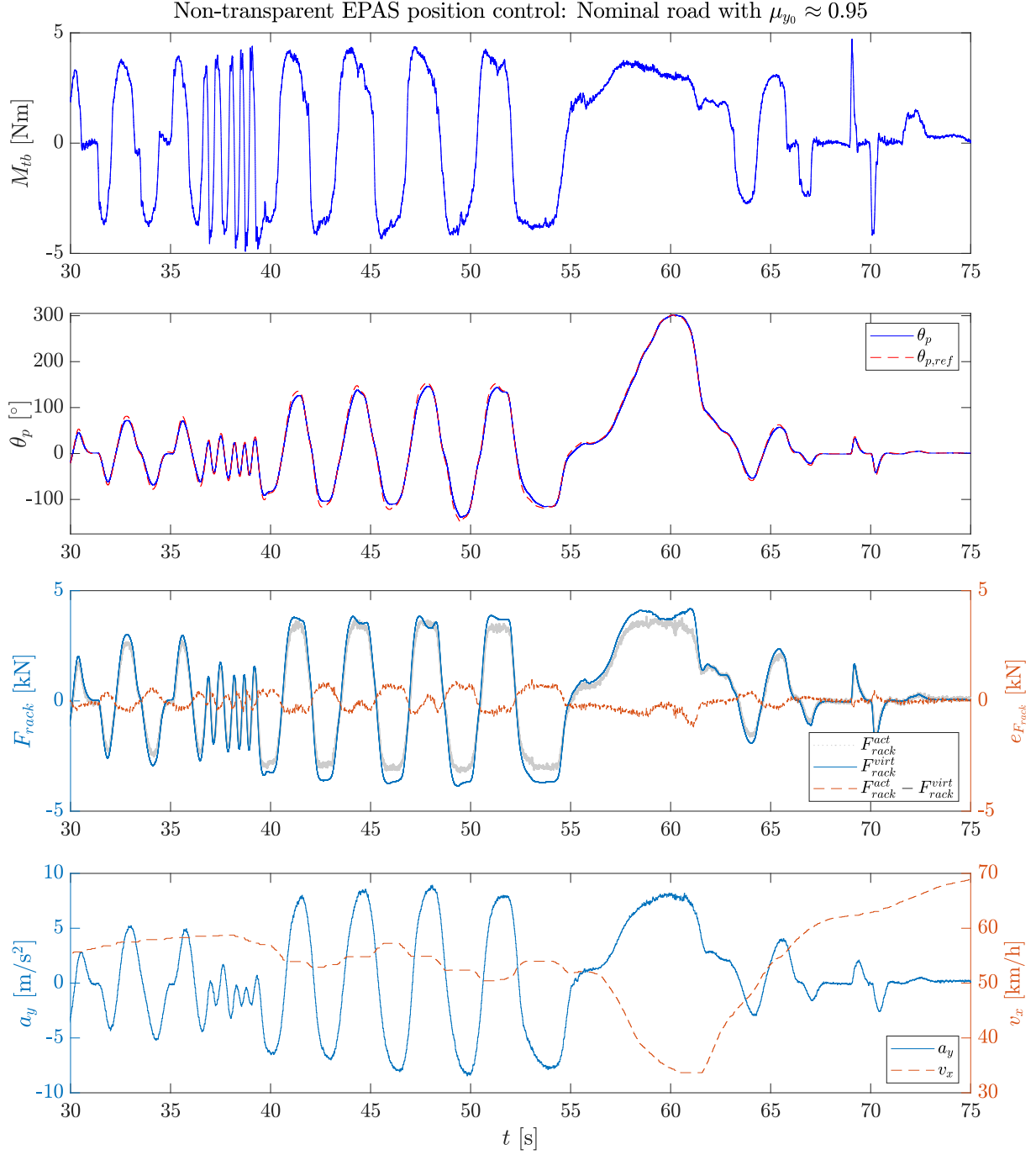


Figure 4.7: A non-transparent EPAS position control response measured on proving ground (during closed-circuit driving) under nominal road conditions ($\mu_{y0} \approx 0.95$) and varying v_x . The time-based signals are: pinion torque (top), pinion angle (second from top), rack force (third from top), lateral acceleration, and vehicle speed (bottom).

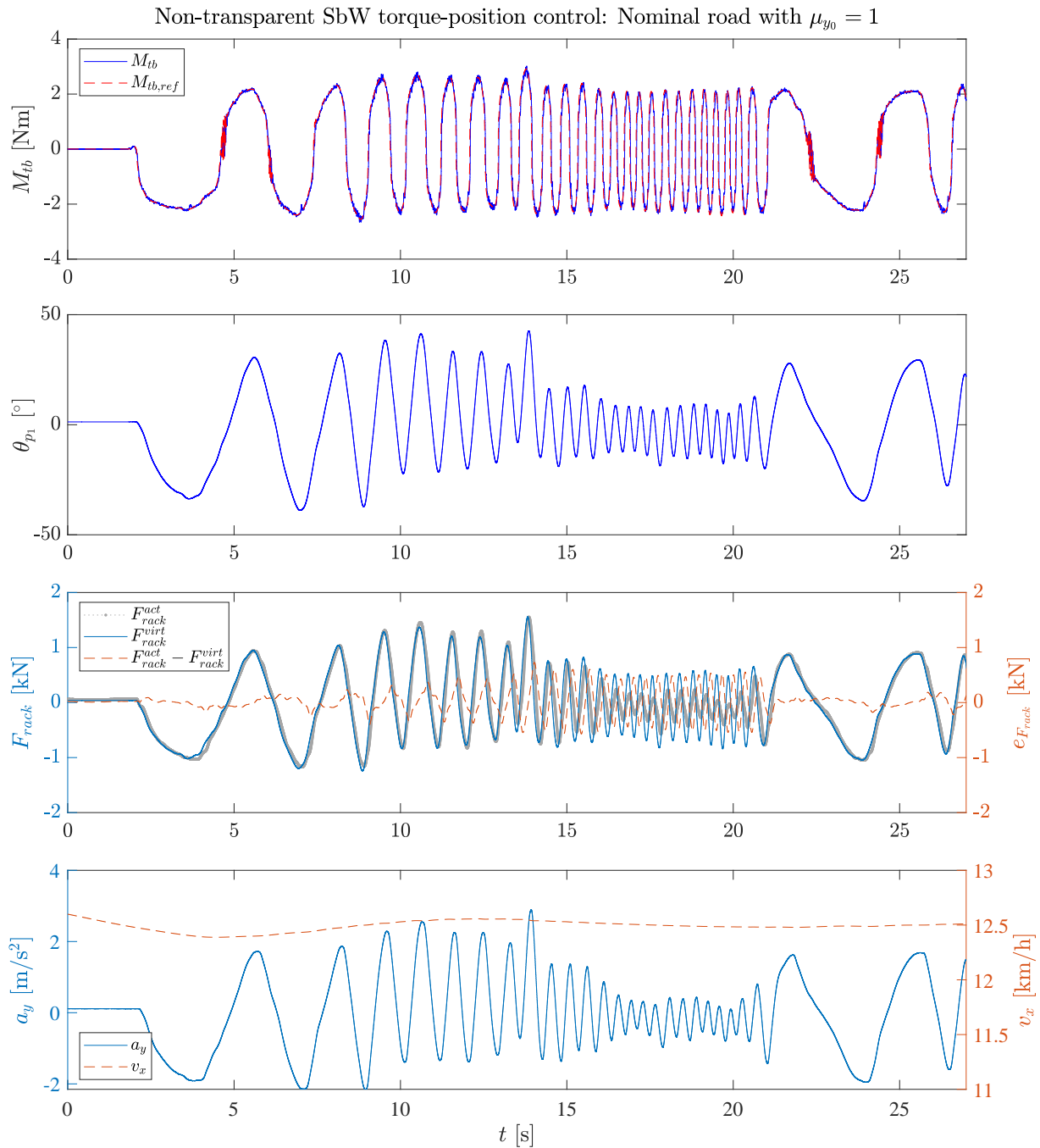


Figure 4.8: A non-transparent SbW torque-position control response measured on HIL test rig under nominal road conditions ($\mu_{y0} = 1$) and $v_x = 45$ km/h. The time-based signals are: FFb pinion torque (top), FFb pinion angle (second from top), rack force (third from top), lateral acceleration, and vehicle speed (bottom).

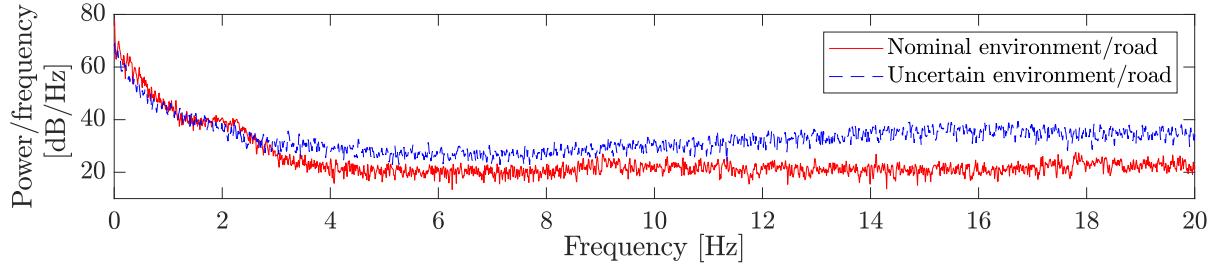


Figure 4.9: Power spectral density of F_{rack}^{act} signal from two different road surfaces.

In Fig. 4.6 and 4.7, the reference variables, $M_{tb,ref}$ and $\theta_{p,ref}$, are a function of $F_{rack}^{virt}(t)$. Hence, the virtual non-linear steady state tire response is clearly reflected in $M_{tb}(t)$, because it starts to drop simultaneously with $F_{rack}^{virt}(t)$ despite the increase in $\theta_p(t)$. This extends the previous result presented in Paper C. Similarly, non-transparent haptic performance can be achieved in SbW using the same reference model. For the SbW-FFb torque control, a sine sweep result is shown in Fig. 4.8. It involves a position controlled SbW-rack that commands a real-time HIL vehicle model (in IPG CarMaker). For the non-transparent setting in SbW, no signal communication is required from the HIL vehicle model to the FFb actuator.

An important remark: the admittance reference in the outer loop sufficiently requires a stable tuning due to low (inner loop) position controller cut-off frequency, as illustrated in Section 3.5.2. In theory, J_{ref} setpoint must satisfy Eq. (3.27); however, a large J_{ref} implies a small loop gain in Eq. (3.13), thus conservatively ensuring stability. A small ω_{in} for the position controller caused J_{ref} to be four times higher than the nominal value in torque control. Similarly, the selected b_{ref} value was twice its nominal value for stability reasons, again based on the small gain arguments. Consequently, the steering feedback performance represented slow dynamics and highly damped behavior; hence, it was found inferior. Accordingly, only torque control is further considered in the transparency section.

Because the virtual rack force model is employed for non-transparency, it cannot replicate reality in case of environmental disturbance or uncertainty. Consider driving on an uncertain road where the lateral tire-road grip conditions are slippery and varying. Then, F_{rack}^{virt} can significantly diverge from F_{rack}^{act} even under normal operating conditions. As a result, a high rack force error (i.e., $e_{F_{rack}} = F_{rack}^{act} - F_{rack}^{virt}$) can occur. To illustrate this, the power spectral density plot of the measured rack force signal obtained from two different road surfaces during closed-circuit driving is shown in Fig. 4.9. A nominal environment, on which the virtual rack force is based, has a higher power spectrum at low frequencies (up to 3 Hz) due to higher lateral tire-road grip. However, beyond 4 Hz (excluding the signal noise), no useful energy content exists. Whereas, in the case of an uncertain environment, i.e., driving on an icy road surface, the power spectral density is lower at low frequencies due to lower lateral tire-road grip. However, a higher power spectrum at high frequencies due to varying lateral tire-road grip occurs, thus implying useful road feedback information.

An example is shown in Fig. 4.10, where a vehicle is operating at extremely high lateral tire slip angles on a slippery road surface with low μ_{y0} at $t \approx 50$ s. As a result, $e_{F_{rack}}$ is large at these time instants, indicating the necessity of improving F_{rack}^{virt} during an environmental uncertainty. Accordingly, the next question is: how can *transparency* be achieved?

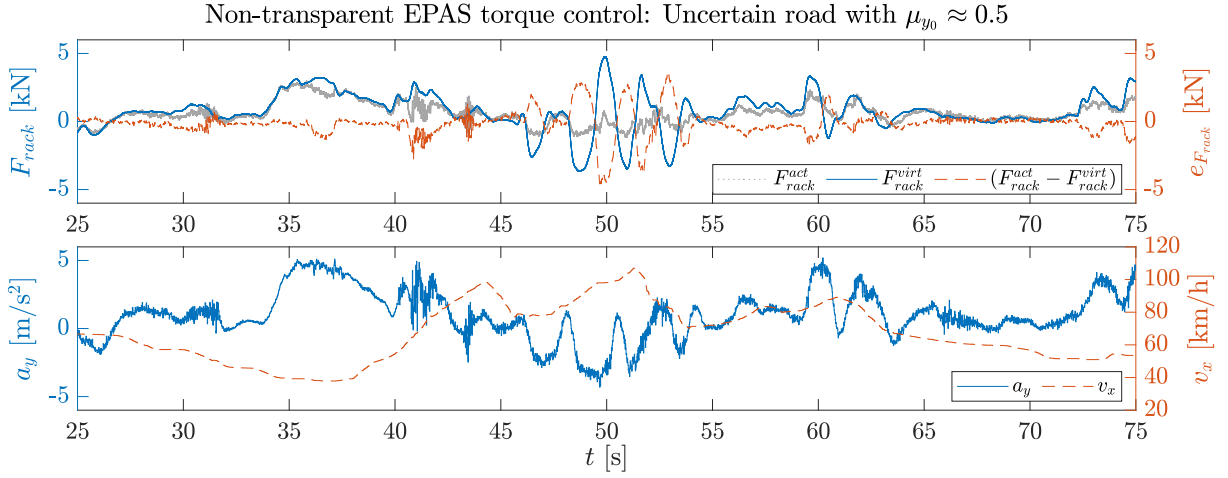


Figure 4.10: A time-based measurement of rack force (top), lateral acceleration, and vehicle speed (bottom) under uncertain and varying road conditions (with $\mu_{y0} \approx 0.5$) while drifting.

4.3 Disturbance estimation

To determine the human–environment transparency in a haptic feedback system, regardless of the configuration, the actual environment interaction dynamics should be estimated and fed back to the reference model. This is the motivation behind the discussion of disturbance estimation. Here, the focus is on estimating the rack force (or rack torque) variable through a disturbance observer (Fig. 3.7) and then the estimated signal can eventually be used for deriving the transparent steering feedback. This section covers an overview of the work presented in Paper D.

Two rack force estimation strategies are introduced for comparison; these are based on (a) vehicle motion sensor signals and (b) steering system sensor signals. In the former, the vehicle motion reaction is used to estimate the rack force due to a cause-and-effect relationship. In the later, the estimation is directly performed at the environment port, i.e., the steering rack. These methods are briefly discussed as follows.

4.3.1 Vehicle motion based observer

The vehicle motion based rack force estimate follows an approach considerably similar to that explained in Section 4.2.1. The fundamental difference between the two is the inclusion of an estimation algorithm, such as Extended Kalman Filter (EKF) and Unscented Kalman Filter (UKF), based on the inertial measurement unit (IMU) signals: ψ and a_y . Consequently, this method is dependent on the fidelity of the vehicle and tire models.

To incorporate a time-varying change in the peak lateral tire–road friction coefficient in Eq. (4.13), as defined by $\Delta\mu_{y,i}$ and described in Paper D, the tire model should be modified. This would ensure that the equations are updated according to the road surface. Hence, the modified expression is $D_{y,i}(t) = \sqrt{((\mu_{y0} - \Delta\mu_{y,i}(t))F_{z,i}(t))^2 - F_{x,i}(t)^2}$.

The estimation algorithm is applied to the combination of Eqs. (4.10), (4.11), (4.13), and (4.15). The input signals are $\delta_{f,l}$, $\delta_{f,r}$, and $F_{z,i}$ from Eq. (4.14) at a given v_x value. In

the discrete-time domain, these equations can be represented as

$$\mathbf{x}_{t+1}^{veh} = \mathbf{f}(\mathbf{x}_t^{veh}, \mathbf{u}_t^{veh}) + \mathbf{q}_t^{veh} \text{ and } \mathbf{y}_t^{veh} = \mathbf{h}(\mathbf{x}_t^{veh}) + \mathbf{r}_t^{veh} \quad (4.18)$$

where $\mathbf{x}_t^{veh} = [v_y \ \dot{\psi} \ \alpha_{f,l} \ \alpha_{f,r} \ \alpha_{r,l} \ \alpha_{r,r} \ \Delta\mu_{yf,l} \ \Delta\mu_{yf,r} \ \Delta\mu_{yr,l} \ \Delta\mu_{yr,r}]^T$ is the state vector; $\mathbf{u}_t^{veh} = [F_{zf,l} \ F_{zf,r} \ F_{zr,l} \ F_{zr,r} \ \delta_{f,l} \ \delta_{f,r}]^T$ are inputs; $\mathbf{y}_t^{veh} = [\psi \ a_y]^T$ are outputs; \mathbf{q}_t^{veh} and \mathbf{r}_t^{veh} are the state and output noise covariance. The estimation algorithm yields $\hat{\mathbf{x}}_{t|t}^{veh}$.

The augmented state-space formulation shown below should be implemented for the EKF state estimation of a non-linear model (derived by linearization):

$$\begin{bmatrix} \mathbf{x}_{t+1}^{veh} \\ 1 \end{bmatrix} = \mathbf{F} \begin{bmatrix} \mathbf{x}_t^{veh} \\ 1 \end{bmatrix} + \mathbf{G}\mathbf{u}_t^{veh} + \begin{bmatrix} \mathbf{q}_t^{veh} \\ 0 \end{bmatrix} \text{ and } \mathbf{y}_t^{veh} = \mathbf{H} \begin{bmatrix} \mathbf{x}_t^{veh} \\ 1 \end{bmatrix} + \mathbf{r}_t^{veh} \quad (4.19)$$

where

$$\mathbf{F} = \begin{bmatrix} \frac{\partial \mathbf{f}}{\partial \mathbf{x}}|_{\hat{\mathbf{x}}_{t|t}, \mathbf{u}_t} & \mathbf{f}(\hat{\mathbf{x}}_{t|t}, \mathbf{u}_t) - \frac{\partial \mathbf{f}}{\partial \mathbf{x}}|_{\hat{\mathbf{x}}_{t|t}, \mathbf{u}_t} \hat{\mathbf{x}}_{t|t} \\ 0 & 1 \end{bmatrix}; \mathbf{G} = \begin{bmatrix} \frac{\partial \mathbf{f}}{\partial \mathbf{u}}|_{\hat{\mathbf{x}}_{t|t}, \mathbf{u}_t} \\ 0 \end{bmatrix}; \mathbf{H} = \begin{bmatrix} \mathbf{h}(\hat{\mathbf{x}}_{t|t}) - \frac{\partial \mathbf{h}}{\partial \mathbf{x}}|_{\hat{\mathbf{x}}_{t|t}} \hat{\mathbf{x}}_{t|t} \\ \frac{\partial \mathbf{h}}{\partial \mathbf{x}}|_{\hat{\mathbf{x}}_{t|t}} \hat{\mathbf{x}}_{t|t} \end{bmatrix}^T.$$

The implemented EKF state estimation is outlined in Algorithm 3, in a generic formulation, such that $\mathbf{x}_t \in \mathbb{R}^{n+1}$ and $\mathbf{y}_t \in \mathbb{R}^m$. The process noise is given by $\mathbf{q}_t \sim \mathcal{N}(\mathbf{0}, \mathbf{Q}_t)$; the measurement noise is given by $\mathbf{r}_t \sim \mathcal{N}(\mathbf{0}, \mathbf{R}_t)$; and the prior distribution is $\mathbf{x}_0 \sim \mathcal{N}(\mathbf{0}, \mathbf{P}_0)$, see Appendix B for the parameters. This algorithm is applied to Eq. (4.19) to obtain $\hat{\mathbf{x}}_{t|t}^{veh}$.

Algorithm 3: EKF/KF state estimation

```

if EKF algorithm then // initialization
    |  $\mathbf{x}_0 = [\mathbf{0}_{1 \times n} \ 1]^T$ ;
    |  $\mathbf{P}_0 = (\mathbf{I}_{n+1 \times n+1})T_s$ ;
else
    |  $\mathbf{x}_0 = \mathbf{0}_{n \times 1}$ ;
    |  $\mathbf{P}_0 = (\mathbf{I}_{n \times n})T_s$ ;
end
while connected to the CAN signals do
    |  $\hat{\mathbf{x}}_{t|t+1}^- = \mathbf{F}\hat{\mathbf{x}}_{t|t} + \mathbf{G}\mathbf{u}_t$ ; // state prediction
    |  $\mathbf{P}_{t|t+1}^- = \mathbf{F}\mathbf{P}_{t|t}\mathbf{F}^T + \mathbf{Q}_t$ ; // state variance prediction
    |  $\hat{\mathbf{y}}_{t|t+1} = \mathbf{H}\hat{\mathbf{x}}_{t|t+1}$ ; // output update
    |  $\mathbf{K}_t = \mathbf{P}_{t|t+1}^- \mathbf{H}^T (\mathbf{H}\mathbf{P}_{t|t+1}^- \mathbf{H}^T + \mathbf{R}_t)^{-1}$ ; // kalman gain update
    |  $\hat{\mathbf{x}}_{t|t+1} = \hat{\mathbf{x}}_{t|t+1}^- + \mathbf{K}_t(\mathbf{y}_t - \hat{\mathbf{y}}_{t|t+1})$ ; // state update
    |  $\mathbf{P}_{t|t+1} = (\mathbf{I} - \mathbf{K}_t \mathbf{H}) \mathbf{P}_{t|t+1}^-$ ; // state variance update
    | return( $\hat{\mathbf{x}}_{t|t+1}$ );
end

```

Similarly, the UKF state estimation (Algorithm 4) can also be implemented such that $\mathbf{x}_t \in \mathbb{R}^n$ and $\mathbf{y}_t \in \mathbb{R}^m$. The process noise is given by $\mathbf{q}_t \sim \mathcal{N}(\mathbf{0}, \mathbf{Q}_t)$; the measurement noise is given by $\mathbf{r}_t \sim \mathcal{N}(\mathbf{0}, \mathbf{R}_t)$; and the prior distribution is $\mathbf{x}_0 \sim \mathcal{N}(\mathbf{0}, \mathbf{P}_0)$. The algorithm is directly applicable to Eq. (4.18) for obtaining $\hat{\mathbf{x}}_{t|t}^{veh}$. Irrespective of the estimation method,

4.3. Disturbance estimation

$\hat{F}_{yf,l}$, $\hat{F}_{yf,r}$, $\hat{t}_{pf,l}$, and $\hat{t}_{pf,r}$ are calculated using $\hat{\alpha}_{f,l}$ and $\hat{\alpha}_{f,r}$, given by Eqs. (4.13) and (4.15), respectively. Subsequently, \hat{M}_{rack} is computed using Eq. (4.16).

Algorithm 4: UKF state estimation

```

 $\mathbf{x}_0 = \mathbf{0}_{n \times 1}$ ; // initialization
 $\mathbf{P}_0 = (\mathbf{I}_{n \times n})T_s$ ; // initialization
while connected to the CAN signals do
     $\alpha = 0.05$ ;
     $\kappa = 0$ ;
     $\beta = 2$ ;
     $\lambda = \alpha^2(n + \kappa) - n$ ;
     $W_0^{(m)} = \lambda / (n + \lambda)$ ;
     $W_0^{(c)} = W_0^{(m)} + (1 - \alpha^2 + \beta)$ ;
     $\chi_{t|t}^{(0)} = \hat{\mathbf{x}}_{t|t}$ ; // sigma point
    foreach  $i \in [1, n]$  do
         $\chi_{t|t}^{(i)} \leftarrow \hat{\mathbf{x}}_{t|t} + \sqrt{n + \lambda}(\sqrt{\mathbf{P}_{t|t}})$ ; // sigma points
         $W_i^{(m)} \leftarrow 0.5 / (n + \lambda)$ ;
         $W_i^{(c)} \leftarrow W_i^{(m)}$ ;
    end
    foreach  $i \in [n + 1, 2n]$  do
         $\chi_{t|t}^{(i)} \leftarrow \hat{\mathbf{x}}_{t|t} - \sqrt{n + \lambda}(\sqrt{\mathbf{P}_{t|t}})$ ; // sigma points
         $W_i^{(m)} \leftarrow 0.5 / (n + \lambda)$ ;
         $W_i^{(c)} \leftarrow W_i^{(m)}$ ;
    end
     $\{\hat{\mathbf{x}}_{t|t+1}^-, \mathbf{P}_{t|t+1}^-, \hat{\mathbf{y}}_{t|t+1}, \mathbf{P}_{yy,t|t+1}, \mathbf{P}_{xy,t|t+1}\} = [\ ] \leftarrow \text{initialize};$ 
    for  $i = 0 \rightarrow 2n$  do
         $\hat{\chi}_{t|t+1}^{(i)} = \mathbf{f}(\chi_{t|t}^{(i)}, \mathbf{u}_t)$ ; // transformed state
         $\hat{\mathbf{x}}_{t|t+1}^- = \hat{\mathbf{x}}_{t|t+1}^- + W_i^{(m)} \hat{\chi}_{t|t+1}^{(i)}$ ; // state prediction
         $\mathbf{P}_{t|t+1}^- = \mathbf{P}_{t|t+1}^- + W_i^{(c)} (\hat{\chi}_{t|t+1}^{(i)} - \hat{\mathbf{x}}_{t|t+1}^-)(\hat{\chi}_{t|t+1}^{(i)} - \hat{\mathbf{x}}_{t|t+1}^-)^T$ ;
         $\gamma_{t|t+1}^{(i)} = \mathbf{h}(\hat{\chi}_{t|t+1}^{(i)})$ ; // transformed output
         $\hat{\mathbf{y}}_{t|t+1} = \hat{\mathbf{y}}_{t|t+1} + W_i^{(m)} \gamma_{t|t+1}^{(i)}$ ; // output update
         $\mathbf{P}_{yy,t|t+1} = \mathbf{P}_{yy,t|t+1} + W_i^{(c)} (\gamma_{t|t+1}^{(i)} - \hat{\mathbf{y}}_{t|t+1})(\gamma_{t|t+1}^{(i)} - \hat{\mathbf{y}}_{t|t+1})^T$ ;
         $\mathbf{P}_{xy,t|t+1} = \mathbf{P}_{xy,t|t+1} + W_i^{(c)} (\hat{\chi}_{t|t+1}^{(i)} - \hat{\mathbf{x}}_{t|t+1}^-)(\gamma_{t|t+1}^{(i)} - \hat{\mathbf{y}}_{t|t+1})^T$ ;
    end
     $\mathbf{P}_{t|t+1}^- = \mathbf{P}_{t|t+1}^- + \mathbf{Q}_t$ ; // state variance prediction
     $\mathbf{K}_t = \mathbf{P}_{xy,t|t+1}(\mathbf{P}_{yy,t|t+1} + \mathbf{R}_t)^{-1}$ ; // kalman gain update
     $\hat{\mathbf{x}}_{t|t+1} = \hat{\mathbf{x}}_{t|t+1}^- + \mathbf{K}_t(\mathbf{y}_t - \hat{\mathbf{y}}_{t|t+1})$ ; // state update
     $\mathbf{P}_{t|t+1} = \mathbf{P}_{t|t+1}^- - \mathbf{K}_t \mathbf{P}_{xy,t|t+1}^T$ ; // state variance update
    return( $\hat{\mathbf{x}}_{t|t+1}$ );
end

```

4.3.2 Steering system based observer

In this approach, the steering rack model presented in Section 2.1 is used for the state estimation problem. Basically, the rack force is directly estimated at the environment interaction port. The measured output signals are $x_{rack}(t)$ and $v_{rack}(t)$, or their equivalent, $\theta_p(t)$ and $\omega_p(t)$, respectively; the input signals are $M_{tb}(t)$ and $M_{mot}(t)$. For SbW, the only input signal is $M_{mot}^{rack}(t)$, instead of $M_{mot}(t)$. Based on the motor and pinion moment balance in Eqs. (2.1) and (2.6), the equations of motion can be rewritten as follows:

$$\begin{aligned} J_{mot}\dot{\omega}_{mot}(t) &= -b_{mot}\omega_{mot}(t) - M_{mot,fric}(t) - M_{belt}(t) + M_{mot}(t) \\ J_p\dot{\omega}_p(t) &= -b_p\omega_p(t) - M_{rack}(t) - M_{rack,fric}(t) + M_{tb}(t) + i_{mot}M_{belt}(t) \end{aligned} \quad (4.20)$$

where $M_{belt}(t) = k_{belt}(\omega_{mot}(t) - i_{mot}\omega_p(t)) + c_{belt}(\theta_{mot}(t) - i_{mot}\theta_p(t))$. As stated in Paper D, the Coulomb friction torques are either excluded for linear state estimation (using the KF), or included for non-linear state estimation (using the UKF).

For the KF formulation, $M_{rack,tot} = M_{rack} + M_{rack,fric}$ is considered as a state. Subsequently, a discrete-time state-space is formulated as $\mathbf{x}_{t+1}^{str} = \mathbf{F}\mathbf{x}_t^{str} + \mathbf{G}\mathbf{u}_t^{str} + \mathbf{q}_t^{str}$ and $\mathbf{y}_t^{str} = \mathbf{H}\mathbf{x}_t^{str} + \mathbf{r}_t^{str}$ such that $M_{rack,tot}^{t+1} = M_{rack,tot}^t$ is presumed. The corresponding state, output, and input vectors are $\mathbf{x}_t^{str} = [\theta_{mot} \ \omega_{mot} \ \theta_p \ \omega_p \ M_{rack,tot}]^T$, $\mathbf{y}_t^{str} = [\theta_p \ \omega_p]^T$, and $\mathbf{u}_t^{str} = [M_{tb} - M_{rack,fric} \ M_{mot} - M_{mot,fric}]^T$, respectively, such that M_{tb} can be neglected for SbW. Algorithm 3 is applied to obtain \hat{M}_{rack} . The following Coulomb friction torques are calculated upon discretization using the second-order Taylor–Lie series method and then deducted accordingly:

$$\begin{aligned} M_{mot,fric}^{t+1} &= M_{mot,fric}^t + f_1|\hat{\mathbf{x}}_t, \mathbf{u}_t T_s + \frac{\partial f_1}{\partial \mathbf{x}_{\hat{\mathbf{x}}_t, \mathbf{u}_t}} \dot{\mathbf{x}}_t^{str} \frac{T_s^2}{2} \\ M_{rack,fric}^{t+1} &= M_{rack,fric}^t + f_2|\hat{\mathbf{x}}_t, \mathbf{u}_t T_s + \frac{\partial f_2}{\partial \mathbf{x}_{\hat{\mathbf{x}}_t, \mathbf{u}_t}} \dot{\mathbf{x}}_t^{str} \frac{T_s^2}{2} \end{aligned} \quad (4.21)$$

where

$$\begin{aligned} f_1 &:= \frac{d}{dt}(M_{mot,fric}(t)) = c_{mot,fric} \left(\omega_{mot}(t) - \frac{M_{mot,fric}(t)}{M_{mot,fric}^0} |\omega_{mot}(t)| \right) \quad \text{and} \\ f_2 &:= \frac{d}{dt}(M_{rack,fric}(t)) = c_{rack,fric} \left(\omega_p(t) - \frac{M_{rack,fric}(t)}{M_{rack,fric}^0} |\omega_p(t)| \right) \end{aligned}$$

Moreover, $c_{mot,fric}$ and $c_{rack,fric}$ are the Dahl friction model stiffness values; $M_{mot,fric}^0$ and $M_{rack,fric}^0$ are the peak Coulomb friction torques on their respective inertia.

In the UKF state estimation, the Coulomb friction torque variables in Eq. (4.21) can be substituted to the discrete-time formulation of Eq. (4.20). Hence, it results in

$$\mathbf{x}_{t+1}^{str} = \mathbf{f}(\mathbf{x}_t^{str}, \mathbf{u}_t^{str}) + \mathbf{q}_t^{str} \quad \text{and} \quad \mathbf{y}_t^{str} = \mathbf{h}(\mathbf{x}_t^{str}) + \mathbf{r}_t^{str} \quad (4.22)$$

such that $M_{rack}^{t+1} = M_{rack}^t$ is presumed, $\mathbf{x}_t^{str} = [\theta_{mot} \ \omega_{mot} \ \theta_p \ \omega_p \ M_{mot,fric} \ M_{rack,fric} \ M_{rack}]^T$, $\mathbf{y}_t^{str} = [\theta_p \ \omega_p]^T$, $\mathbf{u}_t^{str} = [M_{tb} \ M_{mot}]^T$ for EPAS, and $\mathbf{u}_t^{str} = M_{mot}^{rack}$ for SbW. Finally, Eq. (4.22) can be solved using Algorithm 4 to compute \hat{M}_{rack} . Paper D provides a more detailed description of different model orders.

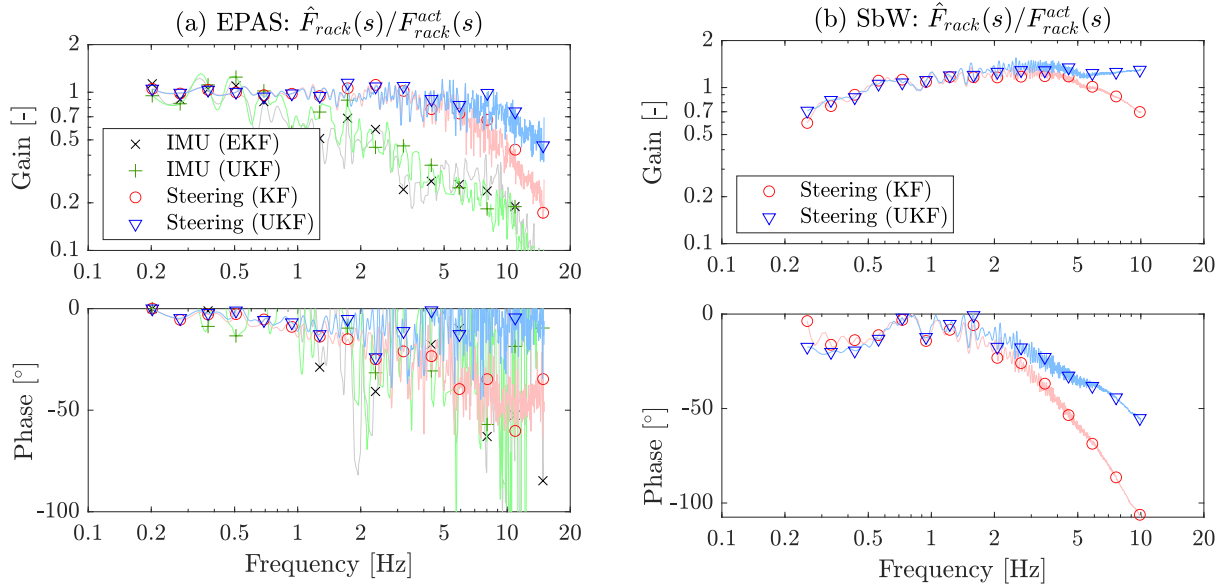


Figure 4.11: Measured rack force observer $\hat{F}_{rack}(s)/F_{rack}^{act}(s)$ FRF for (a) EPAS and (b) SbW.

4.3.3 Evaluation of observers

This section presents a brief comparison of different rack force observers including their estimation algorithm. For EPAS, the results were obtained from a prototype vehicle, whereas a HIL test rig was used for the SbW system. The observer's frequency response plot is shown in Fig. 4.11, also presented in Paper D with a time-based comparison.

In EPAS, the measurement was performed with a sufficient rack force excitation during closed-circuit driving on a winter proving ground. Due to varying road conditions, the measured signals were noisier than usual. The $\hat{F}_{rack}(s)/F_{rack}^{act}(s)$ FRF plot can be seen in Fig. 4.11(a) for an objective comparison among the estimators. Regardless of the algorithm (EKF or UKF), the performance of vehicle motion (or IMU) based approach compared with the steering system based approach is inferior at high frequencies. This is mainly due to the mechanically delayed motion response caused by the vehicle dynamic effects subjected to road disturbance. The secondary reason is the higher sampling time of IMU signals, i.e., 10 ms for a_y and 15 ms for $\dot{\psi}$, when compared with 1 ms for steering system signals. This cumulatively deteriorates the quality of IMU based rack force estimate. Whereas, the performance of steering system based estimators is better. In the non-linear (UKF) estimation, the gain drops at a higher frequency and with a lower phase delay. This is due to the inclusion of the (non-linear) Coulomb friction model within the estimation method, which is a known advantage of the UKF for non-linear state estimation problem [162].

A similar conclusion regarding steering system based observers is valid for SbW, as shown in Fig. 4.11(b). The drop in the FRF gain at low frequencies is caused by the uncompensated friction dynamics of the (test rig) actuator. Again, the UKF for non-linear estimation provides a lower time/phase delay, which is desirable for faster transparency.

An important remark for the UKF: the variance for $M_{rack,fric}$ and $M_{mot,fric}$ is added to \mathbf{Q}_t while keeping the same variance for other states similar to that in the KF. Moreover, \mathbf{Q}_t

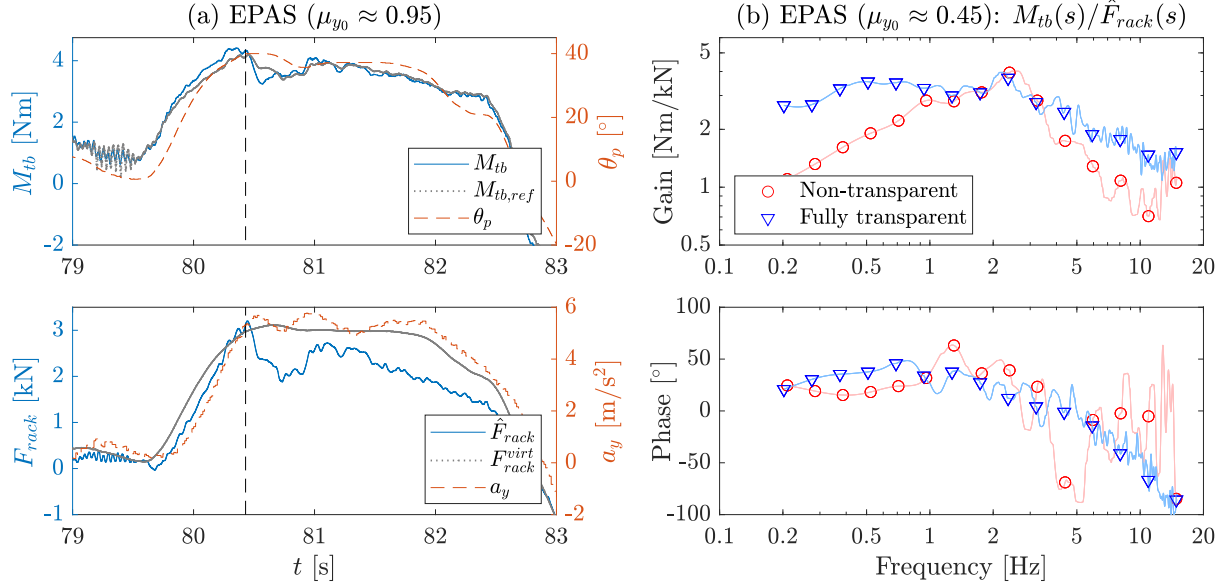


Figure 4.12: (a) A time-based measurement for a fully transparent EPAS setting. (b) Measured $M_{tb}(s)/\hat{F}_{rack}(s)$ FRF response on a surface with low and varying tire-road friction coefficient.

was tuned for a small root mean square error and real-time compatibility at 1 ms.

4.4 Transparency using estimated disturbance

The estimated rack force, \hat{F}_{rack} , or its equivalent, the estimated rack torque, \hat{M}_{rack} , presented in the previous section can be used to achieve the steering feedback transparency. For the upcoming discussion, the following is valid: (a) the steering system based UKF method is selected for \hat{M}_{rack} ; (b) full transparency is applied, implying $\gamma_1 = \gamma_2 = 1$ in Eq. (4.2).

Consider an EPAS example by investigating the non-linear steady state response. As shown in Fig. 4.12(a), at $t = 80.45$ s, \hat{F}_{rack} reaches its peak and then starts decreasing near the maximum lateral tire-road grip, despite maintaining a fairly constant $\theta_p(t)$ until $t \approx 82$ s. An analogous response is observed in the measured pinion torque, $M_{tb}(t)$, because $M_{tb,ref}(t)$ is a function of $\hat{F}_{rack}(t)$ in torque control. Thus, the effect of environmental uncertainty is reflected in the steering feedback. However, this is not true with $F_{rack}^{virt}(t)$, because it is a function of $\theta_p(t)$ and remains relatively constant in the same time window.

For the frequency response analysis, the measured $M_{tb}(s)/\hat{F}_{rack}(s)$ FRF plot is shown in Fig. 4.12(b). This plot is captured from a road surface with sufficient and persistent rack force excitation. The non-transparent setting exhibits a disturbance rejection response. As a result, the torque levels are lower for a given \hat{F}_{rack} value. However, in case of transparency, a higher torque amplitude is achieved because of the estimated rack force/torque feedback to the reference model. Therefore, the proposed concept haptically informs the driver regarding the non-linear steady state tire response and high frequency road disturbance.

A better transparency comparison can be performed in IPG CarMaker simulation because the same rack force excitation input, defined by $F_{rack,ext}$, can be consistently applied without

4.4. Transparency using estimated disturbance

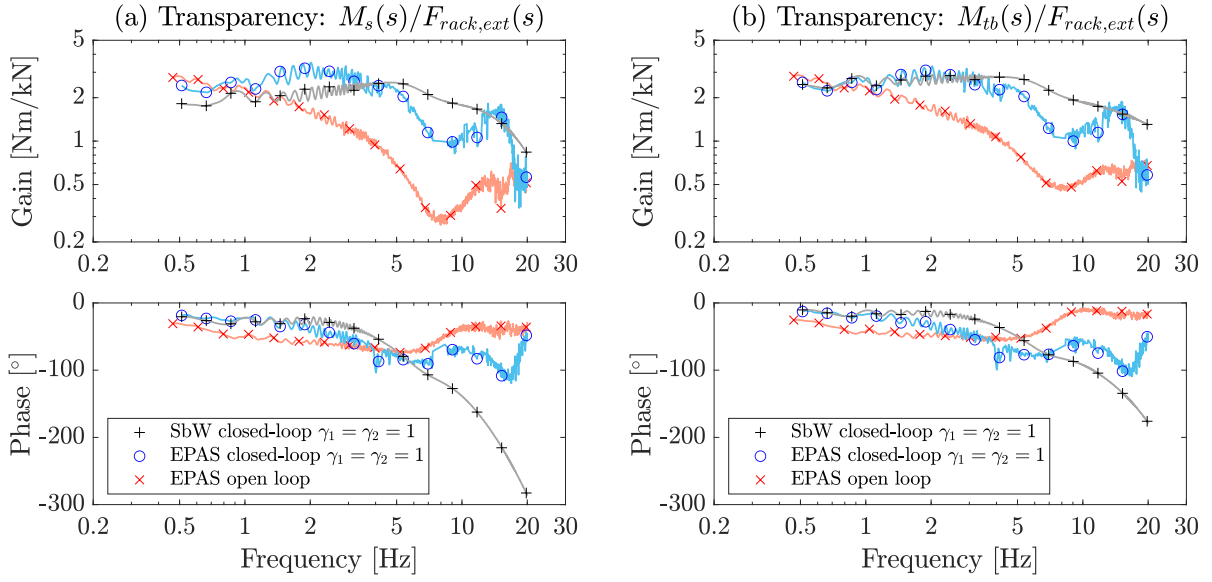


Figure 4.13: Simulated transparency result at 75 km/h in terms of frequency response functions: $M_s(s)/F_{rack,ext}(s)$ and $M_{tb}(s)/F_{rack,ext}(s)$.

any other influencing factors. In reality, this is difficult to achieve due to various reasons, such as varying tire–road interaction dynamics, different driver reactions, and different sampling frequencies of the measured signals in open loop and closed-loop settings.

The problem of attenuated transparency in open loop EPAS was posed earlier in Section 3.2.1 and illustrated in Fig. 3.3. For SbW, the system is already non-transparent. Here, the extent of transparency that can be achieved in closed-loop EPAS and SbW is investigated. For this, a straight-line maneuver was performed with a driver model such that $(\theta_{s,req}, \omega_{s,req}) = (0, 0)$. The rack force excitation was applied with a peak amplitude of 750 N, and the FRF plots, $M_s(s)/F_{rack,ext}(s)$ and $M_{tb}(s)/F_{rack,ext}(s)$, are shown in Fig. 4.13.

The aforementioned figure shows that the transparency of closed-loop EPAS and SbW compared with that of open loop EPAS is considerably less attenuated in the gain response. The phase delay between closed-loop and open loop EPAS is comparable up to 9 Hz; however, beyond this, the phase delay of the former marginally exceeds that of the latter. This is a typical drawback of the closed-loop causality caused by the limited performance of the feedback controller and communication delays. In SbW, the phase delay is even higher due to the mechanical disconnection, higher time delays, and because the response is completely virtual. This aspect must be further improved in the future to achieve faster transparency.

For the SbW measurement, the two-channel DFR bilateral teleoperation scheme was implemented similar to simulation. The measured FFb pinion angle was sent to the SbW-rack position controller such that $\theta_{p2,ref} = \theta_{p1}$, and \hat{F}_{rack} was signaled back to the reference model. The HIL test rig result is shown in Fig. 4.14 illustrating a sine sweep maneuver.

As demonstrated in this section, the driver–environment transparency in closed-loop EPAS and SbW is achieved up to a reasonable extent. Moreover, unlike open loop EPAS, it can be explicitly manipulated. Accordingly, the next step is to compute the optimal transparency (γ_1^*, γ_2^*) , given the non-transparent setting and environmental uncertainty.

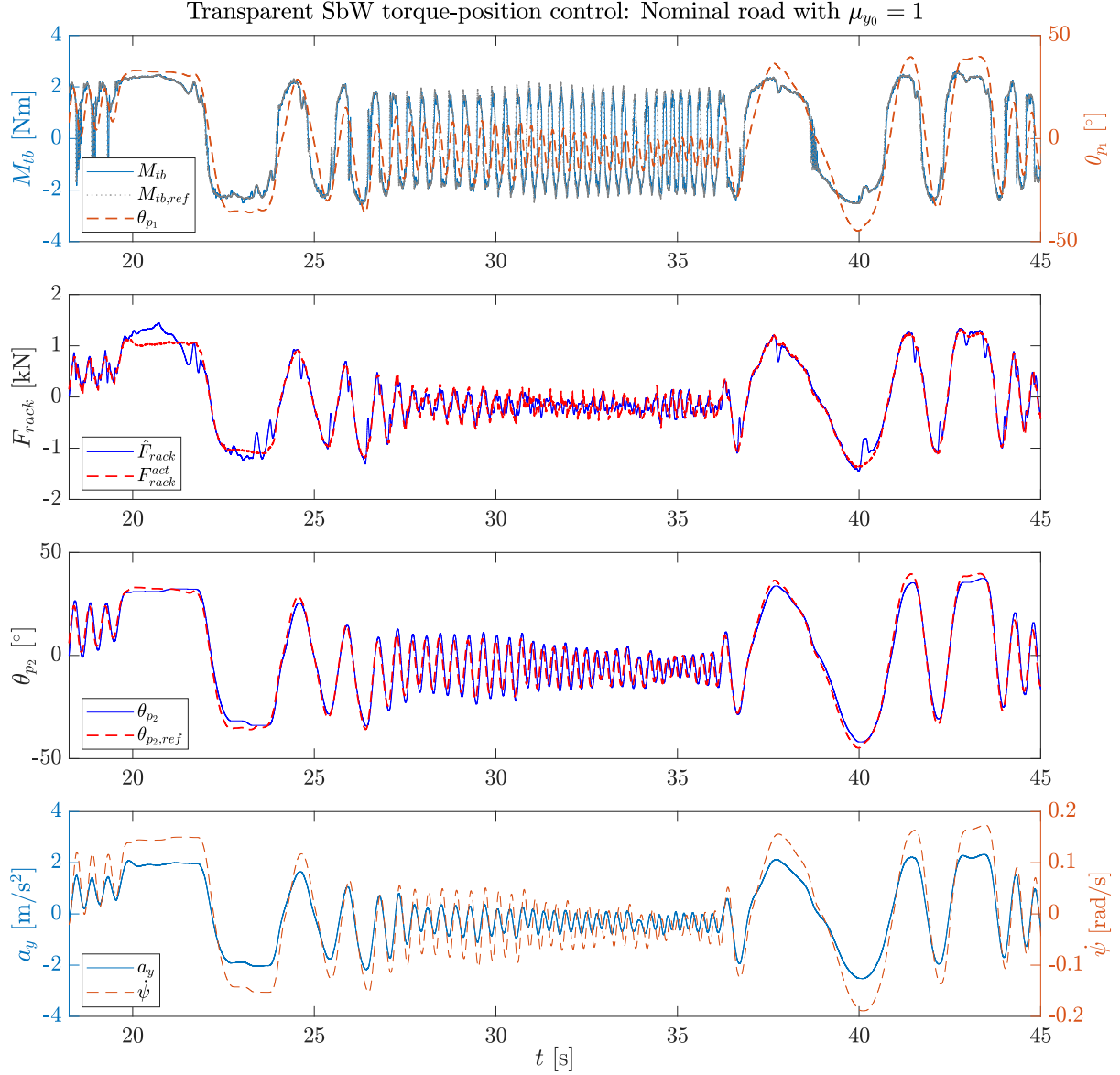


Figure 4.14: A transparent SbW torque-position control response measured on HIL test rig under nominal road conditions ($\mu_{y0} = 1$) and $v_x = 45$ km/h. The time-based signals are: FFb pinion torque, FFb pinion angle (top), rack force (second from top), pinion angle on rack actuator (third from top), lateral acceleration, and yaw rate (bottom).

4.5 Transparency control

In this section, an MPC formulation is proposed to control the driver–environment transparency. Two static (boundary) conditions were previously discussed: $\gamma_1 = \gamma_2 = 0$ for non-transparency (Section 4.2.2) and $\gamma_1 = \gamma_2 = 1$ for transparency (Section 4.4). Here, the goal is to adapt transparency to provide haptic information to the driver, in case the vehicle encounters environmental uncertainty, even if the initial condition is non-transparent. This topic has not been covered by any of the appended papers.

Recall the *transparency control* block shown in Fig. 4.1 and 4.3. The upcoming discussion is based on Eq. (4.2) such that transparency gains (γ_1, γ_2) are treated as decision variables for the optimization problem, as suggested in [163].

4.5.1 Motion based concept

A straightforward means to decide γ_1 and γ_2 is to use an empirical relationship based on the deviation between M_{rack}^{virt} and \hat{M}_{rack} ; however, this approach is cumbersome. As an alternative, a model-based approach with an optimal solution based on the deviation between the virtual and estimated vehicle motion states is presented and applied.

Under the influence of environmental uncertainty, vehicle motion differs between open loop and non-transparent closed-loop control settings. The reason is the disturbance rejection property of the latter such that the given initial condition in terms of either reference torque or reference position is maintained by the controller. Consequently, the vehicle follows different trajectories in the aforementioned control settings. Accordingly, the deviation in vehicle motion is exploited for the transparency control logic.

To explain the problem, consider a hypothetical driving scenario. A simulation example is presented to highlight the difference between non-transparent and transparent haptic feedback setting as well as related vehicle motion variables. The straight-line maneuver begins with driving at 75 km/h on a surface with low lateral tire–road friction ($\mu_{y0} = 0.3$). At $t = 1$ s, the driver step steers to maintain a constant input torque of 2.75 Nm, as shown in Fig. 4.15. The environmental uncertainty occurs at $t = 4.25$ s, i.e., a step change in the peak road friction coefficient such that $\mu_{y0} = 1$.

At this point, the *non-transparent* response is observed. The closed-loop controller attempts to maintain the (virtual) torque–angle equilibrium, despite the external disturbance. This produces a certain vehicle trajectory, as shown in the Global X/Y plot and by the motion variables (i.e., a_y , v_y , and $\dot{\psi}$). A similar response is shown for the *transparent* setting. When driving on a slippery surface, the driver initially aims to achieve the required torque. However, because of the transparency and given road condition, the driver is unable to accomplish this and continues to increase the steering angle in search of the required torque. As the road uncertainty appears, the pinion angle straightaway decreases to maintain the requested input torque, i.e., 2.75 Nm. Consequently, the vehicle motion significantly differs from the non-transparent setting, and the vehicle follows a different path.

The above example is the motivation behind the proposed concept of manipulating transparency using vehicle motion states, given that the initial condition is non-transparent. Thereby, a finite-horizon optimal control problem (OCP) is formulated.

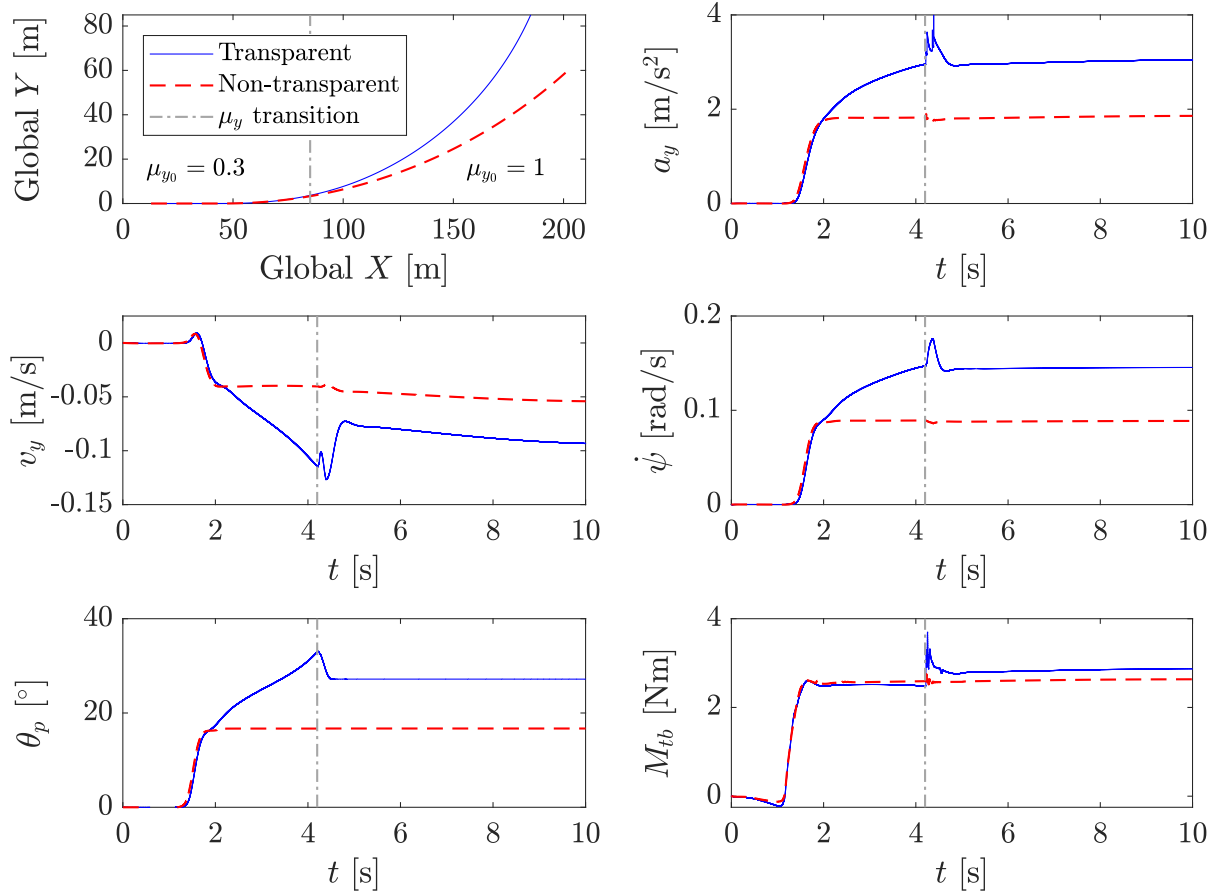


Figure 4.15: A step steer torque maneuver at $v_x = 75$ km/h on a surface with transitioning peak tire-road friction coefficient from 0.3 to 1: Global X/Y plot (top left) and time-based response for lateral acceleration (top right), lateral vehicle speed (middle left), yaw rate (middle right), pinion angle (bottom left), and pinion torque (bottom right). The change in the peak tire-road friction occurs at $t = 4.25$ s for two closed-loop EPAS configurations, i.e., non-transparent and fully transparent.

4.5.2 MPC algorithm

The central objective is to formulate a convex QP optimization problem using decision variables as the control signal such that the closed-loop system is the nominal plant model and non-transparency is the initial condition. This includes a closed-loop controller and a causal combination of models (Chapter 2), i.e., steering, vehicle, tire, and driver. The driver model may be excluded, depending on how the problem is framed.

Consider the single-track vehicle model discussed in Section 2.2 and the steering rack model (Section 2.1.1) in Eq. (4.23). The lateral tire forces, F_{yf} and F_{yr} , and the front axle tire pneumatic trail, t_{pf} , are given by Eqs. (4.13) and (4.15), respectively. The vehicle model, defined by \mathbf{f}_{veh} , has an additional input channel, $\Delta F_{yf}(t)$, to cause front axle tire-road interaction uncertainty.

$$\begin{aligned} \mathbf{f}_{veh} : \begin{cases} m\dot{v}_y(t) = -mv_x\dot{\psi}(t) + F_{yf}(t) + F_{yr}(t) + \Delta F_{yf}(t) \\ J_z\ddot{\psi}(t) = l_f(F_{yf}(t) + \Delta F_{yf}(t)) - l_r F_{yr}(t) \\ M_{rack}(t) = (t_{pf}(t) + t_m)(F_{yf}(t) + \Delta F_{yf}(t))/i_{str} \end{cases} \\ \mathbf{f}_{str} : \begin{cases} J_p\dot{\omega}_p(t) = -b_p\omega_p(t) - M_{rack}(t) + M_{tb}(t) + i_{mot}M_{mot}(t) \end{cases} \end{aligned} \quad (4.23)$$

The closed-loop is formulated using the torque control law in Eq. (3.14); note that a similar result can also be achieved using position control. Equation (4.2) is used for transparency through $M_{rack}^{ref}(t)$; hence, the resulting motor torque is defined as follows:

$$M_{mot}(t) = -(\alpha_1 e_M(t) + \alpha_0 \int_0^t e_M(\tau) d\tau) \quad (4.24)$$

where

$$\begin{aligned} e_M(t) &= J_{ref}\dot{\omega}_p(t) + b_{ref}\omega_p(t) + M_{rack}^{ref}(t) - M_{tb}(t) \\ M_{rack}^{ref}(t) &= (1 - \gamma_1(t))M_{rack}^{virt}(t) + \gamma_2(t)\hat{M}_{rack}(t) \\ M_{rack}^{virt}(t) &= c_{ref}\theta_p(t) \end{aligned}$$

such that $0 \leq (\gamma_1(t), \gamma_2(t)) \leq 1$, $\gamma_1(t) = \gamma_2(t)$ and $\gamma_1(0) = \gamma_2(0) = 0$. Some assumptions are taken for simplicity. (a) The steering wheel's equation of motion is excluded; therefore, M_{tb} is assumed as the driver input. (b) The reference model is linear and has static parameters. (c) The rack force observer (Section 4.3) is ideal, thus implying $\hat{M}_{rack}(t) = M_{rack}(t)$.

For the non-linear closed-loop plant model given by Eqs. (4.23) and (4.24) in continuous-time, the state vector is $x(t) = [v_y \ \dot{\psi} \ \alpha_f \ \alpha_r \ \theta_p \ \omega_p \ \zeta]^T$ such that $\dot{\zeta}(t) = [\alpha_f \ \theta_p \ \gamma_1 \ \gamma_2 \ M_{tb}]^T$ due to integral action of the control law. Subsequently, the following state-space can be obtained upon discretization and linearization

$$\begin{aligned} x(t+1) &= Ax(t) + B_d d(t) + Bu(t) \\ y(t) &= Cx(t) + C_d d(t) \end{aligned} \quad (4.25)$$

where $y(t) = [\dot{\psi} \ a_y \ \theta_p]^T$, $d(t) = [\Delta F_{yf} \ M_{tb}]^T$, and $u(t) = [\gamma_1 \ \gamma_2]^T$. To solve the given linear MPC problem, two sequential steps are implemented: setpoint tracking and minimization of the deviation variables, as shown in Fig. 4.16. Moreover, the estimated disturbance, $\hat{d}(t)$, and vehicle state, $\hat{x}(t)$, are required during optimization. Each aspect is briefly discussed next based on the general propositions from [164, 165].

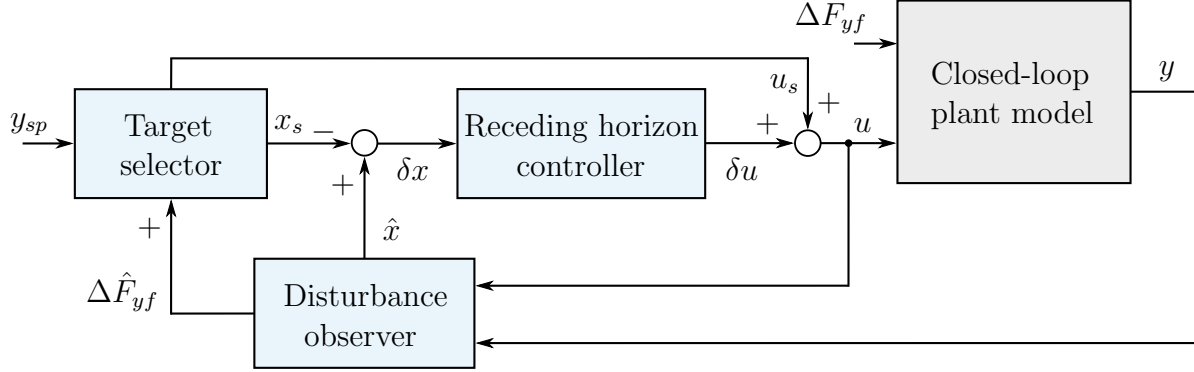


Figure 4.16: Typical MPC formulation with target selector, disturbance observer, and receding horizon controller.

Disturbance observer

The effect of steady state disturbance on the decision variable can be explicitly included upon its estimation and feedback to the target selector, as shown in Fig. 4.16. Here, the unknown disturbance input is ΔF_{yf} . A typical solution is to form an augmented system by assuming $d(t+1) = d(t)$ such that the system remains detectable with the given B_d and C_d . A discrete Kalman Filter can be iterated over the prediction horizon with the stationary Kalman prediction covariance as the initial condition. The Kalman Filter gain, L_e , is chosen to stabilize the observer dynamics. A long horizon implies that L_e converges to its stationary solution given by the filtering algebraic Riccati equation.

In the steering feedback reference model (Fig. 4.1 and 4.3), this observer is represented by the *motion state estimator* block. Because the rack torque, \hat{M}_{rack} , is well estimated (Section 4.3.2) based on the steering system signals, it can be used as a known quantity for the IMU based vehicle state estimator. The state estimation problem can be solved in the same manner as that presented in Section 4.3.1, utilizing the vehicle and tire models including an additional measured variable $\hat{M}_{rack}(t)$; it is appended along with $\dot{\psi}(t)$ and $a_y(t)$ through Eq. (4.16). Therefore, the estimated vehicle states $\hat{x}_{veh}(t)$ are here further improved as compared with the previously discussed estimator in Section 4.3.1. Consequently, $\Delta \hat{F}_{yf}(t)$ is deduced using Eq. (4.13), as follows.

$$\Delta \hat{F}_{yf}(t) = \hat{F}_{yf}(t) - F_{yf}^{virt}(t) = f(\hat{\alpha}_f(t)) - f(\alpha_f^{virt}(t)) \quad (4.26)$$

Target selector

The steady state target problem is solved for the stationary state and input trajectories, i.e., x_s and u_s , respectively. Let y_{sp} be the output reference/setpoint, which should be tracked. Given ΔF_{yf} and system dynamics, x_s and u_s are computed from the optimization problem:

$$\begin{aligned} & \underset{x_s, u_s}{\text{minimize}} && ||C x_s + C_{d1} \Delta \hat{F}_{yf} - y_{sp}||_{Q_y}^2 \\ & \text{subject to} && \begin{bmatrix} I - A & -B \\ 0 & H_u \end{bmatrix} \begin{bmatrix} x_s \\ u_s \end{bmatrix} = \begin{bmatrix} B_{d1} \Delta \hat{F}_{yf} \\ 0 \end{bmatrix} \\ & && 0 \leq u_s \leq 1 \end{aligned} \quad (4.27)$$

where $Q_y = Q_y^T \succeq 0$ is the output penalty, and $H_u = [1 \ -1]$ defines the constraint $\gamma_{1,s} = \gamma_{2,s}$. The inequality constraint ensures that decision variables are bounded between 0 and 1. Note that M_{tb} is excluded from the disturbance, because the goal is to manipulate transparency with ΔF_{yf} , given a certain M_{tb} value.

Receding horizon controller

Given the steady state reference x_s from the *target selector*, an MPC should be applied to the deviation variables, i.e., $\delta x(k) = \hat{x}(k) - x_s$. The aim is to find an optimal control signal, $\delta u^*(k)$, to bring the state trajectory to the equilibrium point, $\delta x_e = 0$, and track the output setpoint. For a general finite-horizon OCP, the cost function is

$$\begin{aligned} V_N(\delta x_0, \delta \mathbf{u}) &= \sum_{k=0}^{N-1} (\|x(k) - x_s\|_Q^2 + \|u(k) - u_s\|_R^2) + \|x(N) - x_s\|_{P_f}^2 \\ &= \sum_{k=0}^{N-1} l(\delta x(k), \delta u(k)) + \|x(N) - x_s\|_{P_f}^2 \end{aligned} \quad (4.28)$$

where $Q = Q^T \succeq 0$, $P_f = P_f^T \succeq 0$, and $R = R^T \succ 0$ are the state, terminal state, and input penalties, respectively. $l(\delta x(k), \delta u(k))$ and N are the stage cost and prediction horizon. Q , P_f , and R should be normalized with respect to the operating range of the corresponding variable, and then weighed accordingly for a *zero* steady state offset in θ_p variable [164].

Using the cost function in Eq. (4.28), the optimization problem in Eq. (4.29) can be solved for the optimal control sequence. Hence, the applied input at each sampling instant is given by the first control action, i.e., $\delta u(t) = \delta u^*(0)$. The constraints follow the linear state model of Eq. (4.23) and ensure $\delta \gamma_1(k) = \delta \gamma_2(k)$ such that $\mathbf{u}^*(k) \in [0, 1]$.

$$\begin{aligned} &\underset{\delta \mathbf{u}}{\text{minimize}} && V_N(\delta x_0, \delta \mathbf{u}) \\ &\text{subject to} && \delta x_0 = \delta x(0), \ \delta x(N) \in \mathcal{X}_f \\ & && \left. \begin{aligned} \delta x(k+1) &= A\delta x(k) + B\delta u(k) \\ H_u \delta u(k) &= 0 \\ \delta u(k) &\leq 1 - u_s \\ \delta u(k) &\geq -u_s \end{aligned} \right\} \text{ for } k = 0, \dots, N-1 \end{aligned} \quad (4.29)$$

A terminal state constraint is also added using a set \mathcal{X}_f as origin. However, this aspect requires a thorough and further investigation for MPC stability, because not all initial states (δx_0) can provide a *feasible* solution. Therefore, a sufficiently long horizon is chosen to ensure feasibility, and the question on how to compute a proper set \mathcal{X}_f for recursive feasibility is kept out of context.

Output setpoint

The reference output, y_{sp} , can be computed as a function of $\Delta \hat{F}_{yf}$ using Eqs. (3.6) and (4.23) for the open loop setting and generating the required motion variables. If the disturbance is applied during a steady state maneuver at an offset position, i.e., $x_0 = x(0) \neq 0$, the corresponding y_{sp} value must also be adjusted using the steady state \hat{M}_{rack} value.

4.5.3 Examples of optimization based transparency

The *transparency control* logic based on the model predictive control framework is summarized in Algorithm 5, where $\text{TS}(\hat{d}, y_{sp})$ and $\text{RHC}(\delta x_0)$ correspond to the optimization problems in Eqs. (4.27) and (4.29), respectively, and solved at $\delta x_0 = \delta x(0)$. Two examples illustrating optimization based transparency are presented using this MPC algorithm for different driving scenarios.

In the first test case, different vehicle configurations are subjected to a step environmental or road disturbance of 1 kN in ΔF_{yf} at $t = 0.1$ s (Fig. 4.17). With no driver input, the non-transparent closed-loop setting aims to maintain the steering system's equilibrium or initial condition, i.e., $\theta_p = 0$ rad, regardless of the disturbance. Consequently, the system has a non-zero rack force; hence, the vehicle motion exhibits a lateral deviation and the corresponding motion variables (v_y , $\dot{\psi}$, and a_y) have a steady state response. In contrast, an open loop vehicle follows a straight-line path due to the zero steady state rack force. A deflected angular position occurs and consequently becomes responsible for generating the counteracting front axle lateral force; thus, causing minimal lateral deviation.

Upon implementing the proposed MPC transparency algorithm, the closed-loop steering controlled vehicle emulates the open loop behavior. The change in transparency gains or decision variables (γ_1 , γ_2) can be seen in Fig. 4.17, given $\gamma_1 = \gamma_2 = 0$ as the initial condition before the uncertainty. Evidently, some amount of lateral deviation occurs during the control actuation until the steady state value is attained; however, this is mitigated to a significant extent compared with that of the non-transparent setting. For the MPC problem, the prediction and the control horizons were chosen as $N = 30$ with a sampling time of 1 ms.

Algorithm 5: MPC transparency algorithm

```

 $t = 0$ ; // initialization
 $x_0 = x(0)$ ; // initialization
while  $x_0 \in \mathbb{X}$  do
     $x_s(t), u_s(t) \leftarrow \text{TS}(\hat{d}, y_{sp})$ ; // steady state reference optimization
     $\delta \mathbf{x}^*(t), \delta \mathbf{u}^*(t) \leftarrow \text{RHC}(\delta x_0)$ ; // deviation variable optimization
     $u^*(t) = u_s(t) + \delta u^*(t)$ ;
    apply  $\gamma_1^*(t), \gamma_2^*(t)$ ;
     $t \leftarrow t + 1$ ;
     $x_0 \leftarrow x(t)$ ;
end

```

The second test scenario considers the driver negotiating a steady state corner and following a certain trajectory, as shown in Fig. 4.18. Environmental uncertainty occurs at $t = 4$ s and lasts until $t = 7$ s; it occurs in terms of ΔF_{yf} , which could be interpreted as an increase in the front axle lateral tire force grip (or equivalent higher operating lateral tire-road friction). To follow a desired motion trajectory, that is quantified in terms of F_{rack} , v_y , $\dot{\psi}$, and a_y , the disturbance should not be attenuated in the steering system such that the driver model adjusts the pinion angle to maintain the same course. This is actually what occurs in the state-of-the-art open loop configuration. However, in the non-transparent

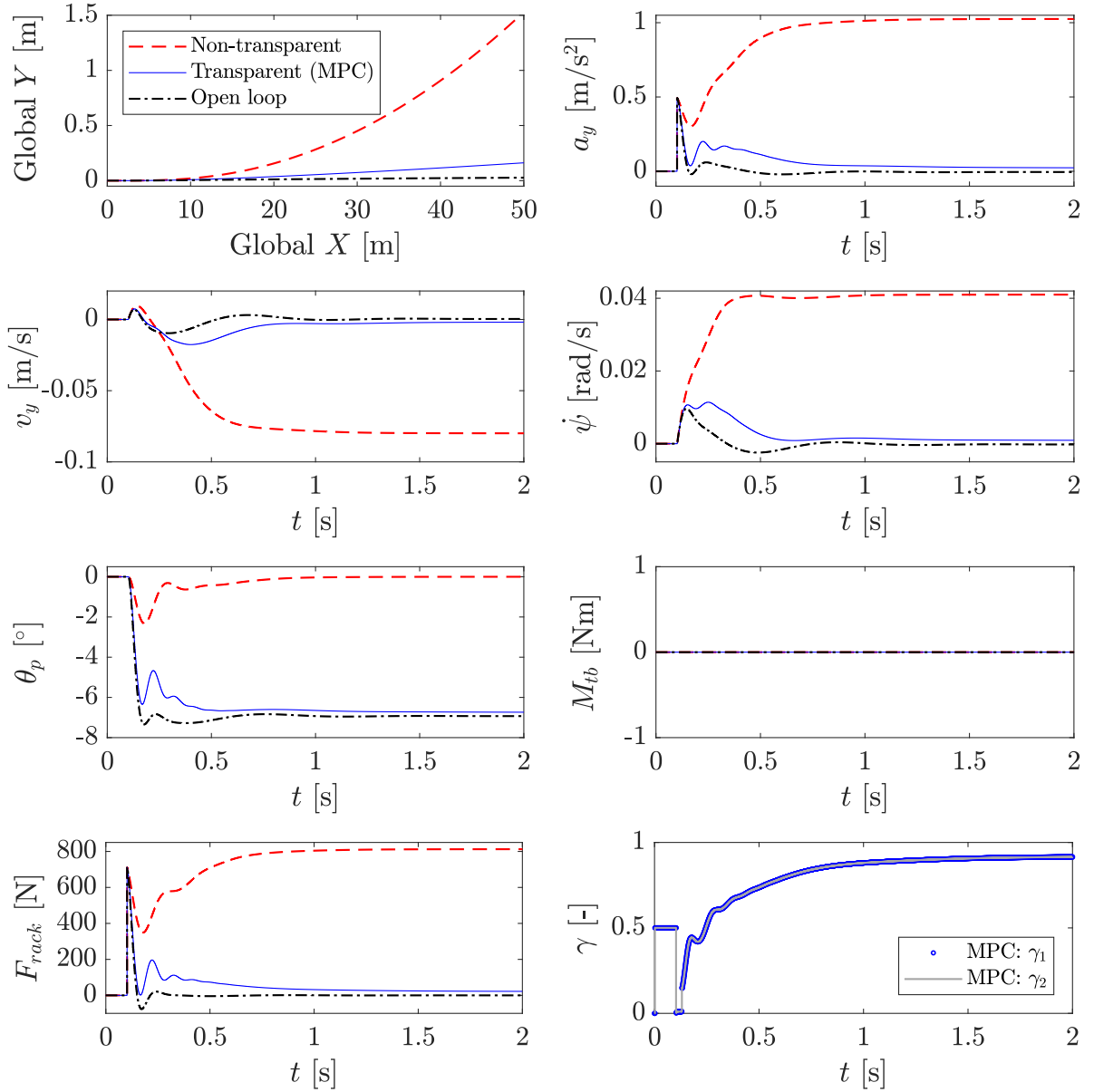


Figure 4.17: 1 kN environmental step disturbance in ΔF_{yf} at $v_x = 90$ km/h: Global X/Y plot (top left) and time-based responses for lateral acceleration (top right), lateral vehicle speed (second row, left), yaw rate (second row, right), pinion angle (third row, left), pinion torque (third row, right), steering rack force (bottom left), and transparency gains or decision variables (bottom right). The disturbance occurs at $t = 0.1$ s for three EPAS configurations, i.e., non-transparent closed-loop, transparent (MPC based) closed-loop, and open loop systems.

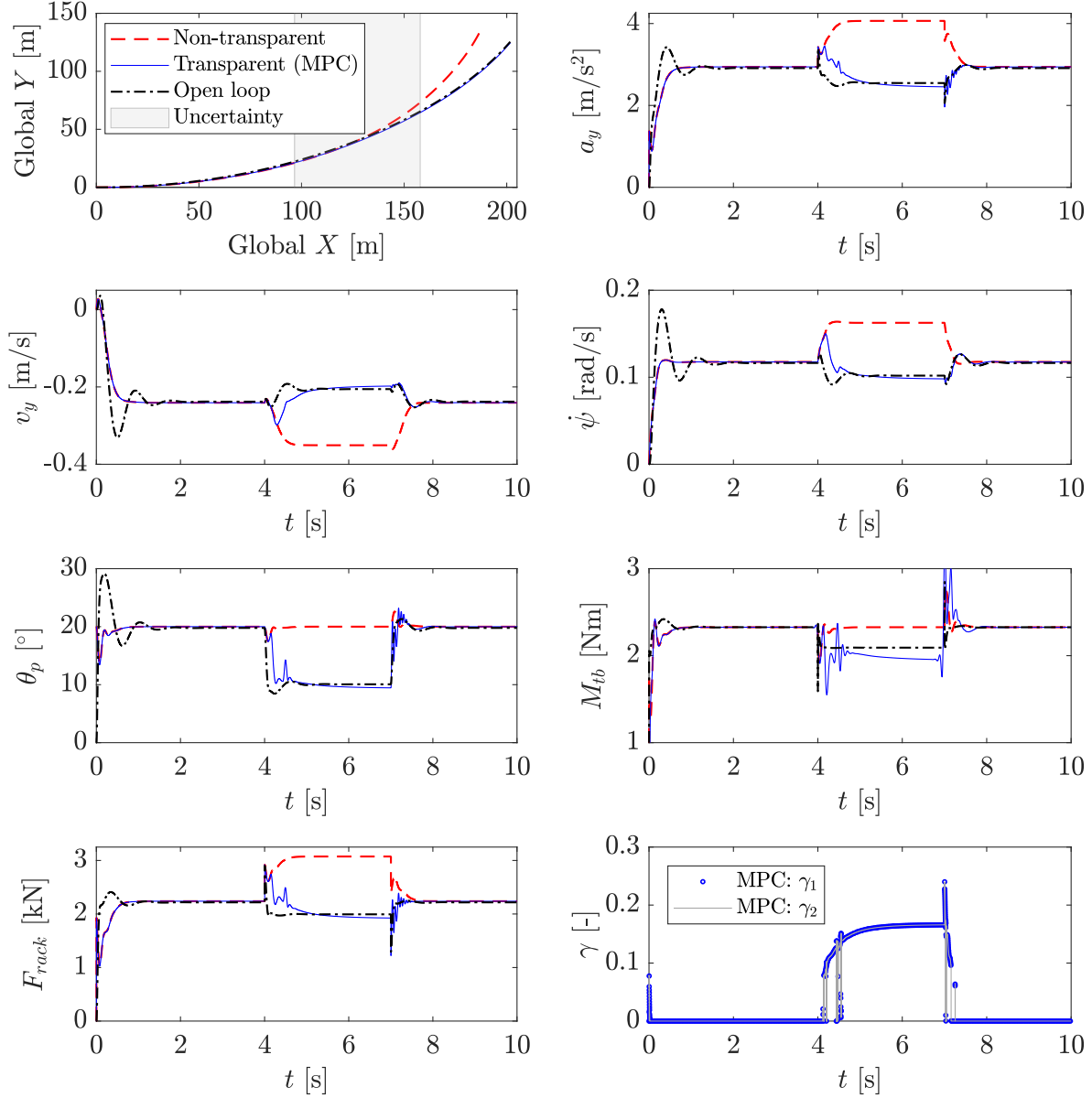


Figure 4.18: 1 kN environmental step disturbance in ΔF_{yf} at $v_x = 90$ km/h: Global X/Y plot (top left) and time-based responses for lateral acceleration (top right), lateral vehicle speed (second row, left), yaw rate (second row, right), pinion angle (third row, left), pinion torque (third row, right), steering rack force (bottom left), and transparency gains or decision variables (bottom right). The disturbance occurs between $t = 4$ s and $t = 7$ s for three EPAS configurations, i.e., non-transparent closed-loop, transparent (MPC based) closed-loop, and open loop systems.

closed-loop setting, road disturbances are attenuated, and the given initial condition in $\theta_p(t)$ and $M_{tb}(t)$ is maintained; in control theory, this is commonly known as *disturbance rejection*. As a result, the vehicle motion differs as the environment varies, because the controller attempts to maintain the same angular position shown in Fig. 4.18. For the stated uncertainty, the non-transparent vehicle exhibits a less understeered response due to the higher steering rack force caused by the higher front axle lateral tire force grip.

For the MPC based transparent setting, the environmental disturbance is reflected to the steering system by increasing γ_1 and γ_2 . Consequently, the driver model reduces the pinion torque and pinion angle to follow the desired course, similar to the open loop configuration. Hence, the vehicle motion variables exhibit a similar steady state response (before, during and after the uncertain road condition) in open loop and closed-loop transparent settings. This demonstrates the effectiveness of the proposed approach for manipulating the haptic feedback transparency based on motion variables subjected to environmental uncertainty and given non-transparency as the initial condition.

4.6 Summary

The control architecture of the steering feedback reference model is proposed in this chapter to answer the second research question (Section 1.2). Both torque and position control causalities are covered, because the former requires an impedance function and the latter, an admittance function. For virtual haptic sensations, a steering rack force model is developed for non-transparency. This model generates the corresponding reference variable as a function of virtual environment dynamics. In the next step, the real environment interaction or actual rack force is estimated using different principles based on available measured signals. The best available estimated rack force signal is then selected and further utilized in the reference model for transparency.

Lastly, an MPC based algorithm is proposed to compute optimal transparency, primarily as a function of deviation in vehicle motion states. The presented algorithm haptically informs the driver regarding the change in environment interaction dynamics, even if the initial condition is non-transparent.

5 Interfacing active safety functions

This chapter exclusively focuses on the third research question (Section 1.2), which pertains to interfacing the steering related active safety functions with the haptic feedback controller. It includes interventions from different functions, such as for shared steering control, ADAS and ADS. Two types of active safety functions are mainly considered: driver haptic support and vehicle motion control. The two are responsible for assisting the driver to drive safely and efficiently, as stated in [100]. Moreover, they control the lateral vehicle positioning on the road for safety and performance reasons (Section 1.1.3).

First, a brief overview of a common approach for realizing these functions in open loop control is discussed. It is assumed that the external request variable from these functions is already known. The question is, how can these interventions be realized in closed-loop control for EPAS and SbW-FFb without quantifying what exactly has to be achieved?

5.1 Open loop control: Motor torque overlay

In typical EPAS systems, (lateral) vehicle motion control functions request external pinion/steering angular position or velocity for a highly or fully ADS, lane keeping assistance/aid, pilot assist, automatic parking, etc. [125, 126, 154, 159]. In contrast, driver haptic support functions can request either an external pinion torque or a pinion angle, depending on the design concept, e.g., driver steer recommendation feature and drifting assistance at the handling limit [100]. These higher level active safety requests require a suitable lower level (or feedback) controller for actuating the steering system and to follow the external request. For example, a position controller for vehicle motion control functions and a torque controller for haptic support functions are required. Therefore, the final requested variable is the motor torque, given by $M_{mot,5}(t)$ in Eq. (3.6) for EPAS; a similar formulation for SbW-FFb is also required. In principle, the different functions with their respective controllers are arbitrated (or summed) at the actuator level. This implies a supplementary motor torque request variable (say $M_{mot,ext}$ in Fig. 3.2 and Fig. 3.5) with the open loop steering feedback control law; this leads to the motor torque overlay.

With the given open loop dynamics in Eq (3.7), the external motor torque request, $M_{mot,ext}(t)$, can be added to represent interventions from active safety functions. For a theoretical interpretation, the corresponding expression in Eq. (5.1) can be resolved into a linear second-order differential equation. In this case, a certain environment load is assumed, say a linear spring such that $M_{rack}(t) = c_p \theta_p(t)$, and without a driver (i.e., $M_{tb} \approx 0$ Nm); moreover, the Coulomb friction torque is neglected.

$$\begin{aligned} J_{p,eff} \dot{\omega}_p(t) &= -b_{p,eff} \omega_p(t) - M_{rack}(t) + K'_{assist} M_{tb}(t) + i_{mot} M_{mot,ext}(t) \\ &= -b_{p,eff} \omega_p(t) - c_p \theta_p(t) + i_{mot} M_{mot,ext}(t) \end{aligned} \quad (5.1)$$

The resulting frequency response function, $\theta_p(s)/M_{mot,ext}(s)$, demonstrates that the vehicle can be steered by applying an excitation to the $M_{mot,ext}$ channel, in particular, at low frequencies to follow the vehicle motion control requests, for example, although the steering

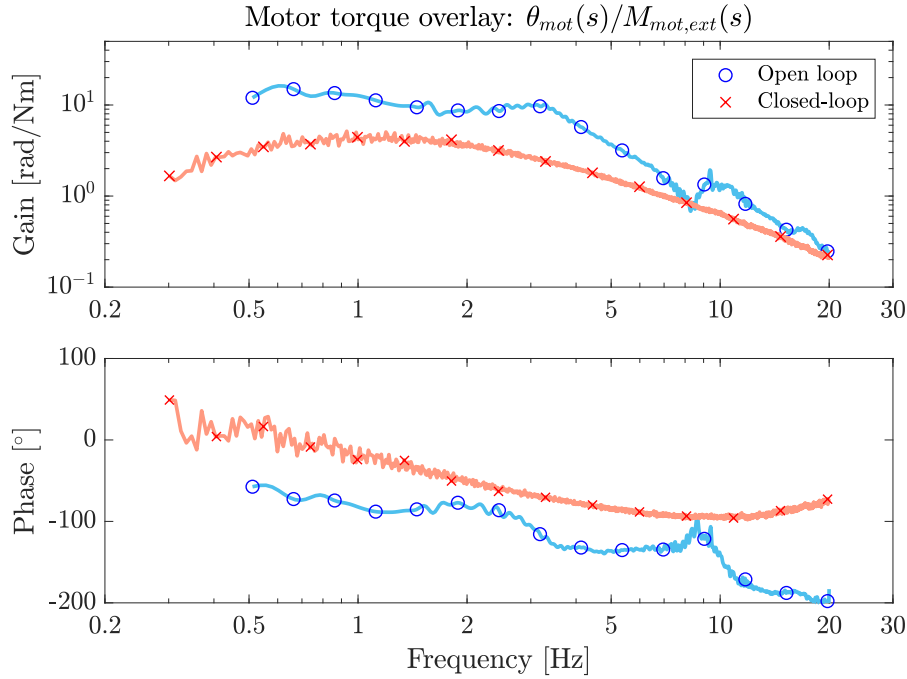


Figure 5.1: A measured frequency response plot of $\theta_{mot}(s)/M_{mot,ext}(s)$ from an EPAS system in an open loop and a closed-loop setting.

response depends on $J_{p,eff}$, $b_{p,eff}$, and c_p . A frequency response example is illustrated in Fig. 5.1 based on an experiment conducted on an EPAS vehicle, where $\theta_{mot} = \theta_p i_{mot}$; the open loop response is similar to a typical multi-DOF system. Subsequently, the obvious choice is to have a motor torque overlay in open loop control. Now the question is, what would happen in the case of closed-loop control with a similar architecture?

5.2 Closed-loop control

The use of the aforementioned motor torque overlay in a closed-loop (non-transparent) setting, regardless of the system and control method, attenuates the external motor torque excitation, particularly at low frequencies. The result, shown in Fig. 5.1, is similar to attenuation of the actual environment interaction discussed in Section 4.4 and illustrated in Fig. 4.12(b). This can be attributed to the disturbance rejection caused by the controller's integral state. The closed-loop response is subsequently similar to that of a band-pass filter such that the low frequency disturbances are suppressed. Accordingly, the phase angle of $\theta_{mot}(s)/M_{mot,ext}(s)$ FRF should be 90° at steady state. Nevertheless, this is the shortcoming of realizing a motor torque overlay with the existing interface between the closed-loop steering feedback controller and active safety functions; the two functionalities are consistently in conflict.

Let $\theta_{p,ext}$ and $M_{tb,ext}$ be the requesting variables from vehicle motion control and haptic support functions. Based on the request signals, a direct approach for realizing the foregoing in closed-loop control is proposed, as shown in Fig. 5.2(a) and 5.2(b) for torque and position

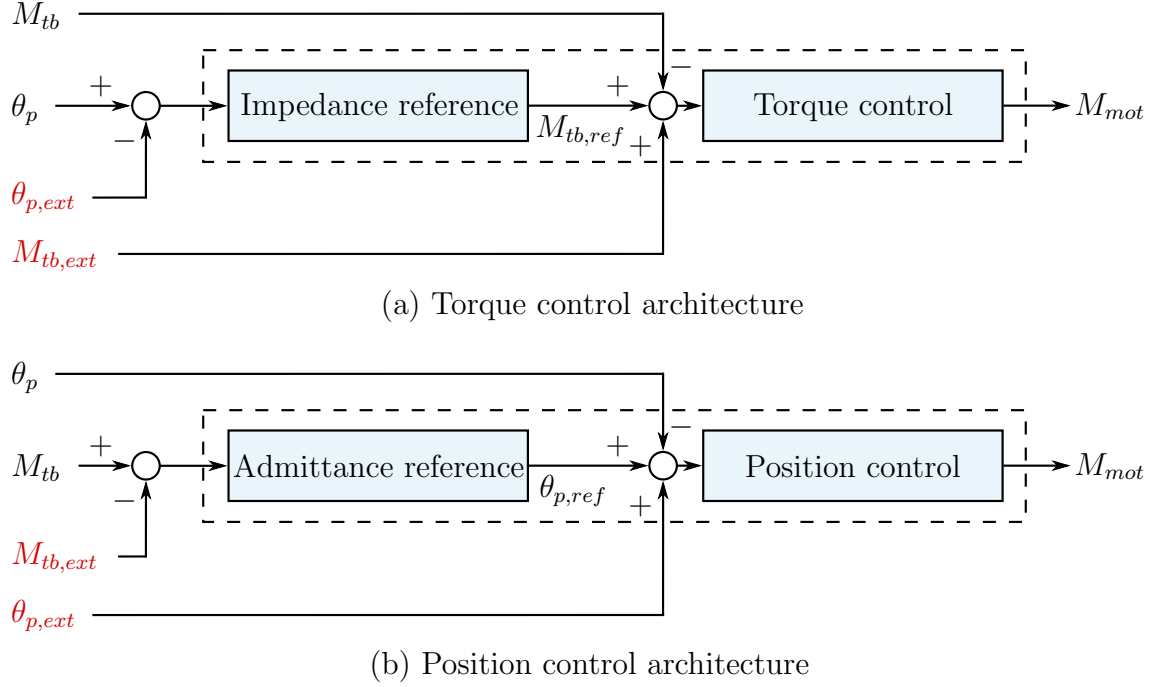


Figure 5.2: A simplified control architecture for realizing active safety function requests, given by $\theta_{p,ext}$ and $M_{tb,ext}$, in closed-loop (a) torque and (b) position control.

control, respectively. In the same figure, the impedance and admittance reference blocks represent the torque and position reference models (Chapter 4), respectively. The main highlight of the given control layout is that the same lower level controller is used to realize both steering feedback and active safety functions sequentially.

Note that the presented control architecture requires a non-transparent setting to follow $\theta_{p,ext}$ and $M_{tb,ext}$; otherwise, the tire–road disturbance would interfere and affect tracking performance. A lower transparency level implies better reference tracking for these external requests. The same applies to SbW-FFb in case the driver–vehicle interaction is analogous to EPAS (i.e., one-channel unilateral teleoperation) such that $y_{ref}^{rack}(t) = \theta_{p1}$ and $\gamma = 0$ in Fig. 3.7(b). Another possible way of completely disconnecting the driver’s haptic sensation from vehicle motion control functions is by sending interventions directly to the RWA (or SbW-rack actuator) such that $y_{ref}^{rack}(t) = \theta_{p1} + \theta_{p,ext}$ and $\gamma = 0$. However, this case is not discussed here any further.

5.2.1 Angular position overlay

In position control, an angular position request from vehicle motion control functions, i.e., $\theta_{p,ext}$, can be directly superimposed on the lower level controller, as shown in Fig. 5.2(b). Evidently, tuning must be performed such that the required lateral motion objective is achieved, given a certain $\theta_{p,ref}$ value from the steering feedback (admittance) reference. This is a straightforward solution, because if the driver is not in the loop (i.e., $M_{tb} \approx 0$ Nm), in theory, it simply represents a typical position controller because $\theta_{p,ref} \approx 0$ rad using Eq. (3.12). However, in torque control, the solution is not that trivial. The angular position

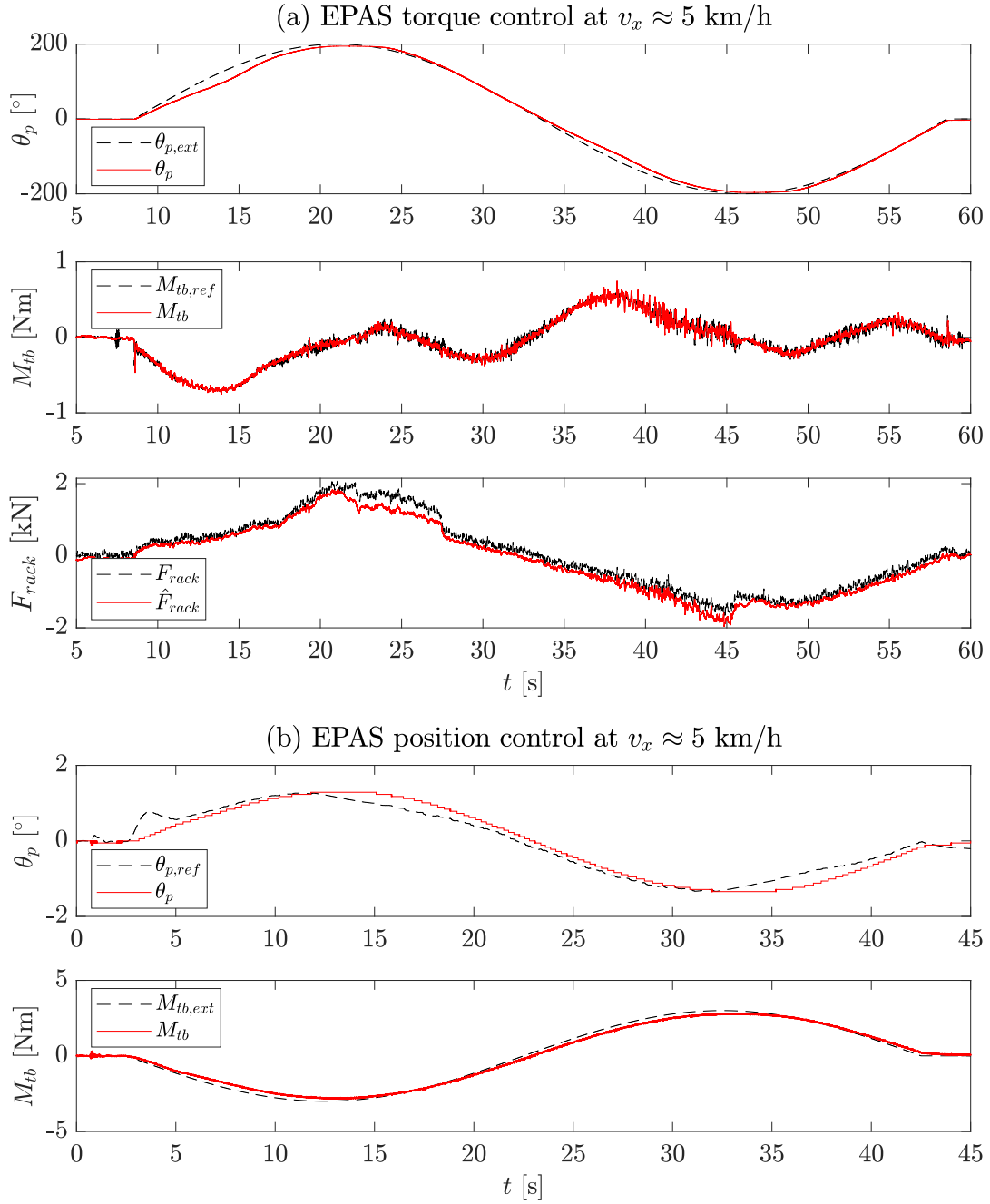


Figure 5.3: A measured time response of (a) angular position overlay in EPAS torque control and (b) driver torque overlay in EPAS position control at a vehicle speed of 5 km/h.

overlay is performed before the torque (or impedance) reference model; mathematically, it becomes the same as position control.

In the Laplace domain, the motor torque is defined as $M_{mot}(s) = H_{fb,M}(s)M_{tb,ref}(s)$, based on Eq. (3.14) and theoretically assuming that no driver is present. Subsequently, the reference torque is derived from Eq. (3.11) and based on Fig. 5.2(a), as follows.

$$\begin{aligned} M_{tb,ref}(s) &= (J_{ref}s^2 + b_{ref}s + c_{ref})(\theta_p(s) - \theta_{p,ext}(s)) \\ &= -H_{ref}^{-1}(s)e_\theta(s) \end{aligned} \quad (5.2)$$

Using Eqs. (3.23) and (5.2), $M_{mot}(s) = H_{fb,\theta}(s)e_\theta(s)$ is obtained as the final expression; hence, it is equal to the position control law in Eq. (3.24).

Consider a real-world example from an EPAS system, as shown in Fig. 5.3(a). The vehicle was driven on a straight road and under a hands-off condition, i.e., no driver torque interference. Then, a low frequency sinus excitation with a peak amplitude of 200° was applied to the $\theta_{p,ext}(t)$ channel. As a result, the vehicle was steered to follow the external request. In reality, $M_{tb}(t) \neq 0$ because it is a sensed signal dependent on state variables; it is not the actual driver input, $M_s(t)$. This maneuver illustrates that the position overlaying in torque control is a feasible solution even for high steering angle amplitudes.

Similarly, the high frequency performance can be evaluated using frequency response excitation with the same setup. The requested variable tracking is shown in the $\theta_p(s)/\theta_{p,ext}(s)$ FRF plot in Fig. 5.4(a) for the torque control setting and with a peak requested angle of 5° . Although the reference tracking bandwidth (i.e., 18.85 rad/s) is sufficient to satisfy the requirements of vehicle motion control functions, it can be further improved by adjusting the reference model parameters, particularly c_{ref} or its equivalent $M_{rack}^{virt}(t)$. Basically, a higher reference stiffness implies an improvement in the tracking performance.

With these two measurements, the proposed angular position overlay concept is demonstrated to be effective for torque control, if it is properly designed. Hence, this can solve the problem of overlaying the vehicle motion control functions using the closed-loop steering feedback controller. An improvement that may be considered in the future is defining the reference model, particularly M_{rack}^{virt} , as a function of the estimated environment load, given by \hat{M}_{rack} . The reason for this is that in the experiments, the corresponding tracking error, e_θ , was found higher in the case of high M_{rack} and given M_{rack}^{virt} setpoint; by increasing M_{rack}^{virt} , this error could be mitigated.

5.2.2 Driver torque overlay

For the driver haptic support functions, an analysis similar to that in the angular position overlay is performed. Let the external torque request variable be $M_{tb,ext}$. The corresponding $M_{tb,ext}$ overlay in torque control can be directly applied to the lower level controller, as shown in Fig. 5.2(a). If a scenario where the driver is assumed to maintain a straight-line path occurs such that $\theta_p = 0$ rad, then $M_{tb,ref} = 0$ Nm using Eq. (3.11). Consequently, the architecture itself becomes a torque controller for such interventions.

The proposed solution, however, is not trivial in position control, because the driver torque overlay is implemented before the position (or admittance) reference model. This can be proved as theoretically the same as torque control assuming that the driver maintains

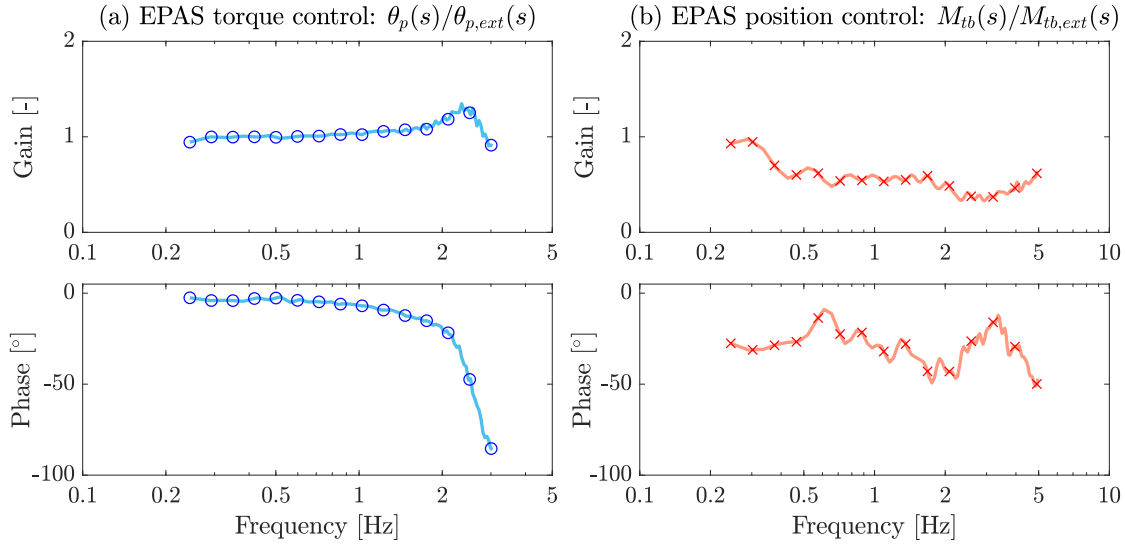


Figure 5.4: Measured frequency responses of EPAS: (a) $\theta_p(s)/\theta_{p,ext}(s)$ FRF for angular position overlay in torque control, and (b) $M_{tb}(s)/M_{tb,ext}(s)$ FRF for driver torque overlay in position control.

a straight-line path (i.e., $\theta_p = 0$ rad). Consider the reference angle definition given in Eq. (3.12), which is resolved further based on Fig. 5.2(b), as follows.

$$\theta_{p,ref}(s) = (J_{ref}s^2 + b_{ref}s + c_{ref})^{-1}(M_{tb}(s) - M_{tb,ext}(s)) = -H_{ref}(s)e_M(s) \quad (5.3)$$

The motor torque variable can be defined in the Laplace domain as

$$M_{mot}(s) = H_{fb,\theta}(s)\theta_{p,ref}(s) = -H_{fb,\theta}(s)H_{ref}(s)e_M(s)$$

using Eqs. (3.24) and (5.3). Finally, $H_{fb,\theta}(s) = -H_{fb,M}(s)H_{ref}^{-1}(s)$ from Eq. (3.23) is inserted into the motor torque definition to obtain $M_{mot}(s) = H_{fb,M}(s)e_M(s)$. The last expression represents the torque control law, similar to that given in Eq. (3.14).

A real-time execution of the above setting can be observed in Fig. 5.3(b) for the steady state response. The driver aimed to maintain a straight-line path (i.e., attempting to achieve a fixed steering wheel), and $M_{tb,ext}$ channel was excited with a low frequency sinus and a peak amplitude of 3 Nm. Although the result shows satisfactory low frequency tracking performance in $M_{tb}(t)$, a major drawback appears in the frequency response excitation.

As shown in Fig. 5.4(b), reference tracking FRF $M_{tb}(s)/M_{tb,ext}(s)$ has inferior (and damped) high frequency performance, although the steady state gain is maintained close to 1. This is mainly caused by the reference model parameters, J_{ref} and b_{ref} , in position control. As described in Section 4.2.2, these parameters are selected to be considerably greater than the torque controller due to the uncoupled stability problem (based on the small gain arguments for an admittance function). Therefore, higher J_{ref} and b_{ref} values imply lower cut-off frequency low-pass filter characteristic and higher damping, respectively. The corresponding adverse effects are clearly visible; hence, this definitely requires an improvement to achieve the desired driver torque overlay in position control, especially at high frequencies.

6 Summary and future work

In this thesis, the problem of steering control has been investigated from the perspective of haptic feedback and (the steering related) active safety functions. A typical solution applied to state-of-the-art electric power assisted steering (EPAS) vehicles is open loop control. From the steering feedback aspect, it means a direct torque control, i.e., without any explicit tracking objectives (Section 3.2.1). Its foremost drawbacks are as follows: attenuated driver–environment transparency and system dependent controller tuning. From the aspect of active safety functions, the external request variable must be realized through the steering actuator. Therefore, each function requires its own feedback controller, e.g., a position controller for vehicle motion control functions and a torque controller for driver haptic support functions. Consequently, they are all abstractly arbitrated on the motor torque request variable, including the steering feedback controller.

To overcome the aforementioned shortcomings of open loop control, two alternative closed-loop steering feedback control architectures based on the principle of torque and position error minimization have been presented. These architectures have the following advantages: system independent steering feedback response, explicit control of the driver–environment transparency, and realizing active safety functions (by torque and position overlays) through the same controller. Because the closed-loop control solution offers a system independent response, the same steering feedback reference can be applied to steer-by-wire force-feedback (SbW-FFb).

The following sections summarize the chapters of this thesis and the appended papers. Lastly, some future work is suggested to continue the research in other possible directions.

6.1 Discussion

A closed-loop haptic controller primarily consists of two parts: reference model and feedback controller. The former is responsible for computing a desired reference variable, and the corresponding error between the reference and measured variables is minimized by the latter. The foregoing forms the basis of the proposed steering feedback controllers. They were developed to answer the research questions formulated in Section 1.2. The first question, “Which closed-loop solution (between torque and position control) offers better steering feedback performance and robustness in EPAS and SbW-FFb?”, was discussed in Chapter 3 and strongly based on the results presented in Papers A and B.

First, the closed-loop architecture was introduced, i.e., torque and position control in EPAS; torque–position and position–position control in SbW. Chapter 3 mainly dealt with non-transparent (steering feedback) causality because the foremost objective was to attain reasonable reference tracking performance while ensuring stability. The model-based solutions, torque and position control, were objectively compared for EPAS and SbW-FFb. For this comparison, a sufficient (single-variable) control law was implemented to compensate for the hardware impedance and to follow the reference variable, thereby considering the following aspects.

(a) **Stability:** Due to multiple feedback interconnections from the plant to the controller, closed-loop stability should be guaranteed. For uncoupled stability, both the inner loop (formed by the feedback controller) and outer loop (including the reference function) should remain stable in isolation. Consequently, the stability conditions were derived using the simplified Nyquist criterion. Based on the small gain arguments and inequality constraints in Eqs. (3.17) and (3.27), small reference stiffness and large reference inertia values are required to maintain torque and position control (uncoupled) stability, respectively. A necessary and sufficient condition for coupled stability is as follows: if the interaction port's admittance function is passive, then stability is achieved regardless of the coupling inertia and spring stiffness. This definition was used to ensure the driver coupled stability for a non-transparent reference variable and the environment coupled stability under transparency. The underlying assumptions are stated in Sections 3.4.1 and 3.5.1 for torque and position control, respectively.

(b) **Tracking performance:** A straightforward proposition to evaluate the controller's performance is through the reference tracking transfer function. This function is defined as the ratio of the measured to the reference variable in the frequency domain. A high cut-off frequency, a low overshoot, and a low phase delay indicate good, accurate, and fast reference tracking performance, respectively. A significantly higher cut-off frequency was achieved in torque control compared with that in position control. The comparison of the reference tracking frequency responses is based on Fig. 3.10 and 3.12. The main reason for the difference in performance is high system inertia; this is in addition to practical reasons, such as low resolution and high noise in the measured angular velocity signal.

(c) **Robustness:** This characteristic was adjudged in terms of the change in the controller's cut-off frequency (with respect to its nominal value) in the presence of the parametric uncertainty of the coupling port. Two main sources of uncertainty were considered: coupling stiffness at the environment port (due to variation in the tire-road interaction dynamics) and coupling inertia at the driver port (due to variation in the driver arm inertia). Although both controllers are robust against environmental uncertainty, the position controller is found to be extremely sensitive toward the arm inertia, as shown in Fig. 3.12(c). Higher coupled inertia results in slower reference tracking performance. To improve robustness against the coupling inertia, the use of a multi-variable position control solution based on the LMI- \mathcal{H}_∞ optimization principle (presented in Paper E) is proposed. Basically, the measured torsion bar torque signal was also utilized within the position controller in an optimal sense. The results clearly illustrated an improvement in the reference tracking performance with the proposed \mathcal{H}_∞ position control solution, especially in case of inertial uncertainty, as compared to single-variable position controller. Although robustness improved to a certain extent, the position controllers, in general, inherently suffered from performance loss with increasing coupling inertia compared to torque control.

The discussion in Chapter 4 was dedicated to the search for an answer to the second research question, "How should the steering feedback response be mathematically represented in the reference model independent of system dynamics?". In a broader context, this chapter pertains to the reference generator (or higher level control) for a closed-loop steering feedback controller. The model structure for computing a desired reference variable depending on the causality (i.e., either torque or position control) was proposed. A reasonable reference model

should include (although it is not be limited to) different components and/or model-based functions to control: inertia, damping, Coulomb friction, basic assistance, trajectory return, virtual endstop, and transparency. Each of these was briefly explained in Section 4.1.

In EPAS, the closed-loop controller causes environmental disturbance attenuation, and subsequently, the reference model must generate a steering feedback. Whereas, in SbW, the reference model can be used for the same purpose because the system is mechanically disconnected from the environment. Therefore, as a first step, a reference model was proposed for the non-transparent steering feedback in EPAS and SbW. This was achieved using virtual environment dynamics for the rack force variable (or rack force model) in Section 4.2.1. Here, an approach for building a non-linear rack force model using vehicle measurements with different sensor signals, such as lateral acceleration, yaw rate, vehicle speed, and pinion angle, under nominal tire-road conditions was demonstrated. This section extends the results of Paper C, which is limited to a linear tire model. Furthermore, the non-transparent control setting was evaluated using the proposed rack force model in EPAS and SbW systems (Section 4.2.2) for virtual haptic feedback, regardless of the environment interaction dynamics. The corresponding results are shown in Fig. 4.6–4.8.

An important finding in position control was the setpoint for reference inertia and reference damping parameters. Based on the small gain arguments for uncoupled stability and Eq. (3.27), a low position controller cut-off frequency caused the reference inertia and damping to be set higher than nominal. As a result, the steering feedback response became considerably damped due to the slower dynamics of the reference admittance function in the outer loop. This constrains a faster haptic response (particularly for transparency) and clearly highlights the performance–stability tradeoff.

The next questions are, why is the driver–environment transparency necessary and how can it be achieved? As described in the introduction (Section 1.1.2), transparency is required to improve the driving performance, in particular, under tire–road interaction uncertainty, or for instance, when road surface conditions vary. To achieve the above, an intermediate step for estimating the actual rack force was considered. This is discussed in Section 4.3, where a comparison between two observer schemes is presented. The first scheme involved the estimation of actual rack force using vehicle motion states. The second approach utilized steering system signals. The former estimation method computed the rack force variable slower due to various reasons: mechanically delayed motion reaction caused by vehicle dynamic effects and inertial properties, lower sampling frequency of the measured vehicle motion signals, and high dependency on the accuracy of the tire model. In contrast, using the steering system based estimation, a faster and more accurate estimate of the rack force variable was obtained, especially with the non-linear method (i.e., including the Coulomb friction model). This is also illustrated in Paper D. The best available rack force estimate was further utilized to attain full transparency in the proposed closed-loop control architectures. The results presented in Section 4.4 validated that the goal of achieving transparency was attained.

The discussion up to this section describes the manual adjustment of the driver–environment transparency using a static gain. In Section 4.5, an MPC (model predictive control) based approach is proposed to adapt transparency as a function of vehicle motion states; the function is subsequently named transparency control. The purpose of such a

function is to compute optimal transparency using the deviation between the reference and measured vehicle motion states under environmental uncertainty and given non-transparency as the initial condition. From the presented examples, this algorithm can be claimed as capable of haptically informing the driver about the tire–road interaction uncertainty, which the non-transparent setting cannot provide.

The last research question, “How can a steering related active safety function be realized using the closed-loop steering feedback controller?”, is explained in Chapter 5. The motor torque overlay (as in open loop control) conflicts with the closed-loop setting due to the controller’s integral state and its disturbance attenuation property, as described in Section 5.2. Thereby, a direct superimposition of the request variable can be an alternative to realize these active safety interventions using the same controller.

For vehicle motion control functions, an angular position overlay is implemented; a driver torque overlay was used for haptic support functions. These signals can be superimposed in a straightforward manner with the position and torque control settings (i.e., with the same causality as that of steering feedback controller), as shown in Fig. 5.2, respectively. However, an angular position overlay in torque control and a driver torque overlay in position control are not trivial. They were achieved by superimposing the same variable before their respective reference models. This is illustrated using real-world experiments in Fig. 5.3 and 5.4, emphasizing the execution of the proposed hypothesis. Hence, the driver torque or angular position request variable from active safety function can be directly realized via the closed-loop steering feedback controller without conflict.

6.2 Conclusion

Two model-based closed-loop steering feedback control solutions have been investigated and implemented in this research for the attenuated driver–environment transparency problem and system independent haptic response. The main elements of the closed-loop architecture (i.e., reference model, feedback controller, and disturbance observer) have been formulated for real-time execution. The results of simulation, hardware-in-the-loop test rig, and prototype vehicle, demonstrated promising outcomes. Some of the concluding remarks are summarized as follows:

- Better reference tracking performance and robustness are achievable using torque control than position control; this is because the latter is affected by higher and/or varying system inertia.
- For uncoupled stability, given the inner loop tracking, low reference stiffness and high reference inertia are required in torque and position control, respectively. The latter indicates slow reference admittance dynamics in the (position control) outer loop, thus illustrating the conflict between stability and fast haptic performance.
- The driver–environment transparency can be explicitly controlled in the presented closed-loop architectures, although dependent on the quality of the estimated rack force signal. The steering model-based rack force estimation provides a more accurate and faster estimate than the vehicle model-based approach.

- A direct signal overlay from active safety functions can be realized using the closed-loop steering feedback controller. This means, an angular position overlay from vehicle motion control functions, and a driver torque overlay from haptic support functions.

Comprehensive haptic feedback control solutions have been proposed despite some challenges that remain. A good starting point has been suggested for developing future steering systems that are suitable not only for manipulating the driver’s steering feedback but also for controlling the lateral motion of semi-autonomous and fully-autonomous vehicles.

6.3 Future work

Although the work presented here has highlighted many benefits, certain aspects require further investigation before the proposed controllers can be realized in the production of vehicles.

A topic not explicitly discussed in this thesis is the human factor, i.e., the subjective perception of steering feedback. This aspect has not been considered, although the functions in the reference model structure (Section 4.1) are mostly introduced based on the requirements posed by the driver’s expectations. In this research, controller development and its tuning were kept as objective as possible; nevertheless, they were devised to satisfy the desired outcome broadly. Therefore, the subjective steering feedback aspect must be evaluated thoroughly to resolve many unanswered questions. For instance, what should be an acceptable on-center steering feedback? How does a driver perceive variations in transparency under changing road conditions and so on? The answer to these questions are anticipated to explain how the functions under different scenarios can be parameterized to provide the driver a “subjectively” acceptable steering feedback response.

In terms of the controller, not everything has been investigated in this work. For example, a typical non-linear tire model valid for vehicle speeds exceeding 15 km/h was used in the virtual environment model (Section 4.2.1). To improve the non-transparent steering feedback response at lower speeds and parking maneuvers, a different (low speed) tire model must be considered. Another example is, the transparency control algorithm (Section 4.5) based on the MPC formulation must be executed in real-world experiments using different and varying control horizons to validate the theoretical results. Moreover, a thorough MPC feasibility analysis is necessary to attain realistic optimal transparency.

Finally, in general, the position controller requires further improvement to realize high frequency steering feedback reference dynamics. As a result, the haptic performance and transparency results were found limited. This is due to low inner loop position tracking performance that subsequently requires high reference inertia in the outer loop admittance for stability; thus generating slow reference dynamics.

As far as the interventions from active safety functions are concerned, the application of a direct signal overlay from existing functions to the closed-loop steering feedback controller is definitely worth considering. For instance, overlaying the angular position request signal from state-of-the-art functions, such as lane keeping assistance and pilot assist, must be performed. This can open new research opportunities on shared steering control depending on how the two functionalities interact with each other in the proposed architecture.

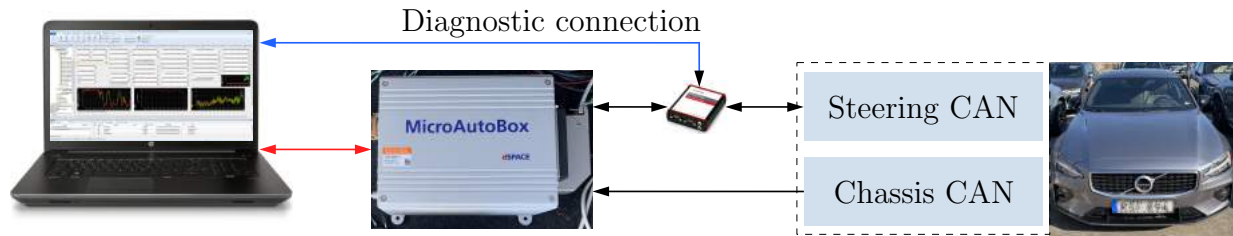
Appendix

A Experimental setups

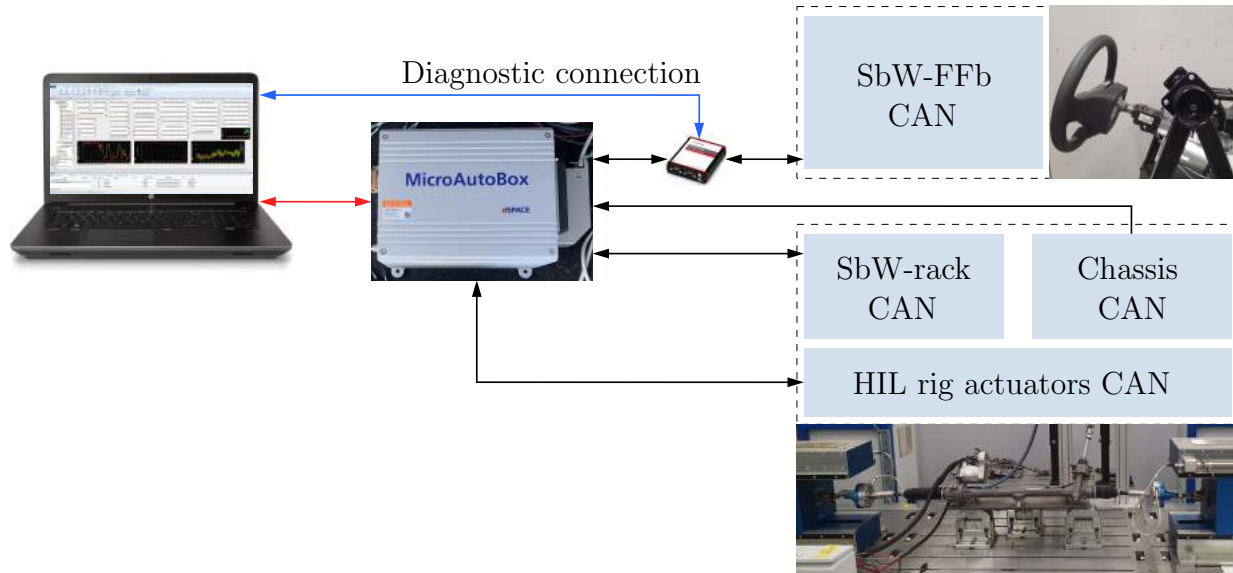
This chapter briefly highlights the experimental setup and test track layouts used in the thesis. The EPAS vehicle experiments were performed on Volvo S90 and S60 equipped with dSPACE Autobox (DS1007) and MicroAutobox (DS1401), respectively. The SbW experiments were conducted on a HIL test rig equipped with dSPACE Autobox (DS1006) and a real-time IPG CarMaker vehicle model. These experimental setups are illustrated in Fig. A.1. Some important considerations during real-world experiments were undertaken, which are stated as follows.

- (a) The control algorithms (including reference model and feedback controller) and disturbance observers were developed in MATLAB/Simulink, and executed using the real-time interface blocks.
- (b) The measured steering system signals (i.e., pinion angle, pinion speed, torsion bar torque, and applied motor torque) and corresponding motor torque requests in EPAS and RWA were interfaced using a private CAN bus at 1 kHz sampling frequency. In contrast, the measured SbW-FFb signals were sampled at 2 ms.
- (c) The actual rack force was measured using tie-rod strain gauges at a sampling frequency of 1 kHz. Due to high noise levels in the measured signal, a zero-phase (acausal) 30 Hz low-pass fourth-order Butterworth filter was implemented in post-processing.
- (d) The lateral acceleration and yaw rate signals were sampled at 15 ms and 30 ms, respectively. The onboard IMU signals were synchronized using an external IMU sensor before rack force estimation.
- (e) The continuous-time LMI- \mathcal{H}_∞ controller was discretized using the explicit Euler method in MATLAB/Simulink at 1 ms time-step.
- (f) To compensate for the Coulomb motor and pinion friction torques, the estimated values from the steering model-based observer were used. The compensating torque was added to the motor torque request variable; an example is illustrated in Paper E.
- (g) Ethernet connection was used to communicate between the computer and Autobox (or MicroAutobox). A steering CAN-breakout was provided as a diagnostic connection for ensuring safe operation, as shown in Fig. A.1.
- (h) For the SbW-rack operation, the rack force variable was requested from the CarMaker vehicle model to the external test rig rack actuators in the force-control mode.

The frequency response measurements were performed on a straight-line path under nominal road conditions, and the slow ramp steer maneuvers in Fig. 4.4 and 4.5 were performed on a skid-pad surface. However, for the closed-circuit driving maneuvers and transparency analysis in Chapter 4, two different test track layouts were considered. The nominal road surface measurements were conducted on proving ground shown in Fig. A.2(a); the measurements for uncertain road conditions (on a low tire-road friction surface) were conducted on proving ground shown in Fig. A.2(b).



(a) EPAS vehicle configuration



(b) SbW HIL test rig configuration

Figure A.1: Illustration of experimental setups with steering and chassis CAN communications, and a diagnostic connection in (a) EPAS vehicle and (b) SbW HIL test rig. The latter consists of two actuators, i.e., SbW-FFb and RWA.

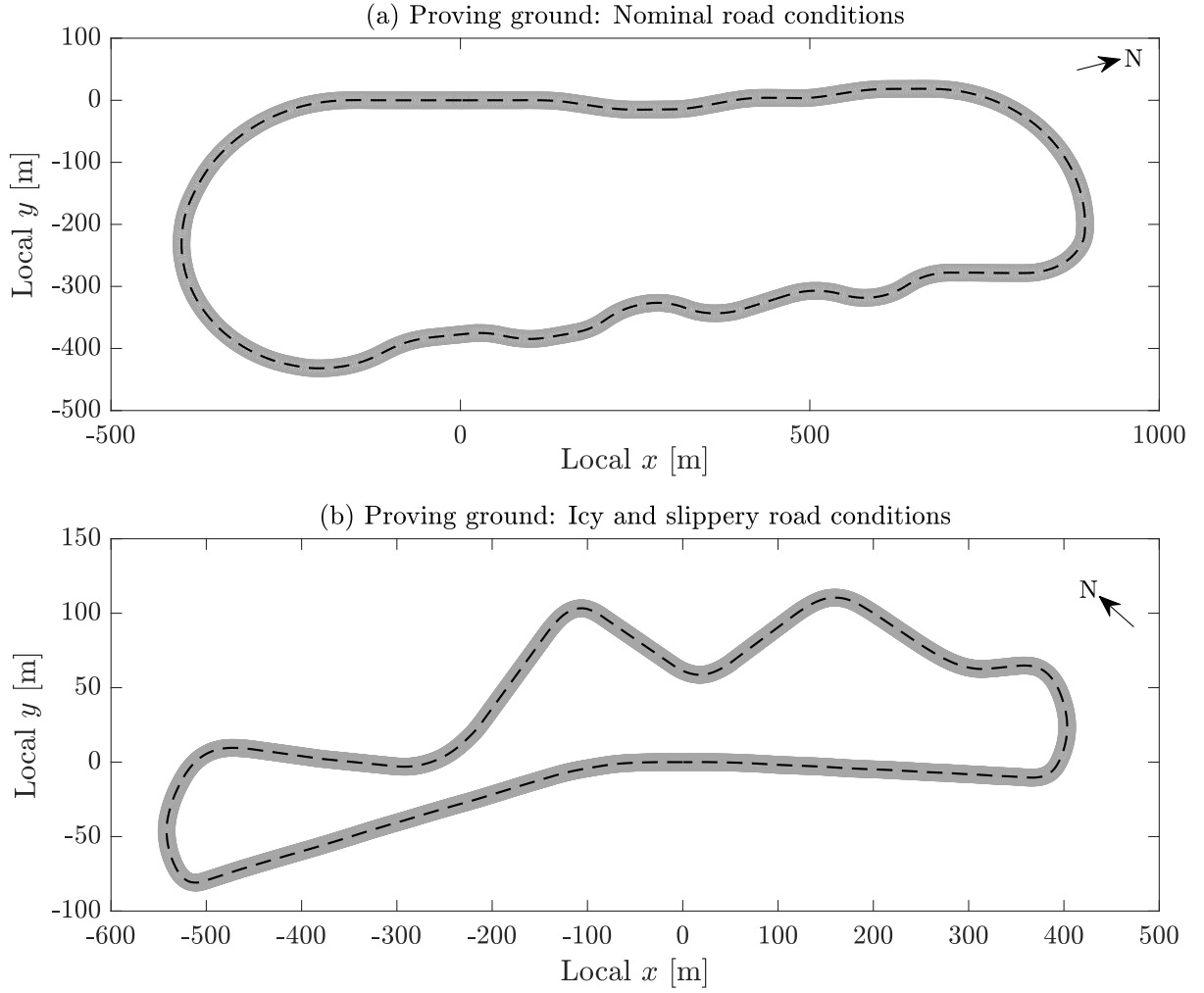


Figure A.2: Maps of proving ground (or test track) used for closed-circuit driving: (a) nominal road conditions with $\mu_{y_0} \approx 0.95$; (b) icy and slippery uncertain road conditions with $\mu_{y_0} \approx 0.45$.

B Model and controller parameters

To implement a model-based controller, the system dynamics must be known. Consequently, some unknown parameters have to be estimated. Although system identification is kept out of context here, the required model parameters, controller gains, and observer noise covariance values are subsequently listed. Accordingly, a brief description of each appended table in this chapter is as follows.

Table B.1: The vehicle and tire model parameters needed for standalone simulations and vehicle model-based rack force observer in Section 4.3.1 are summarized.

Table B.2: The EPAS model parameters, defined in Section 2.1.1, are required for controller design in Section 4.1 and rack force observer in Section 4.3.2.

Table B.3: The SbW model parameters, defined in Section 2.1.2, are required for controller design in Section 4.1 and rack force observer in Section 4.3.2.

Table B.4: The real-time closed-loop (torque and position) controller gains for EPAS, SbW-FFb, and SbW-rack are given in this table.

Table B.5: The state and measured noise covariance values for the IMU based estimator (Section 4.3.1) are summarized here.

Table B.6: The state and measured noise covariance values for the steering system based estimator (Section 4.3.2) are summarized here.

The result in Section 3.5.3 and Paper E is based on the LMI- \mathcal{H}_∞ control solution, as defined in Eq. (3.33). The controller was synthesized using the given model parameters and weighting functions in Paper E. For the EPAS system in context, the controller matrix (K), which has been discretized for real-time execution using the explicit Euler solver at 1 ms time-step, is given as follows. Note that the input signals are: e_θ , \dot{e}_θ , and M_{tb} , respectively.

$$K := \left[\begin{array}{ccccc|ccc} 0.8107 & 0.4285 & -0.0633 & -0.0032 & 2.2727 & 0.0025 & 0.0004 & 0 \\ -0.4285 & 0.3094 & -0.2544 & -0.0081 & 3.5688 & 0.0059 & -0.0001 & 0 \\ 0.0633 & -0.2544 & 0.7516 & -0.0170 & 0.7812 & 0.0015 & -0.0002 & 0 \\ 0.0032 & -0.0081 & -0.0170 & 0.8836 & 0.0082 & 0.0000 & 0 & 0 \\ 0 & 0 & 0 & 0 & 1 & 0.0027 & 0 & 0 \\ \hline 649.9 & 6632.3 & 2144.6 & 70.4 & 0 & 0 & 4.6050 & -0.0029 \end{array} \right]$$

A similar LMI- \mathcal{H}_∞ solution for the given SbW-FFb model is mentioned as follows. The corresponding measured frequency responses are shown in Fig. 3.13, and some additional step response results in Paper E.

$$K := \left[\begin{array}{ccccc|ccc} 0.9484 & 0.2739 & -0.0005 & 0.0044 & -0.6264 & -0.0003 & 0 & 0 \\ -0.2739 & 0.7128 & -0.1753 & 0.0474 & -1.8041 & -0.001 & 0 & 0 \\ 0.0005 & -0.1753 & 0.7648 & 0.1167 & -0.7011 & -0.0004 & 0 & 0 \\ -0.0044 & 0.0474 & 0.1167 & 0.7096 & 0.1331 & 0.0001 & 0 & -0.0001 \\ 0 & 0 & 0 & 0 & 1 & 0.001 & 0 & 0 \\ \hline 291.3 & 2301.8 & 1089.4 & -323.6 & 0 & 0 & -0.1635 & 0.0044 \end{array} \right]$$

Table B.1: Definitions and values of vehicle model parameters

Symbol	Description	Value	Units
m	Vehicle mass	2025	kg
l_f	Front axle to CG	1.3280	m
l_r	Rear axle to CG	1.6130	m
w_f, w_r	Front and rear track widths	1.6180	m
h_{cg}	CG height	0.5440	m
J_z	Vehicle yaw inertia	3100	kgm ²
t_m	Mechanical castor trail	0.0326	m
i_{rw}	Front wheels to rack ratio	6.250	m ⁻¹
r_{0f}, r_{0r}	Front and rear relaxation lengths	0.12, 0.35	m
F_{z0}	Tire model nominal load	5994	N
$B_{y,f}, B_{y,r}$	Lateral force tire model parameter	13.26, 14.54	1/rad
$C_{y,f}, C_{y,r}$	Lateral force tire model parameter	0.94, 1.23	—
$B_{t,f}$	Aligning moment tire model parameter	0.02	1/rad
$C_{t,f}$	Aligning moment tire model parameter	1.09	—
$D_{t,f}$	Aligning moment tire model parameter	0.05	m
$E_{t,f}$	Aligning moment tire model parameter	-7.90	—

Table B.2: Definitions and values of EPAS model parameters

Symbol	Description	Value	Units
b_s	Steering damping	0.1414	Nm-s/rad
J_s	Steering inertia	0.0337	kgm ²
k_{tb}	Torsion bar damping	0.2292	Nm-s/rad
c_{tb}	Torsion bar stiffness	143.24	Nm/rad
b_p	Pinion damping	0.002	Nm-s/rad
J_p	Pinion inertia	0.0098	kgm ²
k_{rack}	Rack damping	21.081	N-s/m
m_{rack}	Effective rack mass	103.78	kg
b_{mot}	Rack motor damping	0.00002	Nm-s/rad
J_{mot}	Rack motor inertia	0.00025	kgm ²
k_{belt}	Motor belt damping	0.00573	Nm-s/rad
c_{belt}	Motor belt stiffness	40.1071	Nm/rad
i_{mot}	Motor-pinion ratio	25*	—
i_{rp}	Rack-pinion ratio	100*	rad/m
i_{mr}	Motor-rack ratio	2500*	rad/m
$c_{rack,fric}$	Rack friction model stiffness	2000	N/mm
$c_{mot,fric}$	Motor friction model stiffness	0.25	Nm/rad
$F_{rack,fric}^0$	Rack Coulomb friction force	172	N
$M_{mot,fric}^0$	Motor Coulomb friction torque	0.038	Nm

*Rounded-off due to proprietary reasons.

Table B.3: Definitions and values of SbW model parameters

Symbol	Description	Value	Units
b_s	Steering damping	0.0195	Nm-s/rad
J_s	Steering inertia	0.0286	kgm ²
k_{tb}	Torsion bar damping	0.1150	Nm-s/rad
c_{tb}	Torsion bar stiffness	143.24	Nm/rad
b_{p1}	FFb pinion damping	0.0025	Nm-s/rad
J_{p1}	FFb pinion inertia	0.0001	kgm ²
b_{mot1}	FFb motor damping	0.00008	Nm-s/rad
J_{mot1}	FFb motor inertia	0.00034	kgm ²
k_{belt1}	FFb belt damping	0.0001	Nm-s/rad
c_{belt1}	FFb belt stiffness	150	Nm/rad
i_{mot1}	FFb motor-pinion ratio	3*	—
$c_{p,fric}$	FFb pinion friction model stiffness	100	Nm/rad
$c_{mot,fric}$	FFb motor friction model stiffness	10	Nm/rad
$M_{p,fric}^0$	FFb pinion Coulomb friction torque	0.03	Nm
$M_{mot,fric}^0$	FFb motor Coulomb friction torque	0.01	Nm
b_{p2}	RWA pinion damping	0.001	Nm-s/rad
J_{p2}	RWA pinion inertia	0.0107	kgm ²
k_{rack}	Rack damping	21.081	N-s/m
m_{rack}	Effective rack mass	112.57	kg
b_{mot2}	RWA motor damping	0.00002	Nm-s/rad
J_{mot2}	RWA motor inertia	0.00026	kgm ²
k_{belt2}	RWA belt damping	0.00573	Nm-s/rad
c_{belt2}	RWA belt stiffness	40.1071	Nm/rad
i_{mot2}	RWA motor-pinion ratio	25*	—
i_{rp}	Rack-pinion ratio	100*	rad/m
i_{mr}	RWA motor-rack ratio	2500*	rad/m
$c_{rack,fric}$	Rack friction model stiffness	2000	N/mm
$c_{mot,fric}^{rack}$	RWA motor friction model stiffness	0.25	Nm/rad
$F_{rack,fric}^0$	Rack Coulomb friction force	136	N
$M_{mot,fric}^{rack,0}$	RWA motor Coulomb friction torque	0.04	Nm

*Rounded-off due to proprietary reasons.

Table B.4: Real-time controller parameters

Symbol	EPAS	SbW-FFb	SbW-rack	Units
β_0	8	15	8	Nm/rad/s
β_1	5	5	4.35	Nm/rad
β_2	0.48	0.325	0.45	Nm-s/rad
β_3	0.0065	0.00035	0.00065	Nms ² /rad
α_0	6	15	—	1/s
α_1	0.35	0.145	—	—
α'_1	-0.0175	0.0725	—	—

Table B.5: IMU based estimator parameters

Symbol	IMU: EKF	IMU: UKF
q_1	0.0001	0.0001
q_2	0.0003	0.0003
q_3, \dots, q_6	0.00001	0.00001
q_7, \dots, q_{10}	0.0000002	0.0000002
q_{11}, q_{12}	0	0
r_1	0.20	0.20
r_2	1	1
n	—	12
α	—	0.05
β	—	2
λ	—	-11.97

$\mathbf{Q}_t = \text{diag}(q_1, q_2, \dots, q_n)$ and $\mathbf{R}_t = \text{diag}(r_1, r_2)$

Table B.6: Steering system based estimator parameters

Symbol	EPAS: KF	EPAS: UKF	SbW-rack: KF	SbW-rack: UKF
q_1, q_2	0.00001	0.00001	0.0001	0.00001
q_3	0.01	0.01	0.001	0.001
q_4	0.10	0.10	0.20	0.20
q_5	100	100	50	1000
q_6	—	0.10	—	0.10
q_7	—	0.000001	—	0.000001
r_1	0.95	0.95	0.95	0.95
r_2	0.001	0.001	0.002	0.002
n	—	7	—	7
α	—	0.05	—	0.05
β	—	2	—	2
λ	—	-6.9825	—	-6.9825

$\mathbf{Q}_t = \text{diag}(q_1, q_2, \dots, q_n)$ and $\mathbf{R}_t = \text{diag}(r_1, r_2)$

References

- [1] A. Arikere, D. Yang, and M. Klomp, “Optimal motion control for collision avoidance at left turn across path/opposite direction intersection scenarios using electric propulsion,” *Vehicle System Dynamics*, vol. 57, no. 5, pp. 637–664, 2019.
- [2] M. Jonasson and M. Thor, “Steering redundancy for self-driving vehicles using differential braking,” *Vehicle System Dynamics*, vol. 56, no. 5, pp. 791–809, 2018.
- [3] M. Klomp, M. Jonasson, L. Laine, L. Henderson, E. Regolin, and S. Schumi, “Trends in vehicle motion control for automated driving on public roads,” *Vehicle System Dynamics*, vol. 57, no. 7, pp. 1028–1061, 2019.
- [4] L. M. Henderson, “Improving emergency braking performance of heavy goods vehicles,” Ph.D. dissertation, University of Cambridge, 2013.
- [5] L. Persson, “Model Predictive Control for Cooperative Rendezvous of Autonomous Unmanned Vehicles,” Ph.D. dissertation, KTH Royal Institute of Technology, 2021.
- [6] SAE J3016, “Taxonomy and Definitions for Terms Related to Driving Automation Systems for On-Road Motor Vehicles,” *Surface Vehicle Recommended Practice*, SAE International, 2018.
- [7] J. G. Wildenbeest, D. A. Abbink, C. J. Heemskerk, F. C. Van Der Helm, and H. Boessenkool, “The impact of haptic feedback quality on the performance of teleoperated assembly tasks,” *IEEE Transactions on Haptics*, vol. 6, no. 2, pp. 242–252, 2013.
- [8] R. Gillespie, *Haptic Interface to Virtual Environments, Robotics and Automation Handbook*. CRC Press LLC, 2005.
- [9] H. Culbertson, S. B. Schorr, and A. M. Okamura, “Haptics: The present and future of artificial touch sensation,” *Annual Review of Control, Robotics, and Autonomous Systems*, vol. 1, no. 1, pp. 385–409, 2018.
- [10] A. Bolopion and S. Régnier, “A review of haptic feedback teleoperation systems for micromanipulation and microassembly,” *IEEE Transactions on Automation Science and Engineering*, vol. 10, no. 3, pp. 496–502, 2013.
- [11] K. Kosuge, Y. Fujisawa, and T. Fukuda, “Control of mechanical system with man-machine interaction,” *Proceedings of the IEEE/RSJ International Conference on Intelligent Robots and Systems*, vol. 1, pp. 87–92, 1992.
- [12] D. Lawrence, “Stability and transparency in bilateral teleoperation,” *IEEE Transactions on Robotics and Automation*, vol. 9, no. 5, pp. 624–637, 1993.
- [13] R. O. Ambrose, H. Aldridge, R. S. Askew, R. R. Burrige, W. Bluethmann, M. Diftler, D. Magruder, F. Rehnmark, and N. Johnson, “Robonaut : NASA’s Space Humanoid,” *IEEE Intelligent Systems and their Applications*, vol. 15, no. 4, pp. 57–63, 2000.
- [14] J. G. Wildenbeest, R. J. Kuiper, F. C. Van Der Helm, and D. A. Abbink, “Position control for slow dynamic systems: Haptic feedback makes system constraints tangible,” *Conference Proceedings - IEEE International Conference on Systems, Man and Cybernetics*, vol. 2014-Janua, no. January, pp. 3990–3995, 2014.
- [15] A. M. Okamura, “Haptic feedback in robot-assisted minimally invasive surgery,” *Current opinion in urology*, vol. 19, pp. 102–107, 2009.

-
- [16] A. Tobergte, P. Helmer, U. Hagn, P. Rouiller, S. Thielmann, S. Grange, A. Albuschäffer, F. Conti, and G. Hirzinger, “The sigma.7 haptic interface for MiroSurge: A new bi-manual surgical console,” *IEEE International Conference on Intelligent Robots and Systems*, pp. 3023–3030, 2011.
 - [17] U. Hagn, R. Konietzschke, B. Kübler, U. Seibold, A. Tobergte, M. Nickl, S. Jörg, and G. Hirzinger, “Telemanipulator for remote minimally invasive surgery,” *IEEE Robotics and Automation Magazine*, vol. 15, no. 4, pp. 28–38, 2008.
 - [18] C. R. Wagner and R. D. Howe, “Force feedback benefit depends on experience in multiple degree of freedom robotic surgery task,” *IEEE Transactions on Robotics*, vol. 23, no. 6, pp. 1235–1240, Dec 2007.
 - [19] N. Dahlström, “Pilot training in our time - use of flight training devices and simulators,” *Aviation*, vol. 12, no. 1, pp. 22–27, 2008. [Online]. Available: <https://doi.org/10.3846/1648-7788.2008.12.22-27>
 - [20] N. Dahlström, S. Dekker, R. van Winsen, and J. Nyce, “Fidelity and validity of simulator training,” *Theoretical Issues in Ergonomics Science*, vol. 10, no. 4, pp. 305–314, 2009. [Online]. Available: <https://doi.org/10.1080/14639220802368864>
 - [21] R. T. Hays, J. W. Jacobs, C. Prince, and E. Salas, “Flight simulator training effectiveness: A meta-analysis,” *Military Psychology*, vol. 4, no. 2, pp. 63–74, 1992. [Online]. Available: https://doi.org/10.1207/s15327876mp0402_1
 - [22] G. Aguirre-Ollinger, J. E. Colgate, M. A. Peshkin, and A. Goswami, “Design of an active one-degree-of-freedom lower-limb exoskeleton with inertia compensation,” *International Journal of Robotics Research*, vol. 30, no. 4, pp. 486–499, 2011.
 - [23] A. Gupta, M. K. O’Malley, V. Patoglu, and C. Burgar, “Design, control and performance of RiceWrist: A force feedback wrist exoskeleton for rehabilitation and training,” *International Journal of Robotics Research*, vol. 27, no. 2, pp. 233–251, 2008.
 - [24] H. Vallery, J. Veneman, E. van Asseldonk, R. Ekkelenkamp, M. Buss, and H. van Der Kooij, “Compliant actuation of rehabilitation robots,” *IEEE Robotics and Automation Magazine*, vol. 15, no. 3, pp. 60–69, 2008.
 - [25] Bosch Mobility Solutions, “Electric power steering belt drive servo unit,” <https://www.bosch-mobility-solutions.com/en/solutions/steering/electric-power-steering-belt-drive-servo-unit/>, accessed: 2021-07-05.
 - [26] Bosch Group, “Zf lenksysteme servoelectric,” <http://www.bosch-presse.de/pressportal/zip?country=de&language=en&docId=41849>, accessed: 2021-07-05.
 - [27] Hitachi Automotive Systems Americas, Inc., “Belt drive electric power steering system,” <http://www.hitachi-automotive.us/Products/oem/DCS/Steering/index.htm>, accessed: 2021-07-05.
 - [28] G. Fontaras, N. G. Zacharof, and B. Ciuffo, “Fuel consumption and co2 emissions from passenger cars in europe – laboratory versus real-world emissions,” *Progress in Energy and Combustion Science*, vol. 60, pp. 97–131, 2017. [Online]. Available: <http://www.sciencedirect.com/science/article/pii/S0360128516300442>
 - [29] M. Harrer and P. Pfeffer, *Steering Handbook*. Springer International Publishing Switzerland, 2017.

- [30] J. E. Colgate, "Robust control of dynamically interacting systems," *International Journal of Control*, vol. 48, no. 1, pp. 65–88, 1988.
- [31] N. Hogan and S. Buerger, *Impedance and Interaction Control, Robotics and Automation Handbook*. CRC Press LLC, 2005.
- [32] W. S. Newman, "Stability and performance limits of interaction controllers," *Journal of Dynamic Systems, Measurement and Control, Transactions of the ASME*, vol. 114, no. 4, pp. 563–570, 1992.
- [33] J. Vogel, J. Bayer, and P. Van Der Smagt, "Continuous robot control using surface electromyography of atrophic muscles," *IEEE International Conference on Intelligent Robots and Systems*, pp. 845–850, 2013.
- [34] L. R. Hochberg, D. Bacher, B. Jarosiewicz, N. Y. Masse, J. D. Simeral, J. Vogel, S. Haddadin, J. Liu, S. S. Cash, P. Van Der Smagt, and J. P. Donoghue, "Reach and grasp by people with tetraplegia using a neurally controlled robotic arm," *Nature*, vol. 485, no. 7398, pp. 372–375, 2012.
- [35] E. Colgate and N. Hogan, "An analysis of contact instability in terms of passive physical equivalents," *International Conference on Robotics and Automation*, vol. 1, pp. 404–409, 1989.
- [36] H. Vallery, E. H. Van Asseldonk, M. Buss, and H. Van Der Kooij, "Reference trajectory generation for rehabilitation robots: Complementary limb motion estimation," *IEEE Transactions on Neural Systems and Rehabilitation Engineering*, vol. 17, no. 1, pp. 23–30, 2009.
- [37] G. Ferretti, G. A. Magnani, P. Rocco, L. Viganò, and A. Rusconi, "On the use of torque sensors in a space robotics application," *2005 IEEE/RSJ International Conference on Intelligent Robots and Systems, IROS*, pp. 2638–2643, 2005.
- [38] H. Vallery, R. Ekkelenkamp, H. Van Der Kooij, and M. Buss, "Passive and accurate torque control of series elastic actuators," *IEEE International Conference on Intelligent Robots and Systems*, pp. 3534–3538, 2007.
- [39] W. Van Dijk, H. Van Der Kooij, B. Koopman, E. H. Van Asseldonk, and H. Van Der Kooij, "Improving the transparency of a rehabilitation robot by exploiting the cyclic behaviour of walking," *IEEE International Conference on Rehabilitation Robotics*, 2013.
- [40] H. Geyer and H. Herr, "A muscle-reflex model that encodes principles of legged mechanics predicts human walking dynamics and muscle activities BT - IEEE Trans Neural Syst Rehabil Eng," *Ieee Transactions on Neural Systems and Rehabilitation Engineering*, vol. 18, no. 3, pp. 1–10, 2010.
- [41] A. Calanca, L. Capisani, and P. Fiorini, "Robust force control of series elastic actuators," *Actuators*, vol. 3, no. 3, pp. 182–204, 2014.
- [42] J. M. Caputo and S. H. Collins, "A universal ankle-foot prosthesis emulator for human locomotion experiments," *Journal of Biomechanical Engineering*, vol. 136, no. 3, 2014.
- [43] C. Ott, R. Mukherjee, and Y. Nakamura, "Unified impedance and admittance control," *Proceedings - IEEE International Conference on Robotics and Automation*, pp. 554–561, 2010.
- [44] J. Zhang, C. C. Cheah, and S. H. Collins, "Experimental comparison of torque control methods on an ankle exoskeleton during human walking," *Proceedings - IEEE*

- International Conference on Robotics and Automation*, vol. 2015-June, no. June, pp. 5584–5589, 2015.
- [45] A. Frisoli, F. Rocchi, S. Marcheschi, A. Dettori, F. Salsedo, and M. Bergamasco, “A new force-feedback arm exoskeleton for haptic interaction in virtual environments,” *Proceedings - 1st Joint Eurohaptics Conference and Symposium on Haptic Interfaces for Virtual Environment and Teleoperator Systems; World Haptics Conference, WHC 2005*, pp. 195–201, 2005.
 - [46] C. Carignan, J. Tang, and S. Roderick, “Development of an exoskeleton haptic interface for virtual task training,” *2009 IEEE/RSJ International Conference on Intelligent Robots and Systems, IROS 2009*, pp. 3697–3702, 2009.
 - [47] G. Aguirre-ollinger, J. E. Colgate, S. Member, M. A. Peshkin, S. Member, A. Goswami, and S. Member, “Inertia Compensation Control of a One-Degree-of- Freedom Exoskeleton for Lower-Limb Assistance : Initial Experiments,” vol. 20, no. 1, pp. 68–77, 2012.
 - [48] C. Silawatchananai and M. Parnichkun, “Haptics control of an arm exoskeleton for virtual reality using pso-based fixed structure h_∞ control,” *International Journal of Advanced Robotic Systems*, vol. 16, no. 3, 2019.
 - [49] A. C. Schouten, E. de Vlugt, J. J. B. van Hilten, and F. C. T. van der Helm, “Design of a torque-controlled manipulator to analyse the admittance of the wrist joint,” *Journal of Neuroscience Methods*, vol. 154, no. 1-2, pp. 134–141, 2006.
 - [50] E. De Vlugt, A. C. Schouten, F. C. Van Der Helm, P. C. Teerhuis, and G. G. Brouwn, “A force-controlled planar haptic device for movement control analysis of the human arm,” *Journal of Neuroscience Methods*, vol. 129, no. 2, pp. 151–168, 2003.
 - [51] M. R. Tucker, J. Olivier, A. Pagel, H. Bleuler, M. Bouri, O. Lambercy, J. R. Del Millán, R. Riener, H. Vallery, and R. Gassert, “Control strategies for active lower extremity prosthetics and orthotics: A review,” *Journal of NeuroEngineering and Rehabilitation*, vol. 12, no. 1, 2015.
 - [52] A. Pennycott, D. Wyss, H. Vallery, V. Klamroth-Marganska, and R. Riener, “Towards more effective robotic gait training for stroke rehabilitation: a review,” *Journal of Neuroengineering and Rehabilitation (JNER)*, vol. 9, p. 65, 2012.
 - [53] C. Everarts, H. Vallery, M. Bolliger, and R. Ronsse, “Adaptive position anticipation in a support robot for overground gait training enhances transparency,” *IEEE International Conference on Rehabilitation Robotics*, 2013.
 - [54] W. Zarrad, P. Poignet, R. Cortesão, and O. Company, “Stability and transparency analysis of a haptic feedback controller for medical applications,” *Proceedings of the IEEE Conference on Decision and Control*, no. 1, pp. 5767–5772, 2007.
 - [55] A. Gupta and M. K. O’Malley, “Disturbance-observer-based force estimation for haptic feedback,” *Journal of Dynamic Systems, Measurement and Control, Transactions of the ASME*, vol. 133, no. 1, pp. 3–7, 2011.
 - [56] T. Nozaki, T. Mizoguchi, and K. Ohnishi, “Decoupling strategy for position and force control based on modal space disturbance observer,” *IEEE Transactions on Industrial Electronics*, vol. 61, no. 2, pp. 1022–1032, 2014.
 - [57] R. Cortesao, J. Park, and O. Khatib, “Real-time adaptive control for haptic telemanipulation with kalman active observers,” *IEEE Transactions on Robotics*, vol. 22, no. 5, pp. 987–999, 2006.

- [58] F. Shah and I. G. Polushin, "Design of telerobotic drilling control system with haptic feedback," *Journal of Control Science and Engineering*, 2013.
- [59] W. H. Zhu and S. E. Salcudean, "Stability guaranteed teleoperation: an adaptive motion/force control approach," *IEEE Transactions on Automatic Control*, vol. 45, no. 11, pp. 1951–1969, 2000.
- [60] R. Baumann and R. Clavel, "Haptic interface for virtual reality based minimally invasive surgery simulation," *Proceedings - IEEE International Conference on Robotics and Automation*, vol. 1, no. May, pp. 381–386, 1998.
- [61] P. Malysz and S. Sirouspour, "Nonlinear and filtered force/position mappings in bilateral teleoperation with application to enhanced stiffness discrimination," *IEEE Transactions on Robotics*, vol. 25, no. 5, pp. 1134–1149, 2009.
- [62] H. K. Khalil. Upper Saddle River, NJ: Prentice-Hall, 2002. [Online]. Available: <https://cds.cern.ch/record/1173048>
- [63] J. Colgate and G. Schenkel, "Passivity of a class of sampled-data systems: application to haptic interfaces," in *Proceedings of 1994 American Control Conference - ACC '94*, vol. 3, 1994, pp. 3236–3240.
- [64] T. Hulin, C. Preusche, and G. Hirzinger, "Stability boundary for haptic rendering: Influence of damping and delay," *IEEE/RSJ International Conference on Intelligent Robots and System*, vol. 1, no. 1, pp. 1570–575, 2006.
- [65] M. Tavakoli, A. Aziminejad, R. V. Patel, and M. Moallem, "High-fidelity bilateral teleoperation systems and the effect of multimodal haptics," *IEEE Transactions on Systems, Man, and Cybernetics, Part B: Cybernetics*, vol. 37, no. 6, pp. 1512–1528, 2007.
- [66] J. J. Gil, E. Sánchez, T. Hulin, C. Preusche, and G. Hirzinger, "Stability boundary for haptic rendering: Influence of damping and delay," in *IEEE International Conference on Robotics and Automation*, vol. 1, no. 1, 2007, pp. 124–129.
- [67] T. Hulin, R. G. Camarero, and A. Albu-Schaffer, "Optimal control for haptic rendering: Fast energy dissipation and minimum overshoot," *IEEE International Conference on Intelligent Robots and Systems*, pp. 4505–4511, 2013.
- [68] T. Hulin, A. Albu-Schäffer, and G. Hirzinger, "Passivity and stability boundaries for haptic systems with time delay," *IEEE Transactions on Control Systems Technology*, vol. 22, no. 4, pp. 1297–1309, 2014.
- [69] T. Hulin, "A Practically Linear Relation Between Time Delay and the Optimal Settling Time of a Haptic Device," *IEEE Robotics and Automation Letters*, vol. 2, no. 3, pp. 1632–1639, 2017.
- [70] R. Muradore and P. Fiorini, "A Review of Bilateral Teleoperation Algorithms," *Acta Polytechnica Hungarica*, vol. 13, no. 1, pp. 191–208, 2016.
- [71] D. Lee, O. Martinez-Palafox, and M. W. Spong, "Bilateral teleoperation of multiple cooperative robots over delayed communication networks: Application," *Proceedings - IEEE International Conference on Robotics and Automation*, vol. 2005, no. April, pp. 366–371, 2005.
- [72] X. Liu, R. Tao, and M. Tavakoli, "Adaptive control of uncertain nonlinear teleoperation systems," *Mechatronics*, vol. 24, no. 1, pp. 66–78, 2014. [Online]. Available: <http://dx.doi.org/10.1016/j.mechatronics.2013.11.010>

-
- [73] A. Mohammadi, M. Tavakoli, and H. J. Marquez, "Disturbance observer-based control of non-linear haptic teleoperation systems," *IET Control Theory and Applications*, vol. 5, no. 18, pp. 2063–2074, 2011.
 - [74] A. Badawy, J. Zuraski, F. Bolourchi, and A. Chandy, "Modeling and Analysis of an Electric Power Steering System," *International Congress and Exposition Detroit, Michigan March 1-4, 1999 400*, vol. 1999, no. 724, 1999.
 - [75] M. Brocker, "New control algorithms for steering feel improvements of an electric powered steering system with belt drive," *Vehicle System Dynamics*, vol. 44, no. 1, pp. 759–769, 2006.
 - [76] T. H. Hu, C. J. Yeh, S. R. Ho, T. H. Hsu, and M. C. Lin, "Design of control logic and compensation strategy for electric power steering systems," *2008 IEEE Vehicle Power and Propulsion Conference, VPPC 2008*, pp. 1–6, 2008.
 - [77] P. Yih and J. C. Gerdes, "Modification of vehicle handling characteristics via steer-by-wire," *IEEE Transactions on Control Systems Technology*, vol. 13, no. 6, pp. 965–976, 2005.
 - [78] D. Lee, K. Yi, S. Chang, B. Lee, and B. Jang, "Robust steering-assist torque control of electric-power-assisted-steering systems for target steering wheel torque tracking," *Mechatronics*, vol. 49, no. December 2017, pp. 157–167, 2018. [Online]. Available: <https://doi.org/10.1016/j.mechatronics.2017.12.007>
 - [79] D. I. Katzourakis, D. A. Abbink, R. Happee, and E. Holweg, "Steering force feedback for humanmachine-interface automotive experiments," in *IEEE Transactions on Instrumentation and Measurement*, vol. 60, no. 1, 2011, pp. 32–43.
 - [80] D. Lee, K. Yi, S. Chang, and B. Lee, "A Novel Electric-Power-Steering (EPS) Control Algorithm Development for the Reference Steering Feel Tracking," *SAE Technical Paper*, 2016.
 - [81] D. Lee, K. S. Kim, and S. Kim, "Controller Design of an Electric Power Steering System," *IEEE Transactions on Control Systems Technology*, vol. 26, no. 2, pp. 748–755, 2018.
 - [82] L. Liu, M. Nagai, and P. Raksincharoensak, "On torque control of handling and steering feel for avoidance maneuver with electric power steering," *IFAC Proceedings Volumes (IFAC-PapersOnline)*, vol. 17, no. 1 PART 1, pp. 12 073–12 078, 2008.
 - [83] M. Von Groll, S. Mueller, T. Meister, and R. Tracht, "Disturbance compensation with a torque controllable steering system," *Vehicle System Dynamics*, vol. 44, no. 4, pp. 327–338, 2006.
 - [84] C. Dannöhl, S. Müller, and H. Ulbrich, " H_∞ -control of a rack-assisted electric power steering system," *Vehicle System Dynamics*, vol. 50, no. 4, pp. 527–544, 2012.
 - [85] C. Chitu, J. Lackner, M. Horn, P. S. Pullagura, H. Waser, and M. Kohlböck, "Controller design for an electric power steering system based on LQR techniques," *COMPEL: The International Journal for Computation and Mathematics in Electrical and Electronic Engineering*, vol. 32, no. 3, pp. 763–775, 2013. [Online]. Available: <http://www.emeraldinsight.com/10.1108/03321641311305737>
 - [86] J. Ekmark and J. Pohl, "Control strategy for computer-controlled steering," *European Patent Specification: EP1431160B1*, pp. 1–20, 2006.

- [87] H. Hsu and M. Harrer, “The New Steering System in the 911 Porsche Carrera – Optimized Design of a Steering System for Sportcars,” *21st Aachen Colloquium Automobile and Engine Technology*, 2012.
- [88] A. Marouf, C. Sentouh, M. Djemai, and P. Pudlo, “Control of an Electric Power Assisted Steering system using reference model,” *Proceedings of the IEEE Conference on Decision and Control*, pp. 6684–6690, 2011.
- [89] A. Marouf, M. Djemai, C. Sentouh, and P. Pudlo, “A new control strategy of an electric-power-assisted steering system,” *IEEE Transactions on Vehicular Technology*, vol. 61, no. 8, pp. 3574–3589, 2012.
- [90] T. Yang, “A new control framework of electric power steering system based on admittance control,” *IEEE Transactions on Control Systems Technology*, vol. 23, no. 2, pp. 762–769, 2015.
- [91] S. Amberkar, F. Bolourchi, J. Demerly, and S. Millsap, “A control system methodology for steer by wire systems,” *SAE Technical Paper*, no. 1–8, 2004. [Online]. Available: <https://doi.org/10.4271/2004-01-1106>
- [92] A. Baviskar, J. R. Wagner, D. M. Dawson, D. Braganza, and P. Setlur, “An adjustable steer-by-wire haptic-interface tracking controller for ground vehicles,” *IEEE Transactions on Vehicular Technology*, vol. 58, no. 2, pp. 546–554, 2009.
- [93] R. Hayama, S. Kawahara, and S. Nakano, “Resistance torque control for steer-by-wire system to improve human – machine interface,” *Vehicle System Dynamics*, vol. 48, no. 9, pp. 1065–1075, 2010.
- [94] A. Balachandran and J. C. Gerdes, “Designing steering feel for steer-by-wire vehicles using objective measures,” *IEEE/ASME Transactions on Mechatronics*, vol. 20, no. 1, pp. 373–383, 2015.
- [95] S. Fankem and S. Müller, “A new model to compute the desired steering torque for steer-by-wire vehicles and driving simulators,” in *Vehicle System Dynamics*, vol. 52, no. 1, 2014.
- [96] T. Koch, “Bewertung des lenkgefühls in einem sportfahrzeug mit steer-by-wire lenksystem,” *18. Aachener Kolloquium Fahrzeug- und Motorentechnik*, pp. 493–507, 2009.
- [97] D. Gualino and I.-J. Adounkpe, “Force-feedback system design for the steer-by-wire: Optimisation and performance evaluation,” *2006 IEEE Intelligent Transportation Systems Conference*, pp. 181–187, 2006.
- [98] N. Bajcinca, R. Cortesao, M. Hauschild, J. Bals, and G. Hirzinger, “Haptic control for steer-by-wire systems,” *Proceedings IEEE/RSJ International Conference on Intelligent Robots and Systems*, vol. 2, pp. 2004–2009, 2003.
- [99] D. Gualino and I. J. Adounké, “Robust 2-DOF H_∞ controller for a force feedback system,” *Proceedings of the IEEE International Conference on Control Applications*, vol. 1, no. October, pp. 1253–1259, 2007.
- [100] D. Katzourakis, “Driver Steering Support Interfaces Near the Vehicle’s Handling Limits,” Ph.D. dissertation, Delft University of Technology, 2012. [Online]. Available: <http://resolver.tudelft.nl/uuid:87f43ef4-c94a-43f1-8c24-d487b387ebbb>
- [101] J.-I. Svensson, J. Pohl, S. Ragnhult, and J. Hultén, “A method and a system for assisting a driver of a vehicle during operation,” *European Patent Specification: EP2857286B1*, pp. 1–18, 2017.

-
- [102] H. Zheng, J. Hu, and Y. Liu, "A bilateral control scheme for vehicle steer-by-wire system with road feel and steering controller design," *Transactions of the Institute of Measurement and Control*, vol. 41, no. 3, pp. 593–604, 2019.
- [103] T. van der Sande, P. Zegelaar, I. Besselink, and H. Nijmeijer, "A robust control analysis for a steer-by-wire vehicle with uncertainty on the tyre forces," *Vehicle System Dynamics*, vol. 54, no. 9, pp. 1247–1268, 2016. [Online]. Available: <http://dx.doi.org/10.1080/00423114.2016.1197407>
- [104] T. Van Der Sande, P. Zegelaar, I. Besselink, and H. Nijmeijer, "Upperbounds on the closed loop sensitivity for the control of a steer-by-wire vehicle," *Proceedings of the 13th International Symposium on Advanced Vehicle Control (AVEC)*, no. 1, pp. 405–410, 2016.
- [105] Z. Sun, J. Zheng, Z. Man, and H. Wang, "Robust Control of a Vehicle Steer-by-Wire System Using Adaptive Sliding Mode," *IEEE Transactions on Industrial Electronics*, vol. 63, no. 4, pp. 2251–2262, 2016.
- [106] H. Wang, Z. Man, W. Shen, Z. Cao, J. Zheng, J. Jin, and D. M. Tuan, "Robust control for steer-by-wire systems with partially known dynamics," *IEEE Transactions on Industrial Informatics*, vol. 10, no. 4, pp. 2003–2015, 2014.
- [107] M. Mulder and D. A. Abbink, "The effect of haptic guidance on curve negotiation behavior of young, experienced drivers," *Proceedings of the IEEE International Conference on Systems, Man and Cybernetics*, pp. 804–809, 2008.
- [108] M. Rothhämel, J. Ijkema, and L. Drugge, "Influencing driver chosen cornering speed by means of modified steering feel," *Vehicle System Dynamics*, vol. 52, no. 4, pp. 522–538, 2014. [Online]. Available: <https://doi.org/10.1080/00423114.2013.841964>
- [109] P. M. Van Leeuwen, S. De Groot, R. Happee, and J. C. De Winter, "Differences between racing and non-racing drivers: A simulator study using eye-tracking," *PLoS ONE*, vol. 12, no. 11, pp. 1–19, 2017. [Online]. Available: <http://dx.doi.org/10.1371/journal.pone.0186871>
- [110] N. Kim and D. J. Cole, "A model of driver steering control incorporating the driver's sensing of steering torque," *Vehicle System Dynamics*, vol. 49, no. 10, pp. 1575–1596, 2011.
- [111] J. Timings and D. Cole, "Robust lap-time simulation," *Proceedings of the Institution of Mechanical Engineers, Part D: Journal of Automobile Engineering*, vol. 228, no. 10, pp. 1200–1216, 2014. [Online]. Available: <https://doi.org/10.1177/0954407013516102>
- [112] D. J. Cole, "Influence of Steering Torque Feedback and Neuromuscular Dynamics on Driver and Vehicle Response To Lateral Force Disturbance," *22nd IAVSD Symposium on the Dynamics of Vehicles on Roads and Tracks*, pp. 1–6, 2011.
- [113] A. J. Pick and D. J. Cole, "A Mathematical Model of Driver Steering Control Including Neuromuscular Dynamics," *Journal of Dynamic Systems, Measurement, and Control*, vol. 130, no. 3, p. 031004, 2008.
- [114] D. J. Cole, "A path-following driver-vehicle model with neuromuscular dynamics, including measured and simulated responses to a step in steering angle overlay," *Vehicle System Dynamics*, vol. 50, no. 4, pp. 573–596, 2012.
- [115] A. J. Tremlett and D. J. Limebeer, "Optimal tyre usage for a Formula One car," *Vehicle System Dynamics*, vol. 54, no. 10, pp. 1448–1473, 2016. [Online]. Available: <https://doi.org/10.1080/00423114.2016.1213861>

- [116] W. J. West and D. J. Limebeer, "Optimal tyre management for a high-performance race car," *Vehicle System Dynamics*, vol. 0, no. 0, pp. 1–19, 2020. [Online]. Available: <https://doi.org/10.1080/00423114.2020.1802047>
- [117] L. J. Mardh and M. Haglund, "Apparatus and method for situation dependent wheel angle control (HAD or ADAS)," pp. 1–19, 2018.
- [118] J.-Y. Hsu, C.-J. Yeh, T.-H. Hu, T.-H. Hsu, and F.-H. Sun, "Development of active steering angle control based on electric power steering systems," *2011 IEEE Vehicle Power and Propulsion Conference*, pp. 1–6, 2011. [Online]. Available: <http://ieeexplore.ieee.org/lpdocs/epic03/wrapper.htm?arnumber=6042999>
- [119] D. A. Abbink, M. Mulder, and E. R. Boer, "Haptic shared control: Smoothly shifting control authority?" *Cognition, Technology and Work*, vol. 14, no. 1, pp. 19–28, 2012.
- [120] D. I. Katzourakis, E. Velenis, E. Holweg, and R. Happee, "Haptic steering support for driving near the vehicle's handling limits: Test-track case," *IEEE Transactions on Intelligent Transportation Systems*, vol. 15, no. 4, pp. 1781–1789, 2014.
- [121] N. R. Kapania and J. C. Gerdes, "Learning at the Racetrack: Data-Driven Methods to Improve Racing Performance over Multiple Laps," *IEEE Transactions on Vehicular Technology*, vol. 69, no. 8, pp. 8232–8242, 2020.
- [122] K. Kritayakirana and J. C. Gerdes, "Autonomous vehicle control at the limits of handling," *International Journal of Vehicle Autonomous Systems*, vol. 10, no. 4, pp. 271–296, 2012.
- [123] J. K. Subosits and J. C. Gerdes, "A synthetic input approach to slip angle based steering control for autonomous vehicles," *Proceedings of the American Control Conference*, pp. 2297–2302, 2017.
- [124] T. Goel, J. Y. Goh, and J. C. Gerdes, "Opening New Dimensions: Vehicle Motion Planning and Control using Brakes while Drifting," *IEEE Intelligent Vehicles Symposium, Proceedings*, no. Iv, pp. 560–565, 2020.
- [125] J. Y. Goh and J. C. Gerdes, "Simultaneous stabilization and tracking of basic automobile drifting trajectories," *IEEE Intelligent Vehicles Symposium, Proceedings*, vol. 2016-Augus, no. Iv, pp. 597–602, 2016.
- [126] N. R. Kapania and J. C. Gerdes, "Path tracking of highly dynamic autonomous vehicle trajectories via iterative learning control," *Proceedings of the American Control Conference*, pp. 2753–2758, 2015.
- [127] S. M. Erlien, J. Funke, and J. C. Gerdes, "Incorporating non-linear tire dynamics into a convex approach to shared steering control," pp. 3468–3473, 2014. [Online]. Available: <http://ieeexplore.ieee.org/document/6859116/>
- [128] A. Balachandran, M. Brown, S. M. Erlien, and J. C. Gerdes, "Predictive haptic feedback for obstacle avoidance based on model predictive control," *IEEE Transactions on Automation Science and Engineering*, vol. 13, no. 1, pp. 26–31, 2016.
- [129] M. Mulder, D. A. Abbink, and E. R. Boer, "Sharing control with haptics: Seamless driver support from manual to automatic control," *Human Factors*, vol. 54, no. 5, pp. 786–798, 2012.
- [130] L. Saleh, P. Chevrel, F. Claveau, J. F. Lafay, and F. Mars, "Shared steering control between a driver and an automation: Stability in the presence of driver behavior uncertainty," *IEEE Transactions on Intelligent Transportation Systems*, vol. 14, no. 2, pp. 974–983, 2013.

- [131] International Organization for Standardization, “ISO 26262-9:2018 Road vehicles — Functional safety — Part 9: Automotive safety integrity level (ASIL)-oriented and safety-oriented analyses,” 2018.
- [132] K. J. Åström and R. M. Murray, *Feedback Systems : An Introduction for Scientists and Engineers*. Princeton University Press, 2008.
- [133] T. Piatkowski, “Dahl and LuGre dynamic friction models - The analysis of selected properties,” *Mechanism and Machine Theory*, vol. 73, pp. 91–100, 2014. [Online]. Available: <http://dx.doi.org/10.1016/j.mechmachtheory.2013.10.009>
- [134] S. Skogestad and I. Postlethwaite, *Multivariable Feedback Control: Analysis and Design*. Wiley, England, 2005.
- [135] R. Rajamani, *Vehicle Dynamics and Control*. Springer, Boston, MA, 2012.
- [136] A. Albinsson, “Online and Offline Identification of Tyre Model Parameters,” Ph.D. dissertation, Chalmers University of Technology, 2018. [Online]. Available: https://research.chalmers.se/publication/501552/file/501552_Fulltext.pdf
- [137] H. B. Pacejka, “Chapter 4 - Semi-Empirical Tire Models,” in *Tire and Vehicle Dynamics (Third Edition)*, 3rd ed. Oxford: Butterworth-Heinemann, 2012, pp. 149–209. [Online]. Available: <https://www.sciencedirect.com/science/article/pii/B9780080970165000048>
- [138] IPG Automotive, “Carmaker simulation software,” <https://ipg-automotive.com/areas-of-application/vehicle-dynamics/>, accessed: 2021-08-03.
- [139] D. I. Katzourakis, D. A. Abbink, E. Velenis, E. Holweg, and R. Happee, “Driver’s arms’ time-variant neuromuscular admittance during real car test-track driving,” *IEEE Transactions on Instrumentation and Measurement*, vol. 63, no. 1, pp. 221–230, 2014.
- [140] C. R. Carignan and K. R. Cleary, “Closed-loop force control for haptic simulation of virtual environments,” *Haptics-e*, vol. 1, no. 2, pp. 1–14, 2000.
- [141] S. Sirouspour and P. Setoodeh, “Adaptive nonlinear teleoperation control in multi-master/multi-slave environments,” in *Proceedings of 2005 IEEE Conference on Control Applications, 2005. CCA 2005.*, 2005, pp. 1263–1268.
- [142] P. E. Pfeffer and M. Harrer, “On-Centre Steering Wheel Torque Characteristics during Steady State Cornering,” *SAE International*, vol. 2008, no. 724, 2008.
- [143] L. Schenk, T. Chugh, and F. Bruzelius, “Musculoskeletal Driver Model for the Steering Feedback Controller,” *Dynamics and Control of Automated Vehicles, MDPI*, vol. 3, no. 1, pp. 111–126, 2021.
- [144] F. Wilhelm, T. Tamura, R. Fuchs, and P. Mullhaupt, “Friction Compensation Control for Power Steering,” *IEEE Transactions on Control Systems Technology*, vol. 24, no. 4, pp. 1354–1367, 2016.
- [145] P. Dahl, “A solid friction model,” *Aerospace Corporation El Segundo, CA*, vol. 158, pp. Tech. Rep. TOR-01 58(3 107-1 8)- 1, 1968. [Online]. Available: <http://oai.dtic.mil/oai/oai?verb=getRecord&metadataPrefix=html&identifier=ADA041920>
- [146] R. Hensen and M. van de Molengraft, “Friction induced hunting limit cycles: an event mapping approach,” *Proceedings of the 2002 American Control Conference*, pp. 2267–2272 vol.3, 2002. [Online]. Available: <http://ieeexplore.ieee.org/document/1023978/>
- [147] C. Canudas de Witt, H. Olsson, S. Member, P. Lischinsky, C. Canudas De Wit, and K. J. Åström, “A new model for control of systems with friction,” *IEEE transactions on automatic control*, vol. 40, no. 3, pp. 419–425, 1995.

- [148] P. E. Pfeffer, M. Harrer, and D. N. Johnston, "Interaction of vehicle and steering system regarding on-centre handling," *Vehicle System Dynamics*, vol. 46, no. 5, pp. 413–428, 2008. [Online]. Available: <https://doi.org/10.1080/00423110701416519>
- [149] S. Fankem, T. Weiskircher, and S. Müller, "Model-based rack force estimation for electric power steering," in *IFAC Proceedings Volumes (IFAC-PapersOnline)*, vol. 19, 2014, pp. 8469–8474.
- [150] P. Brunn and M. Harrer, "Objektivierung der lenkungsrückmeldung," *VDI Fortschritt-Berichte*, pp. 67–79, 2004.
- [151] E. De Vlugt, A. C. Schouten, F. C. Van Der Helm, P. C. Teerhuis, and G. G. Brouwn, "A force-controlled planar haptic device for movement control analysis of the human arm," *Journal of Neuroscience Methods*, vol. 129, no. 2, pp. 151–168, 2003.
- [152] H. Vallery, "Stable and User-Controlled Assistance of Human Motor Function," Ph.D. dissertation, Technischen Universität München, 2009.
- [153] J. Edward Colgate, "Strictly positive real admittances for coupled stability," *Journal of the Franklin Institute*, vol. 329, no. 3, pp. 429–444, 1992.
- [154] L. Ni, A. Gupta, P. Falcone, and L. J. Mardh, "Vehicle Lateral Motion Control with Performance and Safety Guarantees," *IFAC-PapersOnLine*, vol. 49, no. 11, pp. 285–290, 2016.
- [155] N. R. Kapania and J. C. Gerdes, "Design of a feedback-feedforward steering controller for accurate path tracking and stability at the limits of handling," *Vehicle System Dynamics*, vol. 53, no. 12, pp. 1687–1704, 2015. [Online]. Available: <http://dx.doi.org/10.1080/00423114.2015.1055279>
- [156] S. D. Cairano, H. E. Tseng, D. Bernardini, and A. Bemporad, "Steering Vehicle Control by Switched Model Predictive Control," in *6th IFAC Symposium Advances in Automotive Control*. Munich, Germany: IFAC, 2010, pp. 1–6.
- [157] P. Falcone, F. Borrelli, J. Asgari, H. E. Tseng, and D. Hrovat, "Predictive Active Steering Control for Autonomous Vehicle Systems," *IEEE Transactions on Control Systems Technology*, vol. 15, no. 3, pp. 566–580, 2007.
- [158] F. Borrelli, P. Falcone, and T. Keviczky, "MPC-Based Approach to Active Steering for Autonomous Vehicle Systems," *International Journal of Vehicle Autonomous Systems*, vol. 3, no. 2/3/4, pp. 265 – 291, 2005.
- [159] Y. Gao, "Model predictive control for autonomous and semi-autonomous vehicles," Ph.D. dissertation, University of California, Berkeley, 2014.
- [160] P. Gahinet and P. Apkarian, "A linear matrix inequality approach to H_∞ control," *International Journal of Robust and Nonlinear Control*, vol. 4, no. 4, pp. 421–448, 1994.
- [161] H. B. Pacejka, "Chapter 7 - Single-Contact-Point Transient Tire Models," in *Tire and Vehicle Dynamics (Third Edition)*, 3rd ed. Oxford: Butterworth-Heinemann, 2012, pp. 329–354. [Online]. Available: <https://www.sciencedirect.com/science/article/pii/B9780080970165000073>
- [162] E. Wan and R. Van Der Merwe, "The unscented kalman filter for nonlinear estimation," *Proceedings of the IEEE Adaptive Systems for Signal Processing, Communications, and Control Symposium*, pp. 153–158, 2000.

- [163] A. Bemporad and M. Morari, “Control of systems integrating logic, dynamics, and constraints,” *Automatica*, vol. 35, no. 3, pp. 407–427, 1999.
- [164] J. Rawlings, D. Mayne, and M. Diehl, *Model Predictive Control: Theory, Computation, and Design*. Nob Hill Publishing, 2017.
- [165] F. Borrelli, A. Bemporad, and M. Morari, *Predictive Control for Linear and Hybrid Systems*. Cambridge University Press, 2017.

Appended Papers